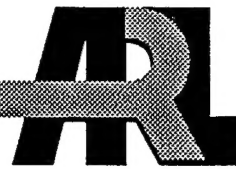


ARMY RESEARCH LABORATORY



**A Process Model and Complementary Experiments for the  
Electron Cyclotron Resonance (ECR) Technology:  
Application to Deposition and Etching**

**M. Meyyappan, T.R. Govindan, F. de Jong and R.C. Buggeln**

ARL-CR-317

December 1996

prepared by  
Scientific Research Associates, Inc.  
P.O. Box 1058  
Glastonbury, CT 06033

under contract  
DAAL01-93-C-3331

19970408 040

DTIG QUALITY INSPECTED 3

APPROVED FOR PUBLIC RELEASE; DISTRIBUTION IS UNLIMITED.

## **NOTICES**

### **Disclaimers**

The findings in this report are not to be construed as an official Department of the Army position, unless so designated by other authorized documents.

The citation of trade names and names of manufacturers in this report is not to be construed as official Government endorsement or approval of commercial products or services referenced herein.

REPORT DOCUMENTATION PAGE			Form Approved OMB NO. 0704-0188
<p>Public reporting burden for this collection of information is estimated to average 1 hour per response, including the time for reviewing instructions, searching existing data sources, gathering and maintaining the data needed, and completing and reviewing the collection of information. Send comment regarding this burden estimates or any other aspect of this collection of information, including suggestions for reducing this burden, to Washington Headquarters Services, Directorate for Information Operations and Reports, 1215 Jefferson Davis Highway, Suite 1204, Arlington, VA 22202-4302, and to the Office of Management and Budget, Paperwork Reduction Project (0704-0188), Washington, DC 20503.</p>			
1. AGENCY USE ONLY (Leave blank)	2. REPORT DATE December 1996	3. REPORT TYPE AND DATES COVERED SBIR Phase II Final Report	
4. TITLE AND SUBTITLE A PROCESS MODEL AND COMPLEMENTARY EXPERIMENTS FOR THE ELECTRON CYCLOTRON RESONANCE (ECR) TECHNOLOGY: APPLICATION TO DEPOSITION AND ETCHING		5. FUNDING NUMBERS C: DAAL01-93-C-3331	
6. AUTHOR(S) M. Meyyappan, T.R. Govindan, F. de Jong and R.C. Buggeln			
7. PERFORMING ORGANIZATION NAMES(S) AND ADDRESS(ES) Scientific Research Associates, Inc. P.O. Box 1058 Glastonbury, CT 06033		8. PERFORMING ORGANIZATION REPORT NUMBER	
9. SPONSORING / MONITORING AGENCY NAME(S) AND ADDRESS(ES) US Army Research Laboratory (ARL) Sensors & Electron Devices Directorate ATTN: AMSRL-SE-RL (G. McLane) Fort Monmouth, NJ 07703-5601		10. SPONSORING / MONITORING AGENCY REPORT NUMBER ARL-CR-317	
11. SUPPLEMENTARY NOTES			
12a. DISTRIBUTION / AVAILABILITY STATEMENT Approved for public release; distribution is unlimited.		12 b. DISTRIBUTION CODE	
13. ABSTRACT (Maximum 200 words)  This Phase II SBIR project was undertaken to model the Electron Cyclotron Resonance (ECR) based plasma processing with a view to understanding plasma mechanisms and aiding in process and equipment design. Models of various complexity levels were successfully developed and applied to ECR discharges. The computer codes were used to study the effects of flow rates, pressure, microwave power and reactor geometry parameters on the process figures-of-merit. This allows understanding of the ECR mechanisms in various electropositive and reactive discharges. The model and code are useful in design of new generation plasma equipment and also in process design and optimization. A graphical user interface was also developed for the easy use of one of the codes.			
14. SUBJECT TERMS Electron Cyclotron Resonance; Plasma Processing; Computer Code		15. NUMBER OF PAGES 99	16. PRICE CODE
17. SECURITY CLASSIFICATION OF REPORT Unclassified	18. SECURITY CLASSIFICATION OF THIS PAGE Unclassified	19. SECURITY CLASSIFICATION OF ABSTRACT Unclassified	20. LIMITATION OF ABSTRACT UL

## Table of Contents

<b>1. Introduction .....</b>	<b>1</b>
<b>2. Background .....</b>	<b>5</b>
<b>3. Model Development .....</b>	<b>7</b>
<b>A. Governing Equations.....</b>	<b>7</b>
<b>B. One-dimensional Model.....</b>	<b>14</b>
<b>C. Zero-dimensional Model.....</b>	<b>18</b>
<b>D. Two-dimensional Fluid Flow Analysis.....</b>	<b>24</b>
<b>4. Experimental Data .....</b>	<b>25</b>
<b>5. ECR Argon Discharge Physics: 0-d Results.....</b>	<b>33</b>
<b>6. ECR Chlorine Discharge Physics: 0-d Results.....</b>	<b>41</b>
<b>7. ECR Argon Discharge Physics: 1-d Results .....</b>	<b>52</b>
<b>8. Pulsed ECR Discharges.....</b>	<b>61</b>
<b>9. 2-d Gas Flow Modeling.....</b>	<b>71</b>
<b>10. Etching Studies.....</b>	<b>77</b>
<b>A. CF<sub>4</sub> etching of silicon and SiO<sub>2</sub> .....</b>	<b>77</b>
<b>11. User-Friendly Code .....</b>	<b>92</b>
<b>12. Summary and Conclusions .....</b>	<b>93</b>
<b>References.....</b>	<b>95</b>

## List of Figures

<b>4.1 Radial profiles of electron density in an 8" PlasmaTherm ECR reactor.</b> .....	27
<b>4.2 F and CF<sub>2</sub> densities in an ECR CF<sub>4</sub> discharge measured by K. Ashtiani.</b> .....	29
<b>4.3 Axial profiles of electron density, electron temperature, and plasma potential measured by K. Ono in an ECR chlorine discharge at 0.8 mTorr.</b> .....	30
<b>4.4 Axial profiles of electron density, electron temperature, and plasma potential measured by K. Ono in an ECR chlorine discharge at 0.24 mTorr.</b> .....	31
<b>4.5 Radial profiles of electron density and temperature in chlorine provided by Ono.</b> .....	32
<b>5.1 Gas temperature in the ECR source chamber as a function of pressure and absorbed microwave power.</b> .....	34
<b>5.2 Pressure dependence of spatially-averaged electron temperature and density.</b> .....	36
<b>5.3 Variation of spatially-averaged electron density and temperature with absorbed microwave power.</b> .....	37
<b>5.4 Effect of source geometry on plasma characteristics.</b> .....	40
<b>6.1 Spatially-averaged electron temperature in an ECR source chamber (radius = 0.1 m, length = 0.5 m) at a Cl<sub>2</sub> for rate of 10 sccm.</b> .....	44
<b>6.2 Effect of pressure on ECR chlorine discharge characteristics: Cl<sub>2</sub> flow rate = 10 sccm; absorbed microwave power = 800 W.</b> .....	45
<b>6.3 Effect of absorbed microwave power on ECR chlorine discharge characteristics: Cl<sub>2</sub> flow rate = 10 sccm; pressure = 0.267 Pa.</b> .....	48
<b>6.4 Effect of Cl<sub>2</sub> flow rate: Pressure = 0.267 Pa, absorbed power = 800 W, radius = 0.1 m and length = 0.5 m.</b> .....	49
<b>6.5 Effect of source chamber radius on electron density n<sub>e</sub>, electron temperature T<sub>e</sub>, and electron density per power density</b> .....	51
<b>7.1 Comparison of predicted and measured pressures in the source chamber (upstream) with no microwave power and in the absence of plasma.</b> .....	53
<b>7.2 Axial profiles of various parameters at 500 W and 20 sccm argon flow</b> .....	55
<b>7.3 The effect of argon flow rate on the axial profiles of various parameters</b> .....	57
<b>7.4 Electron temperature and electron density as a function of pressure</b> .....	59

<b>8.1 Density of various species and reaction rates in a pulsed chlorine discharge. ....</b>	63
<b>8.2 Effect of duty ratio on electron density and temperature in a pulsed chlorine discharge. ....</b>	66
<b>8.3 Effect of pulse period on electron density and temperature in a pulsed chlorine discharge. ....</b>	67
<b>8.4 Densities of radicals and ions in a pulse-modulated <math>\text{CF}_4</math> discharge. ....</b>	69
<b>9.1 Two-dimensional gas flow simulation of an ECR reactor from ref. [40]. ....</b>	72
<b>9.2 Flow streamlines in an ECR chlorine plasma. ....</b>	74
<b>9.3 Nitrogen in an ECR reactor. ....</b>	75
<b>9.4 Same as in Fig. 9.3 with temperature jump condition, Eq. (49). ....</b>	76
<b>10.1 Rate constants vs mean energy for reactions in Tabel 10.1. ....</b>	79
<b>10.2 Variation of pressure with normalized distance (z/L) in an ECR reactor at <math>\text{CF}_4</math> flow rates of 30 sccm and 80 sccm. ....</b>	81
<b>10.3 Two-dimensional results of gas flow without the plasma at 2 mTorr. ....</b>	83
<b>10.4 Profiles of electron density (<math>n_e</math>) and temperature (<math>T_e</math>) in an ECR reactor at 500 W of absorbed microwave power, 2 mTorr exit pressure, and 30 sccm <math>\text{CF}_4</math> flow rate. ....</b>	85
<b>10.5 Electron density (<math>n_e</math>) and temperature (<math>T_e</math>) as a function of pressure at 500 W power. ....</b>	87
<b>10.6 Profiles of neutral temperature and mass-averaged mixture velocity in an ECR <math>\text{CF}_4</math> discharge. ....</b>	88
<b>10.7 Density profiles at 2 mTorr and 30 sccm <math>\text{CF}_4</math>. ....</b>	90
<b>10.8 Effect of pressure on radical concentrations. ....</b>	91

## List of Tables

<b>Table 4.1</b> .....	25
<b>Table 4.2</b> .....	25
<b>Table 4.3</b> .....	26
<b>Table 6.1</b> .....	42
<b>Table 6.2</b> .....	46
<b>Table 6.3</b> .....	47
<b>Table 10.1</b> .....	78
<b>Table 10.2</b> .....	82

## 1. Introduction

Plasma processing is a key technology in integrated circuit manufacturing. Plasma-based etching and deposition are two critical steps in device processing in the fabrication of microelectronics and optoelectronics devices. Plasma etching is widely used to faithfully replicate patterns and to create via holes with desirable anisotropy. Some of the expectations from a good etch process include high etch rates, etch uniformity over large areas, good selectivity between the semiconductor and the mask material, ability to produce etch profiles with minimal undercutting (i.e., desirable anisotropic features), and minimal damage to the underlying layers. While these are the very reasons the industry moved away from wet etching, the objectives are achieved to different degrees with various plasma etch technologies, such as reactive ion etching (RIE), reactive ion beam etching (RIBE), electron cyclotron resonance (ECR) etching, etc. It is important to point out that not all of the above expectations are achieved simultaneously, though that is the coveted goal. In plasma-based deposition, the technology is mainly useful to deposit masking layers at low temperatures in order to avoid heat induced damage to the underlying layers. Again here, the expectations of a good process are high deposition rate, ability to obtain desirable film composition, conformity to the patterns (i.e., good step coverage of the features over which deposition is performed), and uniformity over large areas. With the increasing role played by plasma etching and deposition, plasma processing has a conceivable impact of billions of dollars for the semiconductor and integrated circuit market.

Until the late 1980's, virtually all manufacturing in plasma processing used radiofrequency (rf) capacitive coupled plasma (CCP)- based systems: reactive ion etching (RIE) and rf plasma-enhanced chemical vapor deposition (rf PECVD). As device size continued to shrink and wafer size continued to increase, the rf CCP-based processing has begun to lose its edge. Critical failures of the technique at this stage were (i) etch-induced damage due to large negative dc bias and ensuing ion bombardment, (ii) inability to scale down to submicron feature sizes, and (iii) inability to provide uniformity over, say, 6" wafers. It was found necessary to operate under pressures well below 100 mTorr to obtain anisotropy. However, it is hard to get a high plasma density at these pressures, which is essential to maintain acceptable processing rates. To do so, if one were to increase the applied power at low pressures, then the negative dc bias and ion bombardment on the

substrate increase rapidly. This led to excessive wafer damage. For a while, magnetron-based technologies emerged wherein a magnetic field (either using permanent or electro magnets) was employed to overcome some of the drawbacks mentioned above. The E X B field near the substrate prevented the electrons from being lost quickly by wall recombination and thus increased the ionization efficiency. High plasma density ( $\sim 10^{11} \text{ cm}^{-3}$ ) at low pressures was certainly possible. The high density also allowed lower dc biases on the substrate and hence lower damage. In a previous SBIR project with the Army Research Laboratory, this technology was demonstrated successfully for etching GaAs [1]. Since then, magnetron-based etching has been an integral part of device processing at the ARL, Fort Monmouth, NJ [2]. Though magnetron-based technology had considerable promise, it never caught on with the industry and appears to be rarely used in manufacturing.

Right around 1990, electron cyclotron resonance (ECR) technology started receiving much attention in the U.S. It was previously more popular in Japan. Indeed, when we started this project in 1991, all large scale ECR machines for IC fabrication were from Japanese manufacturers. PlasmaTherm, in Florida, has been selling small ECR units for R&D (U.S. ARL at Fort Monmouth uses one of these units for ECR deposition). ASTEX, in Massachusetts, has been building ECR units for diamond deposition. ECR certainly offers potential to meet the expectations outlined in the opening paragraph. Preliminary research coming out of Japan and the U.S. indicated true promise for the ECR technology. There were several issues unresolved at the time this project was initiated, as discussed in the next paragraph. Resolving these issues required understanding of process mechanisms, which led to the initiation of this study. It is important to emphasize here that, during the tenure of this study, the U.S. industry was also looking at other technologies to counteract Japanese monopoly of ECR technology. To a great extent (at least in etching), success has been reached with inductively coupled plasma (ICP) processing. Today, Applied Materials and Lam Research, among other U.S. companies, sell ICP-based units. ICP technology has several issues common with ECR which require an understanding of mechanisms. No attempt was made here to study ICP in detail, which would have meant deviation from the work statement. However, many of the model developments apply well to ICP and address similar concerns.

There are several important issues in high density plasma processing. ECR processing is extremely complex; perhaps, more than any other competing technique. There is a strong

interaction among the following aspects: microwave propagation, magnetic field, plasma generation in the resonance region, plasma transport, radical and ion generation and their uniformity, feed gas injection and fluid flow, neutral heating, wall and surface processes, wafer location with respect to the location of plasma generation, just to name a few. Also, the well-known chemistries with RIE and PECVD and the corresponding process recipes cannot be simply reapplied with ECR. The high plasma density and high flux of low energy ions meant reinventing new recipes using the old chemistries. The issues in etching are as follows. The general objectives are the same as listed in the opening paragraph. But in practice, and in process and reactor development, it is important to understand plasma generation and transport mechanisms.

- What are the effects of the magnetic coil and hence, ECR location?
- the effect of substrate location with respect to the ECR zone
- effects of pressure, power, and feed gas rates on plasma and etch characteristics
- magnitude and uniformity of ion flux and ion energy over the wafer
- etch mechanisms

The ECR deposition shares many of the same questions. In addition, it is important to determine the parameters which ensure good film quality and adherence of the (mask) films or layers to the underlying layer. Here again, the magnitude and uniformity of ion flux and energy over the wafer are critical parameters. Unlike in etching, the deposition technology may involve introduction of additional feed streams directly in the process chamber. It is thought that such downstream introduction of a gas stream may prevent electron impact dissociation of that particular stream. But in practice, back diffusion of that stream into the upper chamber can result in plasma dissociation of that second mixture or in many cases, the electron density and energy in the downstream chamber itself are too high to promote many electron impact reactions.

When the technology is in the early evolving stages, all issues listed above can be addressed using a combination of plasma and surface characterization experimental work and modeling. This is the underlying premise for the current project. Though this project at SRA did not directly involve any experimental work in-house and complementary characterization works are needed for the purpose of model input generation, knowledge of chemistry, and finally, for model validation, such information was gathered from several sources. ARL's work in this field was primarily on ECR nitride deposition with related diagnostics and was available through publications from ARL. More basic diagnostics involving electron density, electron temperature, and species concentration measurements for gas streams with known reaction kinetic data were provided to this project from collaborators. With these resources, the focus was on model development for ECR processing.

Complementary modeling and diagnostics has several benefits. First, at the stage when equipment is developed, a large degree of trial and error-based design is common now. Availability of reliable models reduces the expense of trial and error and provides a tool to the equipment design team which can be used to generate answers to many "so what happens if I change this" type of questions. Second, in the production line, there is a need to come up with optimum settings for various input parameters to meet specific process targets. A model can identify the effect of varying each parameter separately or in groups and ultimately in optimization. Third, in principle, process control can be model-based. All these three scenarios are important to the semiconductor industry and the equipment industry. Hence, the commercial impact is large. The processes commonly include Si etching, oxide etching, mask layer deposition, to name a few. The same scenarios and processes are critical to DoD too, since DoD is a large consumer of many of these commercial products, in addition to very specialized circuits and components. In both cases, a supply of high quality products at low cost has become critical to DoD now, due to severe budgetary cuts. Finally, there is the application of ECR technology in III-V compound processing with unique needs in DoD and a small commercial market.

This report is organized as follows. A technical background is provided in Chapter 2. Model development is discussed in detail in Chapter 3. A compilation of experimental data is provided in Chapter 4. Following this, the results of this work are organized in several successive chapters. Finally, a summary is presented in Chapter 11.

## 2. Background

In this section we provide a brief background on ECR technique, equipment, processing and diagnostics results, and a survey of models in the literature.

The ECR technology uses a 2.45 GHz microwave source to provide the power and a strong magnetic field of 875 Gauss. With these choices, the magnetic field and electric field strength create resonance which results in efficient power absorption. This phenomenon is different from that used in conventional RIE and PECVD reactors. In these, usually 13.56 MHz rf sources are used. At pressures typical in ECR processing, the collisions are far fewer than in rf discharges. ECR systems are capable of yielding electron densities one or two orders of magnitude higher than the 13.56 MHz rf discharges. A typical ECR system consists of a power source, transmission lines (often waveguide or coaxial cable), microwave applicator (magnetic field design) and a plasma processing chamber. Pumping requirements, mass flow controllers, pressure control, and other needs are similar to those in conventional plasma processing.

Though there are different types of microwave applicators available they all have the same basic features. Typically, the ECR set-up has two zones: a discharge zone and a processing zone. Electromagnetic energy is coupled into the discharge zone from the wave guide excited by the incident electromagnetic wave. Process gases are fed into the discharge zone, which undergo ionization and other inelastic collisions following microwave excitation. The resultant charged and neutral species mixture 'leak' out into a plasma processing zone through a screen separating the discharge and processing zones. The discharge zone is surrounded by one or more coils which produce an axial magnetic field. Here again, a number of different magnet designs are available. A typical design, as in the Plasmatherm system, consists of a multipolar arrangement with eight high strength rare earth magnets. In this arrangement, the cyclotron resonance occurs in eight distinct regions surrounding each magnet within the discharge zone.

The plasma processing zone may take one of the following three forms. In the first design, the substrate is placed entirely inside the discharge; i.e., the discharge zone and processing zone are the same. This has the advantage of high density processing with possible high rates. In a manner, this is similar to MIE with obvious differences in power coupling. In the second design, there is a separate processing chamber which is separated from the discharge zone by a screen. This

downstream configuration allows processing without much ion bombardment. The third design is different from the second in that the substrate in the processing chamber has an additional, independent bias (which may be dc or rf). This additional bias allows independent control of ion bombardment, which is needed to obtain the anisotropic etched features.

At present, commercial reactors are readily available. Though much of these are used in research, there are limited reports on the use of ECR in manufacturing. For additional details on the design of ECR equipment and technology, reference is made to refs. [3,4]. ECR has been widely used in deposition of  $\text{Si}_3\text{N}_4$  [5-7] and  $\text{SiO}_2$  [8,9]. Some examples of application to silicon etching can be found in refs. [10,11] and for III-V compounds in [12,13]. Discussion on diagnostics measurements in ECR reactors is postponed until Chapter 4.

Modeling of ECR is an extremely complex task for the reasons explained in Section 1 with regard to the coupling or interaction of various phenomena. Weng and Kushner [14] used a Monte Carlo simulation to follow the electrons in an ECR discharge and obtained electron and ion characteristics. This work did not consider any reactive plasmas or gas flow. Porteous and co-workers [15,16] modeled an argon ECR discharge using a fluid model for electrons and particle-in-cell (PIC) scheme for ion transport. This work also did not consider gas flow or density variation. But this work effectively demonstrated that one can input a power profile from experimental measurements (as long as the location of the resonance zone and its approximate width are known), rather than solving for the Maxwell's equations and still predict the plasma characteristics reasonably well. This is extraordinary since coupling the plasma transport and power deposition mechanisms is extremely cumbersome. Note that the location of the resonance zone changes with location of the magnetic coils. This is important in determining the distribution of various parameters. On the other hand, ref. 15 and 16 show that the actual width of the resonance zone itself is not that critical; the integrated absorbed power actually determines the plasma characteristics. This has been verified by our model as well.

### 3. Model Development

#### A. Governing Equations

The model consists of mass conservation equations for each component in a multicomponent mixture, momentum and energy conservation equations, and constitutive relations[17,18]. The species conservation equations are given by

$$\frac{\partial \rho_i}{\partial t} + \nabla \cdot \rho_i \mathbf{u} = -\nabla \cdot \mathbf{J}_i + R_i \quad (1)$$

Here  $\rho_i$  is the mass density of species  $i$ ,  $\mathbf{J}_i$  is the diffusional mass flux of species  $i$ , and  $R_i$  is the mass rate of production or consumption of species  $i$  from all homogeneous reactions.  $\mathbf{u}$  is the mass-averaged velocity, and  $\rho$  is the total mass density:

$$\rho \mathbf{u} = \sum \rho_i \mathbf{u}_i \quad \rho = \sum \rho_i \quad (2)$$

where  $\mathbf{u}_i$  is individual species velocity. The diffusive mass flux relative to the mass-averaged velocity is given by

$$\mathbf{J}_i = \rho_i (\mathbf{u}_i - \mathbf{u}) \quad (3)$$

It follows from Eqs. (2) and (3) that

$$\sum_i \mathbf{J}_i = 0 \quad (4)$$

Summing Eq. (1) for all species gives the total mass conservation equation, since  $\sum R_i = 0$ . Here we compute total density from  $\rho = \sum \rho_i$ , rather than using the equivalent total mass conservation equation.

We next discuss the formalism for multicomponent diffusion based on the developments by Ramshaw[19-20]. In many plasma reactor simulations (see review in ref. 16) the diffusion flux for neutral species  $i$  is assumed to be given by Fick's law:

$$\mathbf{J}_i = -\rho D_{ij} \nabla y_i \quad (5)$$

where subscript  $j$  denotes the feed gas,  $y_i$  is mass fraction, and  $D_{ij}$  is a binary diffusion coefficient for species  $i$  in the feed gas. In diode reactors, the feed gas is only weakly dissociated and constitutes the major component in the mixture. This is not the case in high density reactors. Regardless, Eq. (5) would satisfy the constraint (4) only if all  $D_{ij}$  are equal, which is too restrictive. A common practice in the treatment of multicomponent transport is to use an effective diffusion coefficient  $D_i$  for species  $i$  in the mixture in Eq. (5) instead of solving the Stefan-Maxwell equations[15]. Though there are a few different definitions for  $D_i$ , [17-19], the following is more common:

$$D_i = (1 - x_i) / \sum_{j \neq i} x_j / D_{ij} \quad (6)$$

Here  $x_i$  is mole fraction of species  $i$ . The use of Eq. (6) also does not automatically satisfy constraint (4). The usual practice is to obtain the flux for  $(N-1)$  species using Eq. (5) with  $D_i$  (instead of  $D_{ij}$ ) and the flux of the last species from Eq. (4). Ramshaw[19] points out that such an asymmetric treatment is unwarranted and derives an expression for the diffusion flux which satisfies Eq. (4).

$$\mathbf{J}_i = -c M_i D_i \nabla x_i + c y_i \sum_j M_j D_j \nabla x_j \quad (7)$$

Here  $c$  is mixture concentration given by  $c = \rho / \bar{M}$  where  $\bar{M}$  is mixture molecular weight

$\left( = \sum_j M_j x_j \right)$ .  $M_i$  is molecular weight of species  $i$ . Recognizing  $x_i = y_i \bar{M} / M_i$ , it is easy to see

that Eq. (7) satisfies constraint (4). Eq. (7) for  $\mathbf{J}_i$  is valid for a single temperature system in the absence of thermal and pressure diffusion effects, and charged species. An expression for  $\mathbf{J}_i$  with thermal and pressure diffusion is given by Ramshaw[20]; but these phenomena are normally very small in plasma processing reactors. However, we do need  $\mathbf{J}_i$  in a multitemperature, multi-component mixture that contains charged species. We will return to this later.

The chemical reaction term  $R_i$  in Eq. (1) is defined next. There are a total of  $N_R$  reactions in progress involving a total of  $N$  species. They are represented by

$$\sum_{i=1}^N v_{ij}^+ \chi_i \rightarrow \sum_{i=1}^N v_{ij}^- \chi_i \quad j=1, N_R \quad (8)$$

Here  $\chi_i$  is the chemical symbol for species  $i$ .  $v_{ij}^+$  and  $v_{ij}^-$  are stoichiometric coefficients. Further, we define  $v_{ij} = v_{ij}^- - v_{ij}^+$ . The mass rate of net production of species  $i$  is given by

$$R_i = M_i \sum_{j=1}^{N_R} v_{ij} k_j \prod_{i=1}^N c_i^{v_{ij}} \quad (9)$$

If any of the reactions (8) proceed also in the reverse direction, Eq. (9) must be modified to include the reverse rates. Neutral reaction rate constants typically take the Arrhenius form:

$k = k_0 T^\beta \exp(-E_a / R_g T)$  where  $E_a$  is activation energy,  $R_g$  is gas constant, and  $T$  is the temperature of the neutrals. For electron impact reactions, the rate constant needs to be expressed as a function of electron mean energy for use in Eq. (9). Note that discharge physics fluid models do not solve

for the electron energy distribution function (EEDF) or the rate constants for electron inelastic collisions unlike kinetic schemes; rather they require such information as input[18]. The needed kinetic data can be generated using a Boltzmann equation solver; a discussion can be found in ref. 18.

Computation of the mass-averaged velocity  $\mathbf{u}$  requires a momentum equation:

$$\frac{\partial}{\partial t} \rho \mathbf{u} + \nabla \cdot \rho \mathbf{u} \mathbf{u} = -\nabla p + \nabla \cdot \Pi + \rho \mathbf{g} \quad (10)$$

Here  $p$  is pressure,  $\Pi$  is the viscous stress tensor, and  $\mathbf{g}$  is the gravitational force vector.

The multicomponent mixture in a plasma processing reactor consists of electrons, ions, and neutrals in a state of thermal nonequilibrium. Therefore, we need separate energy equations for each of these types of species. First, the energy equation for neutrals is written in terms of their temperature  $T$ [17]:

$$\rho c_p \left[ \frac{\partial T}{\partial t} + \mathbf{u} \cdot \nabla T \right] = \nabla \cdot K \nabla T + \mathbf{u} \cdot \nabla p - \sum_i^N c_{pi} \mathbf{J}_i \cdot \nabla T - \sum_{i=1}^N h_i R_i + Q_{ex} \quad (11)$$

Here  $c_p$  is the mixture specific heat at constant pressure,  $K$  is mixture thermal conductivity, and  $h_i$  is enthalpy of species  $i$  per unit mass. We have ignored viscous dissipation effects and radiation. The third term on the right is the interdiffusional energy flux. The fourth term is due to chemical reactions. The heat gain by the gas from elastic collision with charged species and charge-exchange collisions with ions[16] is represented by  $Q_{ex}$ :

$$Q_{ex} = \frac{3}{2} k (T_e - T) n_e \sum_i f_i 2m_e / m_i + (k T_e - 3/2 k T) n_e f_{ce} \quad (12)$$

Here  $k$  is Boltzmann constant,  $m$  is species mass,  $T_e$  and  $T_+$  are electron and ion temperatures, respectively,  $f_i$  is frequency for electron elastic collision with neutral species  $i$ , and  $f_{ce}$  is the charge exchange collision frequency.  $n$  is species number density given by  $\rho = nm$ . Subscripts  $e$  and  $+$  represent electrons and positive ions.

The thermodynamic state relation must reflect the nonequilibrium nature of the multicomponent mixture in plasma processing.

$$p = \sum_i p_i + \sum_{\text{ion}} p_j + \sum p_e = kT \sum_i n_i + k \sum_{\text{ion}} n_j T_j + n_e k T_e \quad (13)$$

The last term due to electrons is critical in ECR and ICP reactors. The ratio  $n_e/n$  may be of  $O(10^{-3})$  or higher. However,  $T_e/T$  may be  $O(10^2)$  in some parts of the reactor, making the last term significant.

Now we return to issues related to charged species. The integration of the equations inside the sheaths and solution of Poisson's equation to obtain sheath potential make the plasma transport problem difficult to solve numerically. Instead, here we assume a quasineutral plasma. This is appropriate everywhere except the very thin sheaths. We compute the electron density from

$$n_e = \sum_i q_i n_i \quad (14)$$

where  $q_i$  is the ion charge. The ion conservation equations are also given by Eq. (1). We need to redefine  $J_i$  for ions and neutrals suitable for use in a multitemperature, multicomponent mixture. The individual velocity  $u_i$  of a neutral species is determined by concentration gradients only (in the absence of thermal and pressure gradients and body forces). For charged species, the electrostatic forces must be accounted for in evaluating  $u_i$ . In this case,  $J_i$  would consist of an ordinary diffusion term and a drift term proportional to the electric field, if inertial terms and time rate of change of  $u_i$  are neglected in the charged species momentum equation. In the context of multitemperature

plasmas and with the need to satisfy Eq. (4) in a multicomponent mixture, Ramshaw[19] derives an expression for  $\mathbf{J}_i$  to be used in Eq. (1) for all neutral species and ions except electrons:

$$\begin{aligned} \mathbf{J}_i = & -\frac{p}{R_g T} D_i \nabla \left( \frac{R_g T}{p} \rho_i \right) + \frac{y_i p}{R_g T} \sum_{j \neq e} D_j \nabla \left( \frac{R_g T \rho_j}{p} \right) \\ & + \frac{A}{R_g T} \left[ q_i D_i \rho_i - y_i \sum_{j \neq e} q_j D_j \rho_j \right] \mathbf{E} \quad \text{for all } i \neq e \end{aligned} \quad (15)$$

Here  $\mathbf{E}$  is the space charge induced electric field, and  $A$  is Avogadro constant. Several comments about Eq. (15) are in order. First, Eq. (15) is written for a two temperature ( $T$  and  $T_e$ ) system. Assuming  $T_{ion} = T$  does not affect the fluxes much or the thermodynamic state relation Eq. (13) and makes the expression (15) a little simpler. Second, Eq. (15) satisfies Eq. (4). In addition to the  $\mathbf{E}$  term, Eq. (15) looks complex due to the thermodynamic state relation. That is, the total concentration  $c$  is no longer given by  $p/R_g T$ . Indeed, for a single temperature, multicomponent mixture without charged species, Eq. (15) reduces to Eq. (7). Finally, the form of the flux relation in Eq. (15) is more complex than expressions widely used due to its self-consistent satisfaction of Eq. (4). The additional effort incurred to evaluate Eq. (15) in Eq. (1) is well spent since mass and flux conservation is ensured.

The total current  $\mathbf{J}_t$  in the plasma is given by

$$\mathbf{J}_t = \sum_i \frac{q_i}{m_i} \mathbf{J}_i \quad (16)$$

This relation defines the current density with respect to the mass averaged velocity. As pointed out in ref. 21, because of the neutrality condition, there is no distinction between this current density and that in the laboratory frame. Now, we can use Eqs. (15) and (16) with the ambipolar constraint to obtain  $\mathbf{E}$

$$\mathbf{E} = \frac{p \sum_i q_i D_i \nabla x_i}{\sum_i q_i^2 D_i n_i} \quad (17)$$

which is a well-known expression for the space charge electric field[22]. In Eq. (17), the electron terms dominate the sums and an order of magnitude analysis[21] shows

$$\mathbf{E} = -\frac{1}{n_e} \nabla n_e k T_e \quad (18)$$

Setting  $\mathbf{J}_e = 0$  would be acceptable with respect to mass flux, due to the small mass of electrons, but would be improper when computing current density. Though an expression equivalent to Eq. (15) for electrons is possible, a simpler approach is to obtain  $\mathbf{J}_e$  from

$$\mathbf{J}_e = m_e \sum_i \frac{q_i \mathbf{J}_i}{m_i} \quad (19)$$

A thorough discussion on this subject can be found in ref. 21.

In writing an energy conservation equation for the electrons, we assume that the electron thermal energy is much larger than its kinetic energy ( $3/2 k T_e \gg 1/2 m_e u_e^2$ ).

$$\begin{aligned} \frac{\partial}{\partial t} (3/2 n_e k T_e) + \nabla \cdot n_e \mathbf{u}_e 3/2 k T_e &= -n_e \mathbf{u}_e \cdot \mathbf{E} \\ -\nabla \cdot p_e \mathbf{u}_e + \nabla \cdot K_e \nabla T_e - \sum_j R_{ej} H_{ej} + P_{ext} \end{aligned} \quad (20)$$

Here,  $\mathbf{u}_e$  is the electron velocity given by  $\mathbf{u} + \mathbf{J}_e / \rho_e$  from Eq. (3). The mass-averaged velocity  $\mathbf{u}$  and diffusive velocity  $\mathbf{J}_e$  are known from other equations described earlier.  $K_e$  is electron thermal

conductivity. The fourth term on the right side of Eq. (20) represents energy loss due to inelastic collisions.  $P_{ext}$  is the external power coupled to the plasma, which can be self-consistently determined from the solution to Maxwell's equations. Some examples of electromagnetic equation solvers and integration with electron dynamics can be found in refs. [23,24]. In the present work we solve Eq. (20) with an assumed power profile. Also, an equation analogous to Eq. (20) for ions is not written at present. Instead, experimentally measured ion temperature is used to model gas heating due to charge exchange collisions.

The numerical algorithm to solve the multi-dimensional equations is described below. The procedure to solve the governing equations is a consistently split linerized block implicit scheme originally developed by Briley and McDonald [25] at SRA. The basic algorithm has been further developed and applied to both laminar and turbulent fluid flows. The method can be outlined as follows: the governing equations in a dimensionless form are replaced by an implicit time difference approximation. Terms involving nonlinearities at the unknown time level are linearized by Taylor series expansion about the solution at the previous known time level, and spatial difference approximations are introduced. The result is a system of multi-dimensional coupled (but linear) difference equations for the dependent variables at the unknown or implicit time level. To solve these difference equations, the Douglas-Gunn procedure for generating alternating direction implicit (ADI) splitting schemes is used. This ADI splitting technique leads to systems of coupled linear difference equations having narrow block-banded matrix structures which can be solved efficiently by standard block-elimination methods.

## B. One-dimensional Model

The governing equations presented above need to be solved in at least two dimensions to account for the complex geometry of commercial reactors and etch/deposition uniformity related issues. This is a time-consuming task, due to the coupling of gas flow and charged species dynamics, widely disparate time scales of various physical phenomena, and the large number of conservation equations when multiple neutral and ionic species are considered. Recently, however, models have been proposed[26-28] (to be discussed next under Section C) wherein volume-averaged balance equations or zero-dimensional versions of the governing equations in Section A are used. Such lower-order models require very little computational time and provide valuable

information regarding plasma scaling laws and insight into mechanisms on how the applied power is expended through various collisions, ion acceleration, etc. In the same spirit, we develop a one-dimensional model here by radially averaging the governing equations and study ECR discharge dynamics in the flow (axial) direction.

We define a radially-averaged variable  $\bar{\phi}$  as

$$\bar{\phi} = \frac{\int_0^{R(z)} \phi r dr}{\int_0^{R(z)} r dr} \quad (21)$$

$R(z)$  is local radius. Note that radius can vary from source to the process chamber. Terms involving products of two or more variables, such as  $\phi_1 \cdot \phi_2$  are treated as  $\bar{\phi}_1 \cdot \bar{\phi}_2$  in both the source/sink terms and axial derivatives. Using this procedure, equations (1), (10), (11) and (20) can be radially averaged. In doing so, application of radial boundary conditions at  $r = R(z)$  results in a pseudo-volumetric term in the equation appropriately weighted by the surface to volume ratio. (The boundary condition at  $r = 0$ , which is  $\frac{\partial \phi}{\partial r} = 0$ , does not result in an additional term.) First, we list only such additional terms obtained in each equation.

The one-dimensional species mass conservation equation has a surface reaction term  $\frac{2}{R(z)} r_i$  where  $r_i$  is the net production rate of species  $i$  through surface reactions. The surface reaction rate constant  $k_s$  for neutrals may be expressed in terms of a reactive sticking coefficient,  $\gamma$ , as  $k_{s,i} = \gamma_i (R_g T / 2\pi M_i)^{0.5}$ . The positive ions reach the Bohm velocity at the sheath edge, while the negative ions are repelled from the walls due to the positive plasma potential. Recognizing the deviation of the positive ion density at the sheath edge from that in the plasma, Lee and Lieberman[26] introduced a correction factor  $h_r$  for the wall flux ( $= h_r n_+ u_{\text{Bohm}}$ ). Expressions for  $h_r$  in simple electropositive discharges, as well as multi-ion discharges, are given in ref. 26. The

electron loss to the radial wall is equal to the ion wall flux under the ambipolar constraint. The corresponding electron energy loss now appears as a sink term in the one-dimensional equivalent of Eq. (20).

The additional term due to radial averaging in the axial momentum equation is  $8\mu u_z / (1 + C_s)R(z)^2$ , where  $\mu$  is mixture viscosity,  $u_z$  is axial mass-averaged velocity and  $C_s$  is a coefficient of slip or slip correction[29] given by  $8\lambda / 3R$ .  $\lambda$  is the gas mean free path. The sink term appearing in the gas energy equation due to radial averaging is related to heat loss from the gas to surroundings. This term can be written with the aid of an overall heat transfer coefficient  $U$  as  $\frac{2}{R(z)} U(T - T_a)$  where  $T_a$  is ambient temperature. If we represent the heat loss process by a network of resistors in series,  $U$  is given by [30]

$$U = \frac{1}{1/h_i + \frac{\Delta x}{K_w} + 1/h_o} \quad (22)$$

Here,  $h_i$  and  $h_o$  are convective heat transfer coefficients for inside and outside the chamber.  $h_i$  can be written as  $1/4 kn_g u_{th}$  using kinetic theory, where  $k$  is Boltzmann constant,  $n_g$  is gas number density, and  $u_{th}$  is gas thermal velocity. Empirical relations for  $h_o$  can be found in heat transfer texts[30]. The middle term in Eq. (22) represents the conduction through the wall and quartz liner, if any.

With the above additional terms, the exact form of the radially-averaged one-dimensional equations is given below. Equations (23) - (26) represent conservation of individual species mass, mixture momentum, energy of the heavy species ( neutrals and ions), and electron energy, respectively.

$$\frac{\partial p_i}{\partial t} + \frac{1}{A} \frac{\partial}{\partial z} A \rho_i u_z = - \frac{1}{A} \frac{\partial}{\partial z} A J_{i,z} + r_{v,i} + \frac{2}{R} r_{s,i} \quad (23)$$

$$\frac{\partial \rho u_z}{\partial t} + \frac{1}{A} \frac{\partial}{\partial z} A \rho u_z^2 = - \frac{\partial p}{\partial z} - \frac{8 \mu u_z}{R^2 (1 + C_s)} + \frac{\partial}{\partial z} \mu A \frac{\partial u_z}{\partial z} + \rho g \quad (24)$$

$$\begin{aligned} \rho c_p \frac{\partial T}{\partial t} + \frac{\rho c_p u_z}{A} \frac{\partial AT}{\partial z} &= \frac{1}{A} \frac{\partial}{\partial z} \left( AK \frac{\partial T}{\partial z} \right) + \frac{2}{R} q_w + u_z \frac{\partial p}{\partial z} \\ &\quad - \sum_i c_{p_i} J_{i,z} \frac{\partial T}{\partial z} - \sum_i h_i r_{v,i} + Q \end{aligned} \quad (25)$$

$$\begin{aligned} \frac{\partial}{\partial t} \left( \frac{3}{2} n_e k T_e \right) + \frac{1}{A} \frac{\partial}{\partial z} \left( \frac{5}{2} A n_e k T_e u_{e,z} \right) &= - e n_e u_{e,z} E_z + \frac{1}{A} \frac{\partial}{\partial z} \left( AK_e \frac{\partial T_e}{\partial z} \right) \\ &\quad + \frac{2}{R} q_{e,w} - \sum_j r_{e,j} H_j + P_{ext} \end{aligned} \quad (26)$$

Boundary conditions for the solution of the above equations in the axial direction are as follows. At  $z = 0$ , the incoming mass flux of each species is specified along with the specification of gas temperature, and extrapolation of pressure since the inlet flow is subsonic. The pressure is specified downstream. Note that since  $p$  is not an explicit dependent variable, Eq. (13) is used to relate pressure to other dependent variables. The species density (or mass flux) and gas temperature are extrapolated at  $z = L$ . For electron energy, in the absence of secondary electron emission at the quartz window and other walls, an energy balance at the boundary reduces to a zero gradient of the electron temperature.

We have developed a code based on a fully implicit finite difference scheme to solve all the governing equations in a coupled manner. The general numerical procedure adopted in the code is described in ref. 31. A brief summary was also provided at the end of Section A. Variation in cross-sectional area is included in the equations. The code allows for multiple injection locations for feed gases, which is common in ECR deposition reactors. The substrate positioned at any  $z$ -location is treated as a sink in all governing equations. Transport properties such as viscosity,

thermal conductivity, and binary diffusivity are computed using well-known procedures[17]. The transition regime diffusivity is computed from molecular and Knudsen diffusivities. Thermo-chemical properties for various chemical species are obtained from JANNAF tables[32]. Input of chemical reactions in the gas phase and on the surfaces can be done using alphanumeric characters. The code was developed in a modular fashion to easily accommodate future enhancements.

### C. Zero-dimensional Model

The plasma modeling community has recently focused on developing models which require minimal computational resources and, nevertheless, capture essential features. Volume-averaged conservation equations representing global mass and energy balances form an example of such an approach. These are called zero-dimensional models, since they deal with volume-averaged quantities and hence, provide no information on spatial distribution. These models can provide valuable information rapidly on average densities and temperatures as a function of system parameters. Average etch and deposition rates can also be obtained. A detailed description of the approach is given below.

We consider a plasma source chamber of radius,  $r$ , length,  $L$ , and volume  $V (= \pi r^2 L)$  where the plasma is generated. The total surface area  $A$  may consist of wall ( $A_s$ ) and wafer ( $A_w$ ) areas. The wafer may be processed in the source chamber or in a separate process chamber. If there is a separate process chamber downstream, as in ECR, it may be analyzed in a cascading fashion; i.e., process chamber inflow conditions will be the outflow properties computed in the source chamber analysis. It is not easy to include the nature and details of power deposition, associated magnetic field effects, etc. in a zero-dimensional volume-averaged model; plasma power input is simply treated as a model input variable. In this sense, there is nothing in the model that distinguishes ICP and ECR reactors and what follows is an analysis of a generic high density plasma reactor.

**Species Mass Conservation:** A mass balance for each of the neutral and ionic species in the plasma is written as

$$\dot{m} (y_{i,in} - y_i) + V M_i \sum_j R_{ij} + A M_i \sum_k S_{ik} = 0 \quad i = 1, I \quad (27)$$

Here, the subscript 'in' denotes inlet conditions.  $I$  is the total number of neutral and ionic species.  $y_i$  is the mass fraction of species  $i$  ( $y_i = \rho_i / \rho$ );  $\rho_i$  is the mass density of species  $i$  given by  $n_i m_i$  where  $n_i$  and  $m_i$  are the species number density and mass. Other notations are as follows.  $\dot{m}$  is the total mass flow rate;  $M_i$  is the molecular weight;  $R_{ij}$  is the molar homogeneous reaction rate of species  $i$  in reaction  $j$ ;  $S_{ik}$  is the molar heterogeneous reaction rate of species  $i$  in surface reaction  $k$ . The terms in Eq. (27) represent changes due to the flow, and species production/consumption due to volume and surface reactions, respectively. In principle, the last term in Eq. (27) can be written as two independent contributions from wall and wafer reactions as they may differ in nature. The net rate of production from volume reactions  $R_{ij}$  is written as

$$R_{ij} = (v''_{ij} - v'_{ij}) \left[ k_{fj} \prod_{i=1}^{i=I} (\rho y_i / M_i)^{v'_{ij}} - k_{rj} \prod_{i=1}^{i=I} (\rho y_i / M_i)^{v''_{ij}} \right] \quad (28)$$

Here  $v_{ij}$  is stoichiometric coefficient of species  $i$  in reaction  $j$ . The single and double primes denote reactant and product, respectively.  $k_{fj}$  and  $k_{rj}$  are forward and reverse rate coefficients for elementary reaction step  $j$ . Eq. (28) represents a more complete form of Eq. (9). The surface reaction rate is written in a similar manner.

The mass flow rate  $\dot{m}$  in Eq. (27) is taken as constant, though in principle, surface reactions may result in a loss of mass. In such a case, the first term in Eq. (27) would be written as  $\dot{m}_{in} y_{i,in} - \dot{m} y_i$ , and  $\dot{m}$  then can be obtained from a total mass balance which is the sum of Eq. (27) over all  $I$  species:

$$\dot{m}_{in} - \dot{m} + A \sum_i M_i \sum_k S_{ik} = 0 \quad (29)$$

The plasma is assumed to be neutral and thus, the electron number density is obtained from

$$n_e = \sum_{i=1}^I q_i n_i \quad (30)$$

where  $q_i$  is the charge of species  $i$ .

**Thermodynamic Relation:** The gas density,  $\rho$ , is computed from the thermodynamic relation:

$$\begin{aligned} p &= \sum_{i \neq e} p_i + \sum p_e \\ &= RT_g \rho \left[ \sum_{i \neq e} \frac{y_i}{M_i} + \frac{T_e}{T_g} \frac{y_e}{M_e} \right] \end{aligned} \quad (31)$$

where  $p$  is the total reactor pressure,  $R$  is the universal gas constant,  $T_g$  is the gas temperature, and  $T_e$  is electron temperature. The second term due to the electrons is usually negligible in diode reactors since the plasma is very weakly ionized. In contrast, fractional ionization  $n_e / n$  may be of  $O(10^{-2})$  in high density discharges with  $T_e / T_g$  nearly of  $O(10^2)$ .  $n$  is the total number density in the reactor. Hence, contribution of electron pressure to the total cannot be ignored, especially at low pressures and high power levels. In principle, the thermodynamic relation in (31) may be written to recognize an ion temperature also, however the effect is expected to be negligible. The principles behind the development of Eqs. (29) - (31) are the same as in the one-dimensional model discussed in the previous section.

**Plasma Power Balance:** The power balance in the plasma source takes the form:

$$P_{ext} = P_e + P_{ion} \quad (32)$$

where  $P_{ext}$  is the external applied power, and  $P_e$  and  $P_i$  are power deposited to electrons and ions, respectively. While it is possible to express  $P_e$  in terms of electron conduction current and average

electric field, we obtain  $P_e$  from an electron energy balance assuming that the electron-ion volume recombination is negligible:

$$(Qn_e \varepsilon_e)_{in} - Qn_e \varepsilon_e + P_e - V\tilde{N} \sum_j R_{ej} H_j - 3\left(\frac{m_e}{m}\right) v_{el} V n_e k (T_e - T_g) - A \Gamma_e (\varepsilon_e + 0.5kT_e) = 0 \quad (33)$$

Here  $Q$  is flow rate given by  $\dot{m}/\rho$ ,  $\varepsilon_e$  is electron mean thermal energy ( $= 3/2 kT_e$ ) where  $k$  is Boltzmann constant,  $\tilde{N}$  is Avagodro number,  $R_{ej}$  is rate of electron impact reaction  $j$ ,  $H_j$  is the corresponding threshold energy,  $m$  is mixture-average mass,  $v_{el}$  is the elastic collision frequency, and  $\Gamma_e$  is electron wall flux. The terms in Eq. (33) represent electron energy from inflow and outflow, energy gain from external source, energy loss from all inelastic collisions, energy loss from elastic collisions, and energy lost due to electron wall recombination, respectively. The energy of electrons at the wall is  $\varepsilon_e + 1/2 mv^2$  where  $v$  is electron directed velocity; we assume that the electrons at the wall are thermal and rewrite their energy as  $\varepsilon_e + 0.5kT_e$ . The electron wall flux  $\Gamma_e$  must equal the positive ion wall flux, assuming that the massive negative ions are excluded from the wall due to the positive plasma potential.

$$\Gamma_e = \sum \Gamma_+ = (A_{eff}/A) \sum n_+ u_{B,+} \quad (34)$$

Here, the subscript + indicates a positive ion and  $\Sigma$  indicates sum over all positive ions.  $u_B$  is the Bohm velocity given by  $(kT_e / m+)0.5$ . Implicit in Eq. (34) is the assumption that the ion flux  $\Gamma_+$  at the wall is the same as that at the edge of the sheath.  $A_{eff}$  is an effective area, as suggested in ref. 26 and discussed in Section B, to account for the deviation of sheath edge ion density from that at the center.

$$A_{eff} = A_R h_R + A_L h_L \quad (35)$$

where  $A_R$  and  $A_L$  are radial and axial surface areas. The correction factors  $h_R$  and  $h_L$  are:

$$\begin{aligned} h_R &= 0.8 / (4.0 + r/\lambda)^{0.5} \\ h_L &= 0.86 / (3.0 + 2L/\lambda)^{0.5} \end{aligned} \quad (36)$$

where  $\lambda$  is the mean free path based on charge exchange collisions.  $h_R$  and  $h_L$  reduce to 0.4 and 0.5 at the free fall limit.

The ion power deposition,  $P_{ion}$ , is given by

$$P_{ion} = A \sum \Gamma_+ \Delta\psi \quad (37)$$

where  $\Delta\psi$  is the driving potential equal to the difference between the plasma and wall potentials.  $\Delta\psi$  can be estimated from Eq. (34) by recognizing that

$$\Gamma_e = (n_e/4)v_{e,th} \exp(-\Delta\psi/kT_e) \quad (38)$$

where  $v_{e,th}$  is electron thermal velocity,  $(8kT_e/\pi m_e)^{0.5}$ . Combining Eqs. (34) and (38), we get

$$\Delta\psi = -kT_e \cdot \ln \left[ \frac{(A_{eff}/A) \sum n_+ u_{B+}}{(n_e/4)v_{e,th}} \right] \quad (39)$$

Combining Eqs. (32), (33), (34), (37) and (38), we get the final form of the power balance:

$$\begin{aligned}
P_{ext} + (Qn_e \varepsilon_e)_{in} - Qn_e \varepsilon_e - V \tilde{N} \sum_j R_{ej} H_j \\
- 3(m_e/m) v_{e\ell} V n_e k (T_e - T_g) - A_{eff} (\varepsilon_e + 0.5 k T_e) \sum n_+ u_{B+} \\
+ A_{eff} k T_e \cdot \ln \left[ \frac{(A_{eff}/A) \sum n_+ u_{B+}}{(n_e/4) v_{e,th}} \right] \cdot \sum n_+ u_{B+} = 0
\end{aligned} \tag{40}$$

**Gas Energy Balance:** In high density discharges, it is well known that plasma heating of the gas can result in high gas temperatures[33,34]. We write a gas energy balance in order to predict the gas temperature:

$$\begin{aligned}
(\dot{m} c_p T_g)_{in} - \dot{m} c_p T_g + 3(m_e/m) v_{e\ell} V n_e k (T_e - T_g) \\
+ v_{ce} V n_+ 3/2 k (T_+ - T_g) + V \sum_i \bar{h}_i M_i \sum_j R_{ij} - U A (T_g - T_a) = 0
\end{aligned} \tag{41}$$

Here  $c_p$  is mixture specific heat,  $\bar{h}_i$  is species enthalpy per unit mass,  $v_{ce}$  is charge exchange collision frequency,  $T_+$  is ion temperature,  $U$  is an overall heat transfer coefficient, and  $T_a$  is ambient temperature. The terms in Eq. (41) represent sensible heat associated with gas inflow and outflow, heat gain due to electron-gas elastic collisions, heat gain from charge exchange collisions with ions, heat of all other chemical reactions, and finally, heat loss to the ambient, respectively. The last term is written using an overall heat transfer coefficient [30], as before in the 1-d model, since the wall temperature is unknown.

In summary, the reactor model consists of Eqs. (27), (29), (30), (40) and (41), augmented with thermodynamic relation (31). We developed a code called REAC to solve these equations. REAC is a zero-dimensional reactor analysis code to study plasma and non-plasma reactors. The code has an interpreter that allows input of volume and surface reactions using alphanumeric characters. REAC computes thermochemical properties using the NASA Lewis data base. The reverse rate constants are related to equilibrium rate constants ( $k_r = k_f/k_{eq}$ ) which in turn are

computed from a knowledge of standard-state Gibbs free energy. For electron impact reactions, REAC requires rate constants as a function of mean electron energy; if this information is not readily available, a companion zero-dimensional Boltzmann solver may be used to compute the electron energy distribution function (eedf) and rate constants.

#### **D. Two-dimensional Fluid Flow Analysis**

Throughout this project, we used both 0-d and 1-d models extensively to analyze ECR problems. A completely coupled 2-d analysis that consists of the gas flow, gas heat transfer, plasma dynamics, microwave power coupling, and magnetic field effects is beyond the scope. Indeed, no such capability is available with any research group. To augment the information from the lower order models, we also performed two-dimensional gas flow computations. These were done using SRA's multi-dimensional fluid flow code called MINT. This code solves 2-d, as well as 3-d, equations for gas momentum, energy, and multiple species mass conservation.

#### 4. Experimental Data

Plasma and surface characterization works are needed for the purpose of model input generation, knowledge of chemistry, and for model validation. In this chapter, the experimental data gathered from several sources are discussed. Much of the data is from collaborators known to the PI, which also later appeared in the published literature.

Argon is widely used in diagnostic studies because of its inertness and well-known collision cross-sections. In practice, it is an additive gas used in etch and deposition feed streams. Bowden [35] presents the following data generated by Thomson scattering measurements of on-axis electron density and electron temperature in an ECR chamber.

Table 4.1 Plasma parameters in an argon discharge at 570 W of microwave power.

Pressure (mTorr)	$n_e$ ( $10^{11} \text{ cm}^{-3}$ )	$T_e$ (eV)
0.5	4.0	4.05
1.0	6.5	3.20
2.0	6.6	3.10
4.0	7.0	2.30

Table 4.2 Plasma parameters in argon at 1 mTorr

Power (W)	$n_e$ ( $10^{11} \text{ cm}^{-3}$ )	$T_e$ (eV)
300	2.15	2.00
400	4.00	2.30
500	5.00	3.30
600	5.50	2.35
700	6.50	2.50

While the above data correspond to single point measurements on-axis of the chamber, our collaborator, Chris Constantine of PlasmaTerm, an ECR equipment manufacturer, was able to provide this contract Langmuir probe data taken above the wafer. Figure 4.1 shows the radial variation of electron density over an 8" wafer. The electron density profile is somewhat ambipolar-like. Also shown in this figure is silicon etch rate across an 8" wafer.

Additional data on argon was obtained from the work of Steve Gorbatkin of Oak Ridge National Laboratory. These data were taken at the ECR location inside the source chamber and just above the wafer in the process chamber. The data are reproduced in Figs. 7.1 (pressure), and 7.4 (electron density and temperature) later in Chapter 7. The pressure measurements allowed us to validate the gas flow part of the computer model. It is important to note that in ECR plasmas, unlike in RIE and PECVD, the pressure is not constant from the inlet to the exhaust. Indeed, at pressures below 3 mTorr, there is as much as 50% pressure drop from the inlet to the turbopump. In that sense, ECR reactors need pressure sensors in more than one location.

$\text{CF}_4$  is an important etching gas for silicon and is normally used in a mixture with  $\text{O}_2$  and argon. K. Ashtiani (currently at Materials Research Corporation), in a collaboration, provided SRA electron density and radical concentration data. His electron density data was obtained using microwave interferometry. The data listed below in Table 4.3 is for the process chamber at every 5 cm interval.

**Table 4.3 Microwave interferometry data in  $\text{CF}_4$  at 2 mTorr**

Power (W)	Electron density ( $10^{10} \text{ cm}^{-3}$ ) at every 5 cm
500	10.3, 6.69, 4.32, 3.28, 2.44, 2.02, 1.61, 1.19, 0.56, 1.06, 0.39
600	17.2, 10.7, 7.45, 5.61, 4.18, 3.15, 2.44, 1.7, 1.17, 1.23, 0.65
700	24.8, 16.0, 11.0, 8.37, 6.25, 4.68, 3.72, 3.16, 2.63, 1.88, 0.98
800	33.3, 22.1, 14.3, 10.0, 7.93, 5.56, 4.56, 3.39, 2.59, 1.75, 1.06

## 8 inch ECR Uniformity Study

### Electron Density and Etch Rate

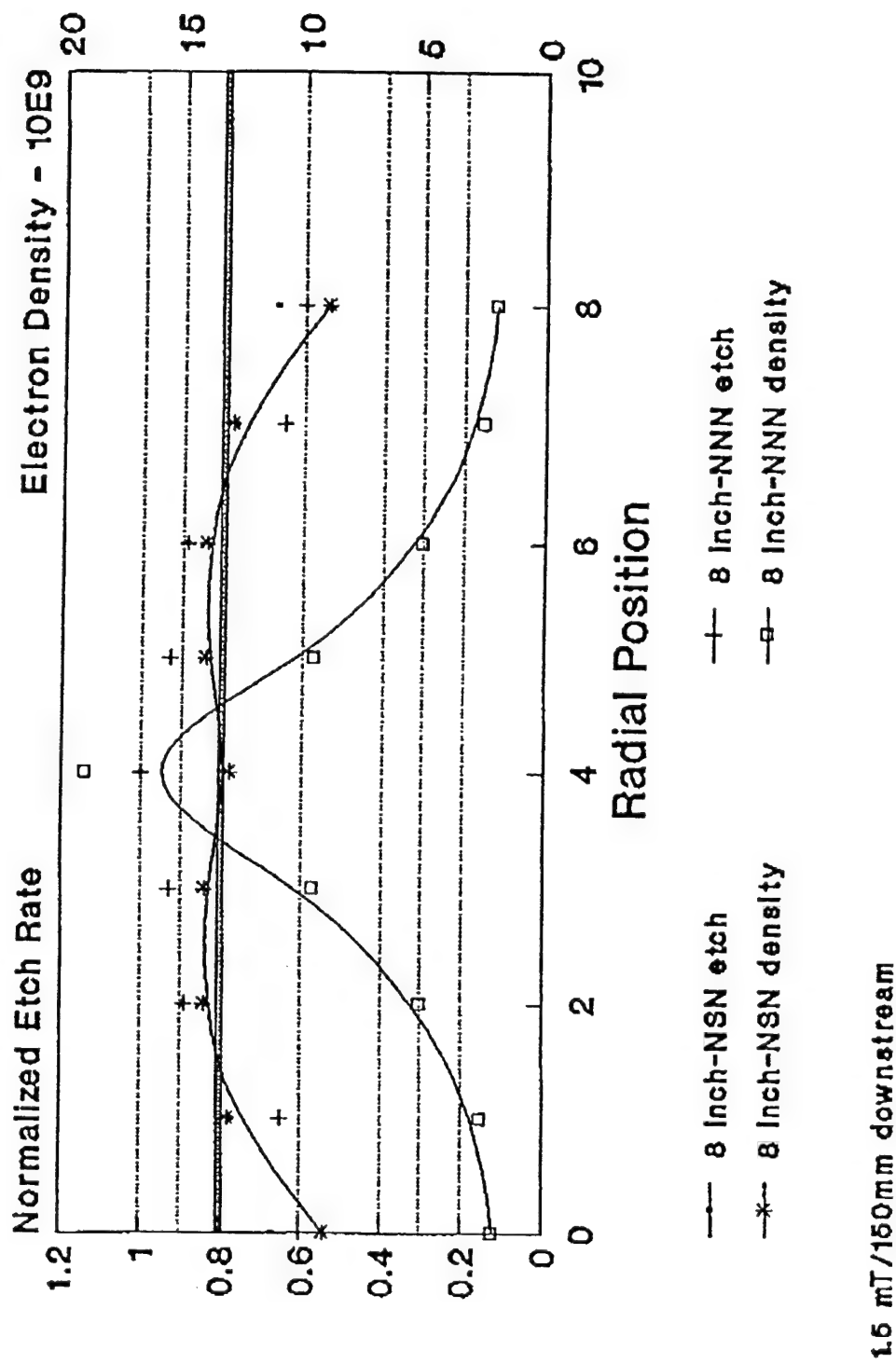


Fig. 4.1 Radial profiles of electron density in an 8" PlasmaTherm ECR reactor. Also shown is etch rate uniformity (from C. Constantine, PlasmaTherm).

Ashtiani also made measurements of radical densities. His data on F and  $\text{CF}_2$  measurements are given in Fig. 4.2.

Chlorine is an important etch gas used in etching of both silicon and GaAs. Dr. K. Ono of Mitsubishi provided us with Langmuir probe data for electron density and temperature, which are produced in Figs. 4.3 - 4.5. Figure 4.3 shows axial variation of  $n_e$ ,  $T_e$ , and plasma potential in 0.8 mTorr, 900 W chlorine ECR plasma. The density shows a peak at the ECR resonance region. The electron temperature in the source is as high as 8 eV. The plasma potential near the wafer position is only about 10 V. Figure 4.4 is a set of analogous plots at 0.24 mTorr. Figure 4.5 shows radial profiles of density and temperature just above the wafer. The electron temperature is nearly uniform, while the electron density exhibits a parabolic profile.

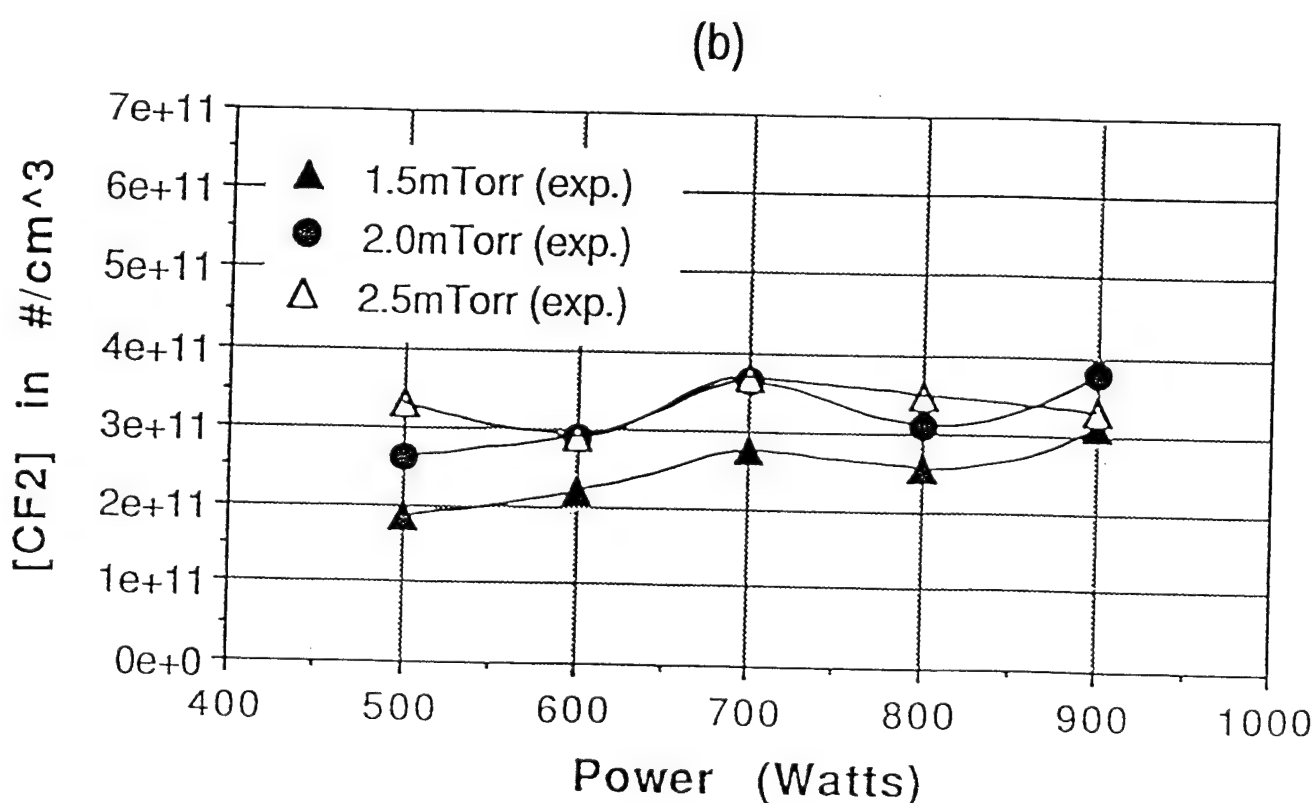
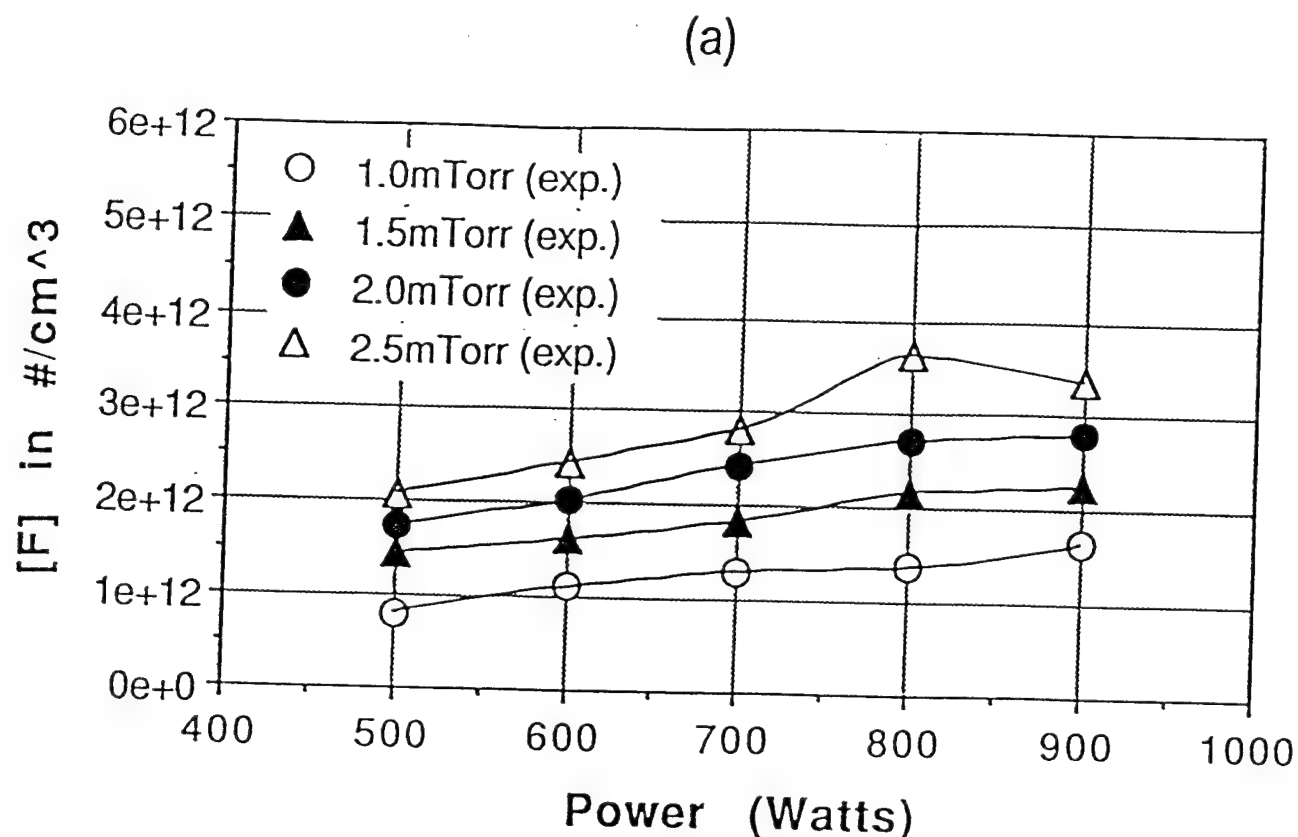


Fig. 4.2 F and  $\text{CF}_2$  densities in an ECR  $\text{CF}_4$  discharge measured by K. Ashtiani.

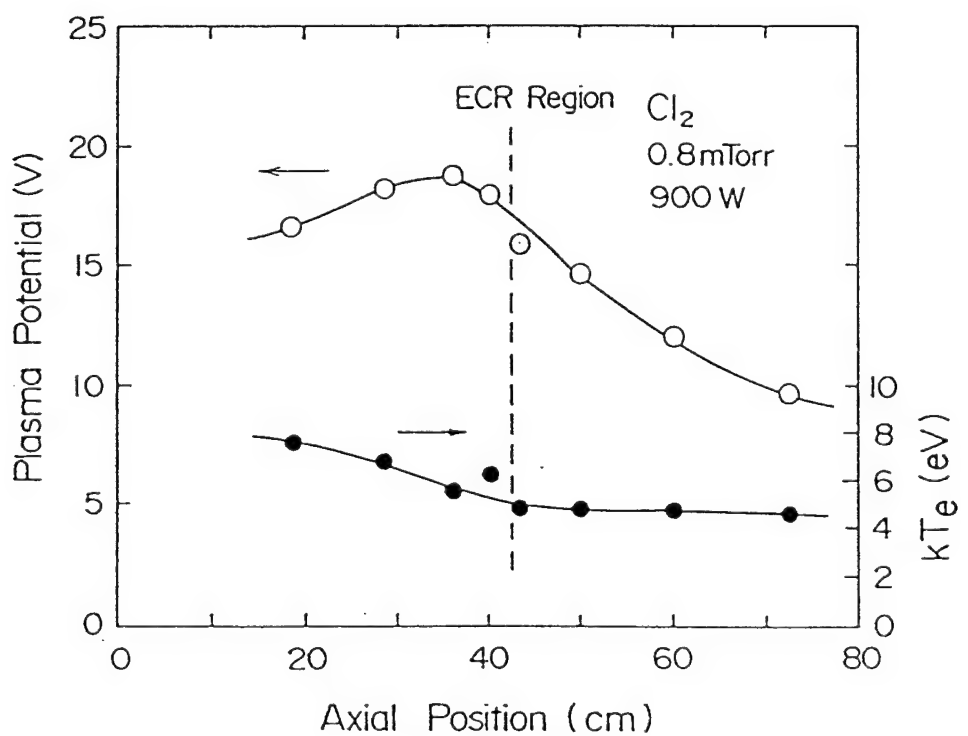
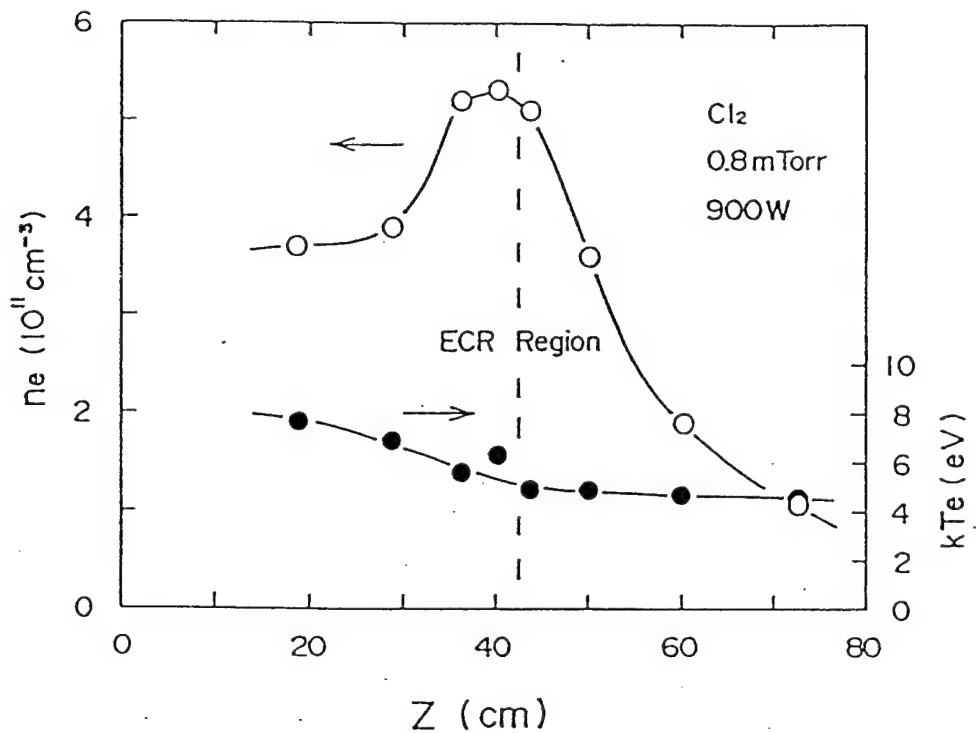


Fig. 4.3 Axial profiles of electron density, electron temperature, and plasma potential measured by K. Ono in an ECR chlorine discharge at 0.8 mTorr.

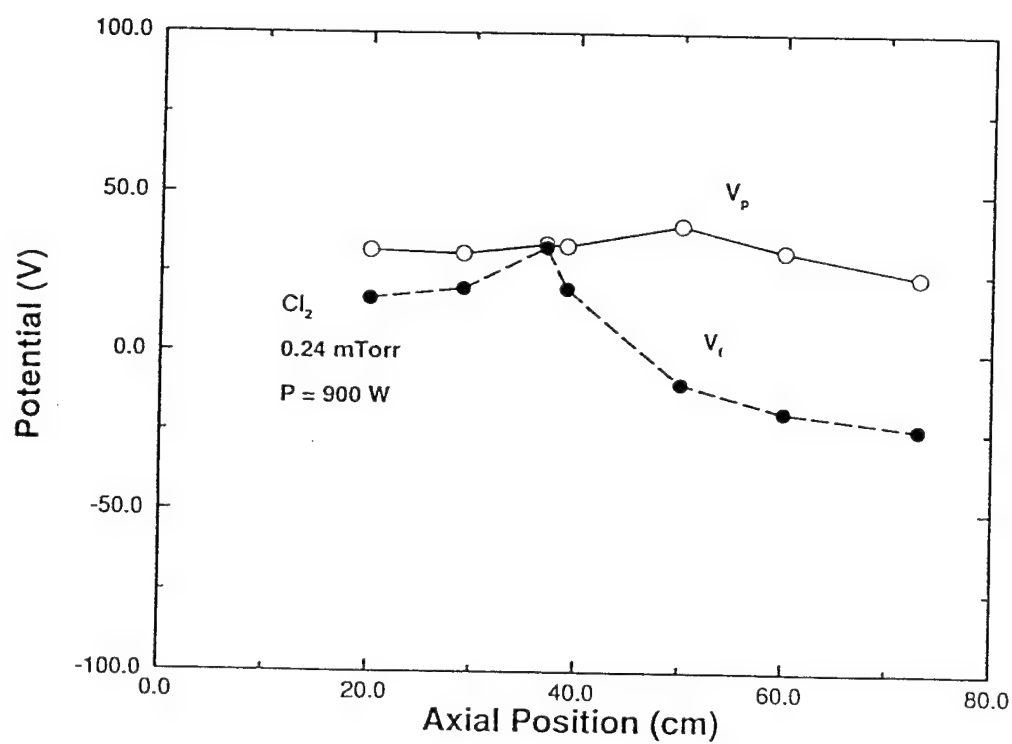
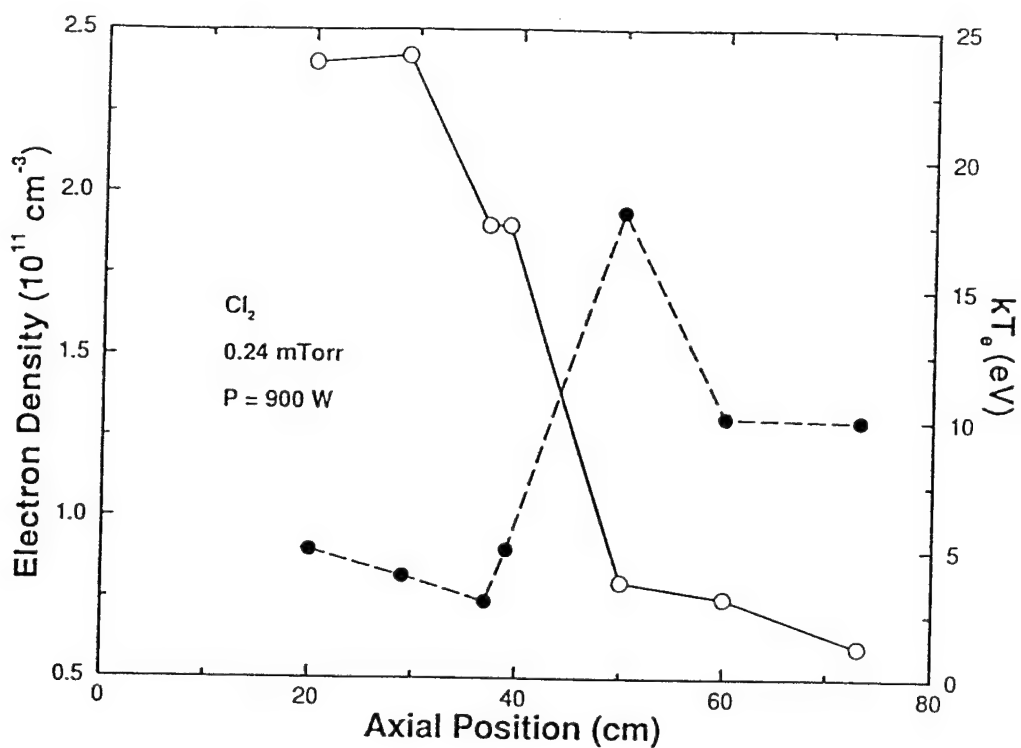


Fig. 4.4 Axial profiles of electron density, electron temperature, and plasma potential measured by K. Ono in an ECR chlorine discharge at 0.24 mTorr.

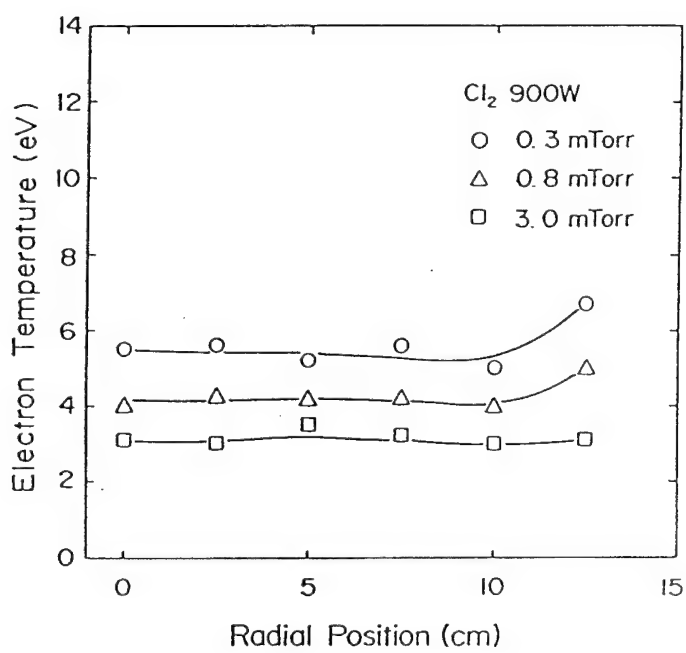
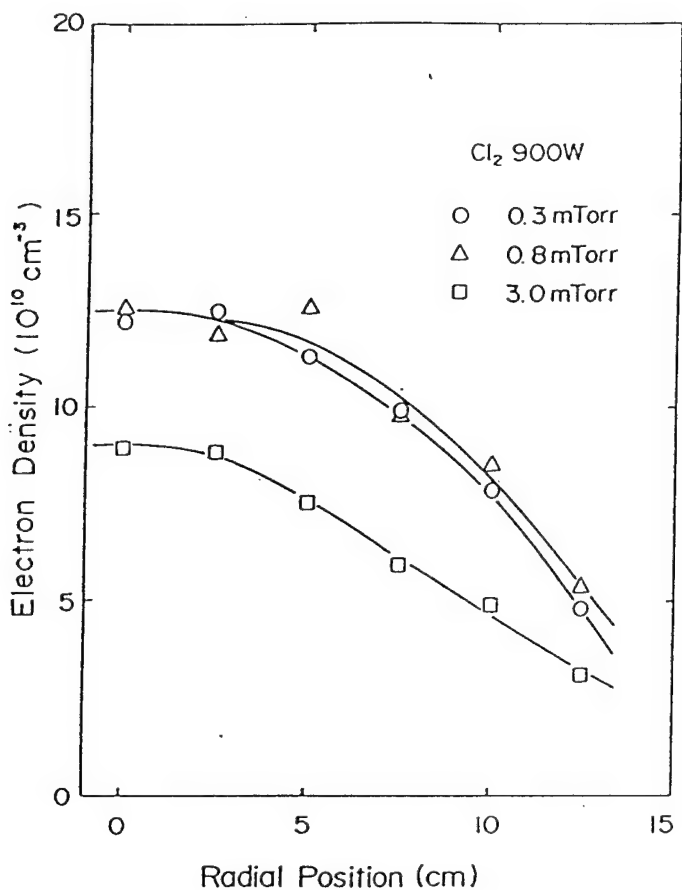
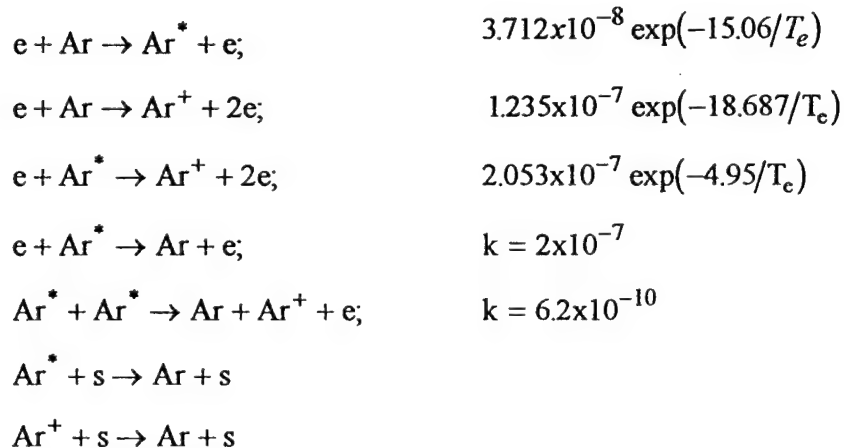


Fig. 4.5 Radial profiles of electron density and temperature in chlorine provided by K. Ono.

## 5. ECR Argon Discharge Physics: 0-d Results

In this section, we demonstrate the 0-d model for an ECR argon discharge. Mass balance for Ar,  $\text{Ar}^+$ ,  $\text{Ar}^*$ , power balance, and gas energy balance are considered. The equations are first solved for the source chamber followed by the solution for the process chamber in a cascading fashion. Volume and surface reactions and the corresponding rate coefficients given below are from ref. [26].



All rate coefficients have units of  $\text{cm}^3/\text{s}$ .  $s$  in the above reactions denotes a surface. We assume a unity sticking coefficient for both surface reactions. A constant cross-section of  $3.5 \times 10^{-15} \text{ cm}^2$  is assumed for argon-ion charge exchange. Electron elastic collision frequency is given by the relation  $\nu_e(\text{Hz}) = 1.756p/T_g$ . The ion temperature is assumed to be 0.5 eV based on the measurements of Nakano, et al. [34].

Plasma heating of the gas has been known to result in high gas temperatures of about 900°K in ECR source chambers [33, 34]. Hot neutrals and possible high surface temperatures may adversely affect surface reactions. Also, gas heating leads to a reduction in neutral density and affects plasma properties. Hence, we first validate our gas temperature predictions against experimental measurements. Figure 5.1 shows predicted gas temperatures as a function of pressure and microwave power for the experimental conditions of Hopwood and Asmussen [33]. The source chamber is 12.5 cm diameter and 15 cm long. Argon flow is 20 sccm. The uncertainty in

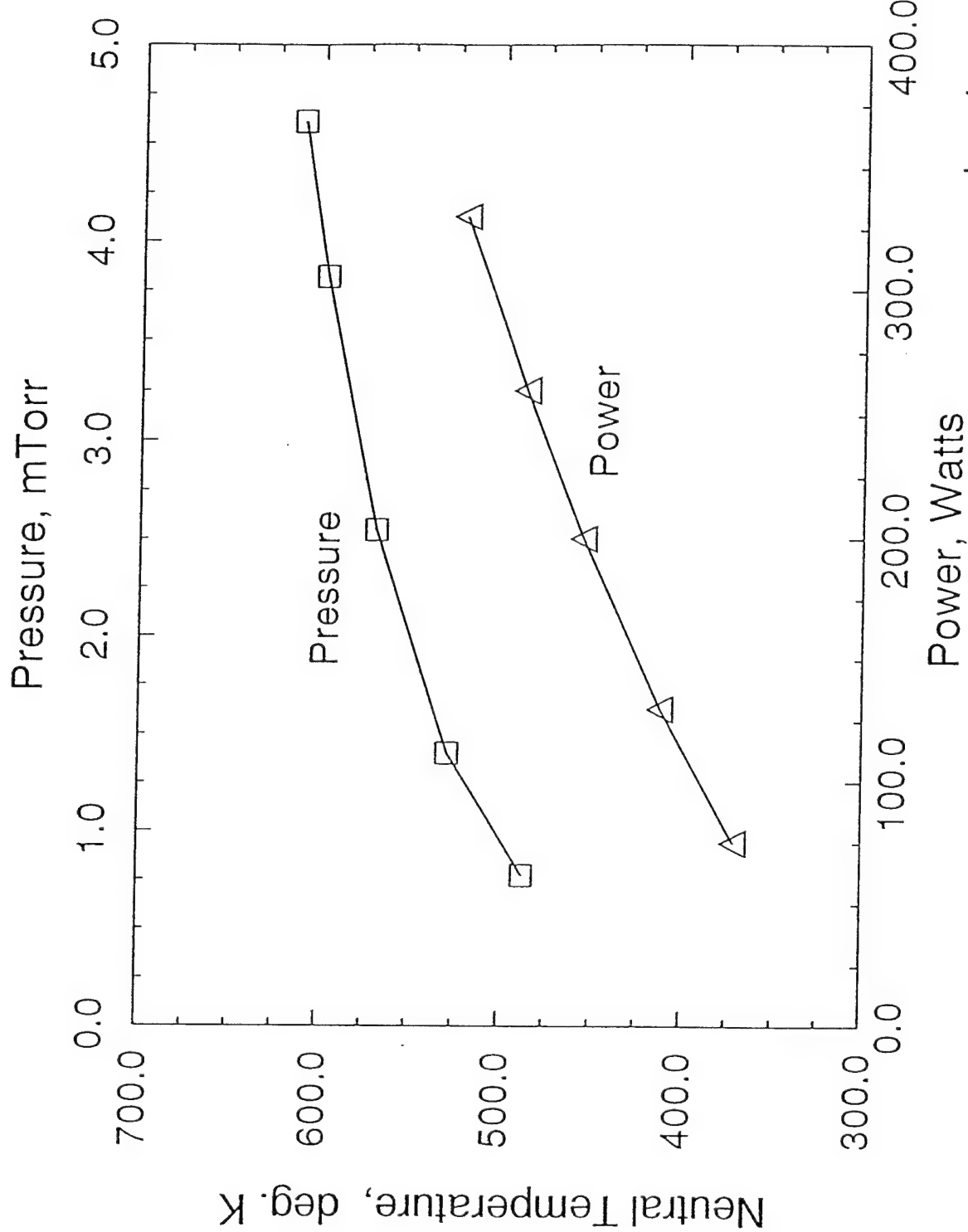


Fig. 5.1 Gas temperature in the ECR source chamber as a function of pressure and absorbed microwave power. Source diameter = 12.5 cm, length = 15 cm, argonflow = 20 sccm.

the measurements in ref. [33] is dominated by background noise and the error bars span over a 50-80° range (Figures 4 and 5 in ref. 33). The predicted temperature in each of the cases in Fig. 5.1 is well within the error bar and the comparison is good. Ion-neutral charge exchange collision is the major source of gas heating. Electron-gas elastic collisions also lead to a rise in neutral temperature although to a less extent. The ratio of heat input from charge exchange collisions to that from elastic collisions is about 7-9 for the conditions in Fig. 5.1. The resultant gas temperature is determined by the effectiveness of heat transfer to the ambient. The gas temperature increases with the absorbed microwave power. This is mainly due to an increase in plasma density with power (as will be seen later). Inspection of Eq. (41) reveals that the heating terms are proportional to plasma density. Figure 5.1 also shows that the gas temperature increases with chamber pressure. Both collision frequency and plasma density increase with pressure and lead to increased collisional heating. Gas temperatures well above that in Fig. 5.1 are obtained at higher pressures and power levels; for example, the predicted temperature is 919.5°K at  $p = 4.6$  mTorr and absorbed power of 800 Watts. In contrast, the volume-averaged gas temperature in the process chamber for conditions in Fig. 5.1 is just above room temperature. Collisional heating in the process chamber is drastically reduced due to a decrease in plasma density. The sensible heat brought into the process chamber by the gas flow is effectively dissipated to the ambient and hence, the gas temperature in the process chamber is not much above that of the ambient.

Next we discuss the plasma characteristics predicted by the model. Figure 5.2 presents the variation of electron density and temperature with pressure in the source chamber for an absorbed power of 570 watts. Figure 5.3 presents the plasma characteristics in the source chamber as a function of microwave power at a pressure of 1 mTorr. These results correspond to the Thomson scattering measurements by Bowden, et al. [35]. The source chamber dimensions are  $d = 30$  cm and  $\ell = 25$  cm. Argon flow rate is 15 sccm. To understand the discharge behavior, let us inspect Eq. (27) for  $\text{Ar}^+$  and Eq. (40) from Section 3. The  $\text{Ar}^+$  density balance requires the generation rate to be equal to the ambipolar loss rate which determines the electron temperature in the discharge. (The flow effects are negligible.) Since the particle flux to the wall depends on Bohm velocity as discussed earlier, we note from Eq. (27) that  $\sqrt{T_e} \cdot \exp(E/kT_e)$  is proportional to  $n_g L$  where  $L$  is a characteristic length. So, an increase in neutral density would result in a decrease in  $T_e$ . The plasma density is determined by the energy equation, (40), which suggests

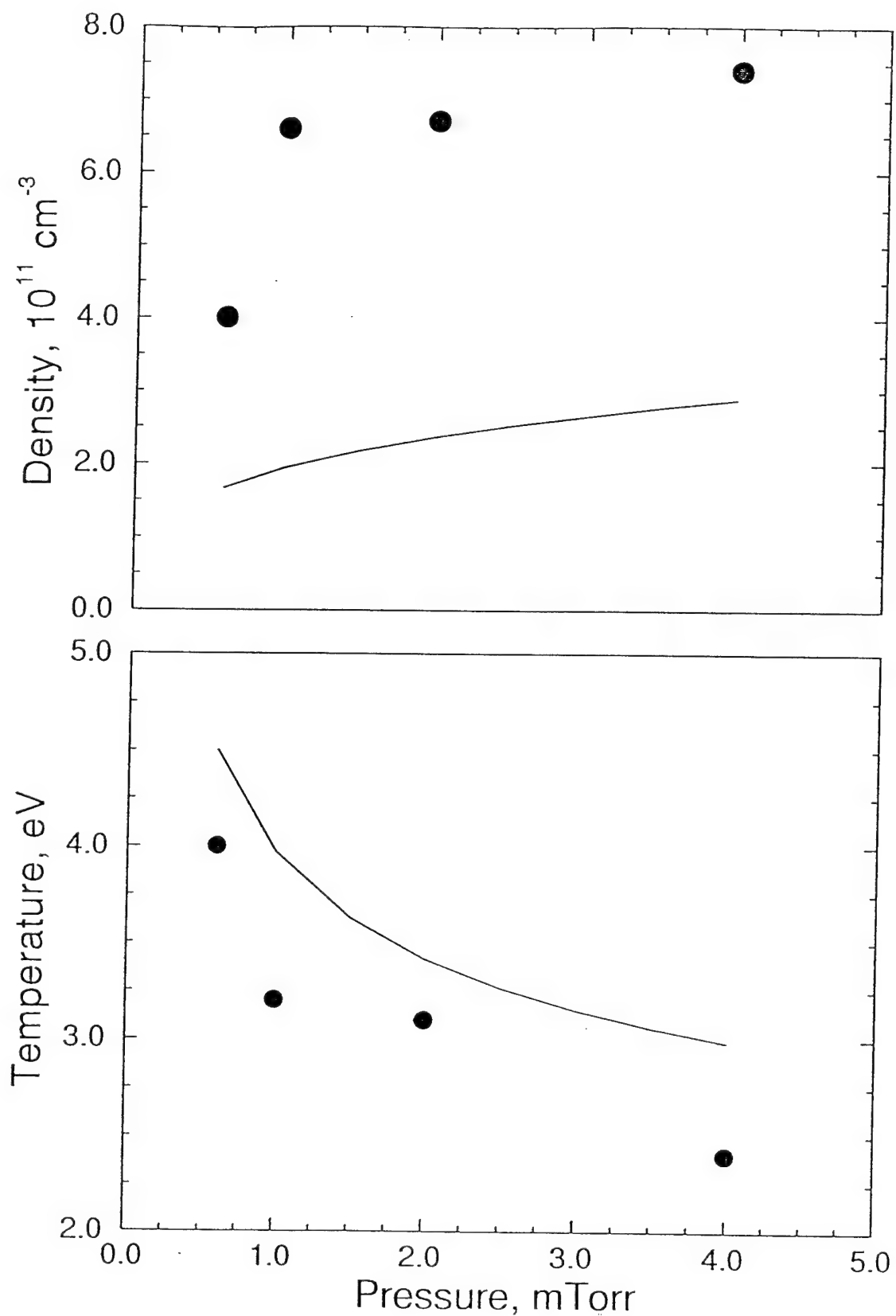


Fig. 5.2 Pressure dependence of spatially-averaged electron temperature and density (solid line). Also shown (symbols) are Thomson scattering measurements from Ref. 7, Fig. 6. The measurements correspond to a small volume on-axis and hence, are quantitatively different from reactor volume-averaged predictions.

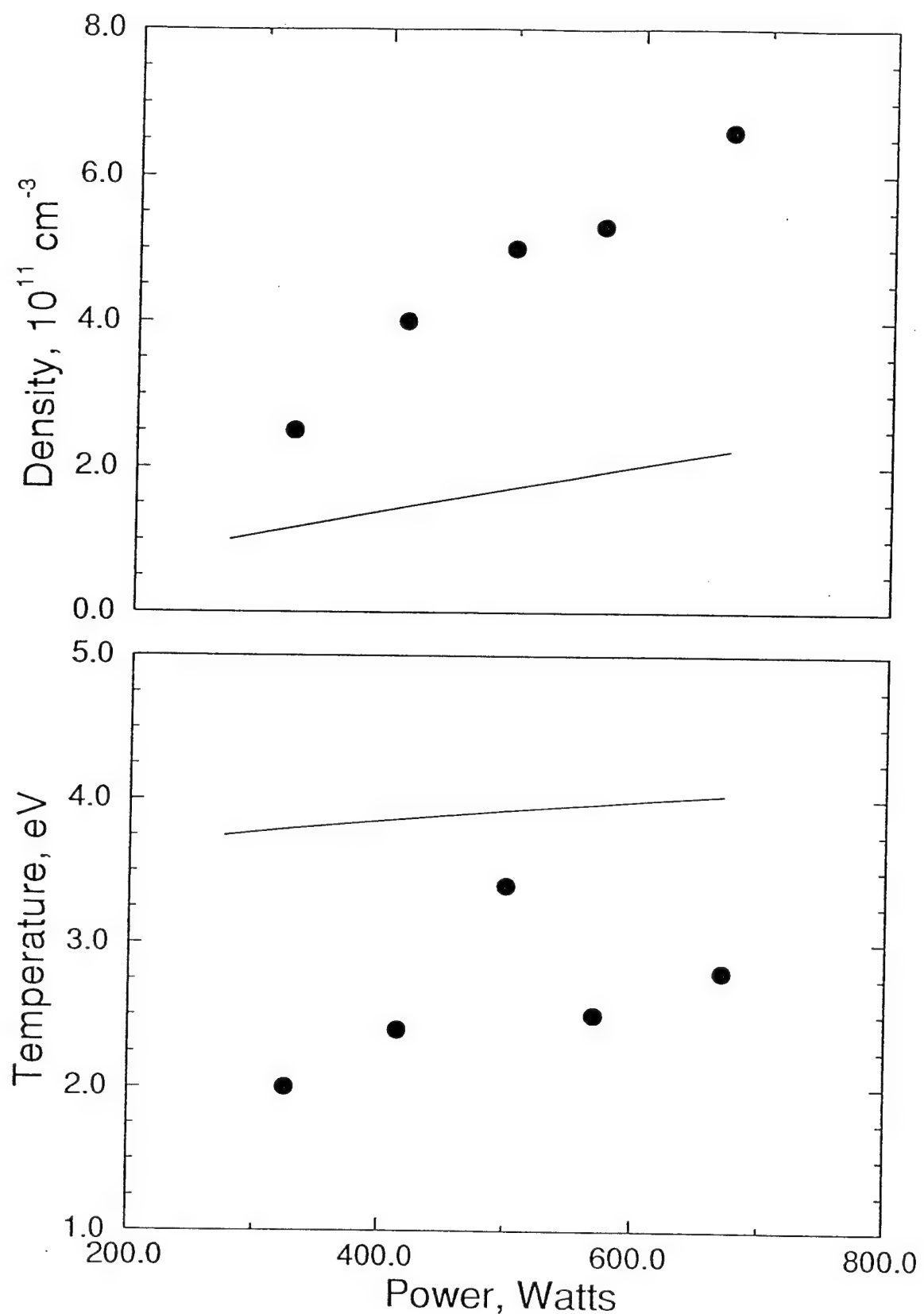


Fig. 5.3 Variation of spatially-averaged electron density and temperature with absorbed microwave power (solid line). The on-axis experimental measurements from Ref. 7, Fig. 5 are shown using symbols.

$n_+ = p_{ext}/f(T_e)$ . When the chamber pressure is increased, neutral density increases even with an increase in neutral temperature resulting in a drop of electron temperature. The plasma density increases with pressure as shown in Fig. 5.2. The variation in electron temperature with microwave power is not significant. Any variation seen in Fig. 5.3 follows changes in gas temperature and thus the neutral density. The plasma density increases with microwave power. Also shown in Figures 5.2 and 5.3 are the electron density and temperature as determined by Thomson scattering measurements from [35]. Note that the experimental measurements correspond to a small plasma volume on the axis of the source chamber and hence are quantitatively different from the volume-averaged quantities predicted here. But the qualitative behavior is mostly similar with an exception at high microwave powers. The measured density and temperature tend to saturate as power is increased, which has been attributed to the failure of microwaves to propagate in a highly dense plasma [35]. The present model is too simple to account for such phenomena. The model has also been validated by comparison against Monte-Carlo simulation results of Weng and Kushner [14]. The quantitative and qualitative agreement between the present model and the volume-averaged results of ref. 14 (Figs. 3 and 7 in ref. [14]) are good for the electron temperature dependence on pressure and microwave power. The predictions for the process chamber corresponding to the conditions in Figs. 5.2 and 5.3 reveal volume-averaged plasma densities smaller by one to two orders of magnitude and electron temperatures below 2 eV. Note that the product  $n_g L$  is higher in the process chamber than that in the source chamber which reduces the electron temperature. The ionization rate in the process chamber also is substantially reduced.

The model also allows an examination of power dissipation in ECR discharges. For a typical case of 1 mTorr and 570 Watts, the applied power is distributed as follows:

Electron-gas inelastic collision loss	= 42.3%
Electron-gas elastic collision loss	= 0.05%
Electron ambipolar wall loss	= 15.6%
Electron energy outflow	= 0.01%
Ion acceleration	= 42.0%

The above distribution essentially does not change when the power is varied from 100 to 700 Watts at 1 mTorr. However, the distribution is affected by pressure. For example, the fraction of power spent on inelastic collisions goes up from 0.35 at 0.5 mTorr to 0.52 at 5 mTorr while the fraction corresponding to ion acceleration goes down from 0.48 to 0.36. The potential difference  $\Delta\psi = V_p - V_f$  from Eq. (39) is of the order  $5.4 kT_e$  with a minor dependence on pressure.

We have used the model to examine the effect of source geometry. Figure 5.4 shows the effect of source chamber radius on the plasma characteristics for a source length of 25 cm, at 1 mTorr and 570 Watts. As the radius is increased, the characteristic length  $L$  and product  $n_g L$  increase; as discussed earlier, from Eq. (27) this requires a decrease in  $T_e$ . The volume-averaged plasma density also decreases with an increase in source chamber radius.

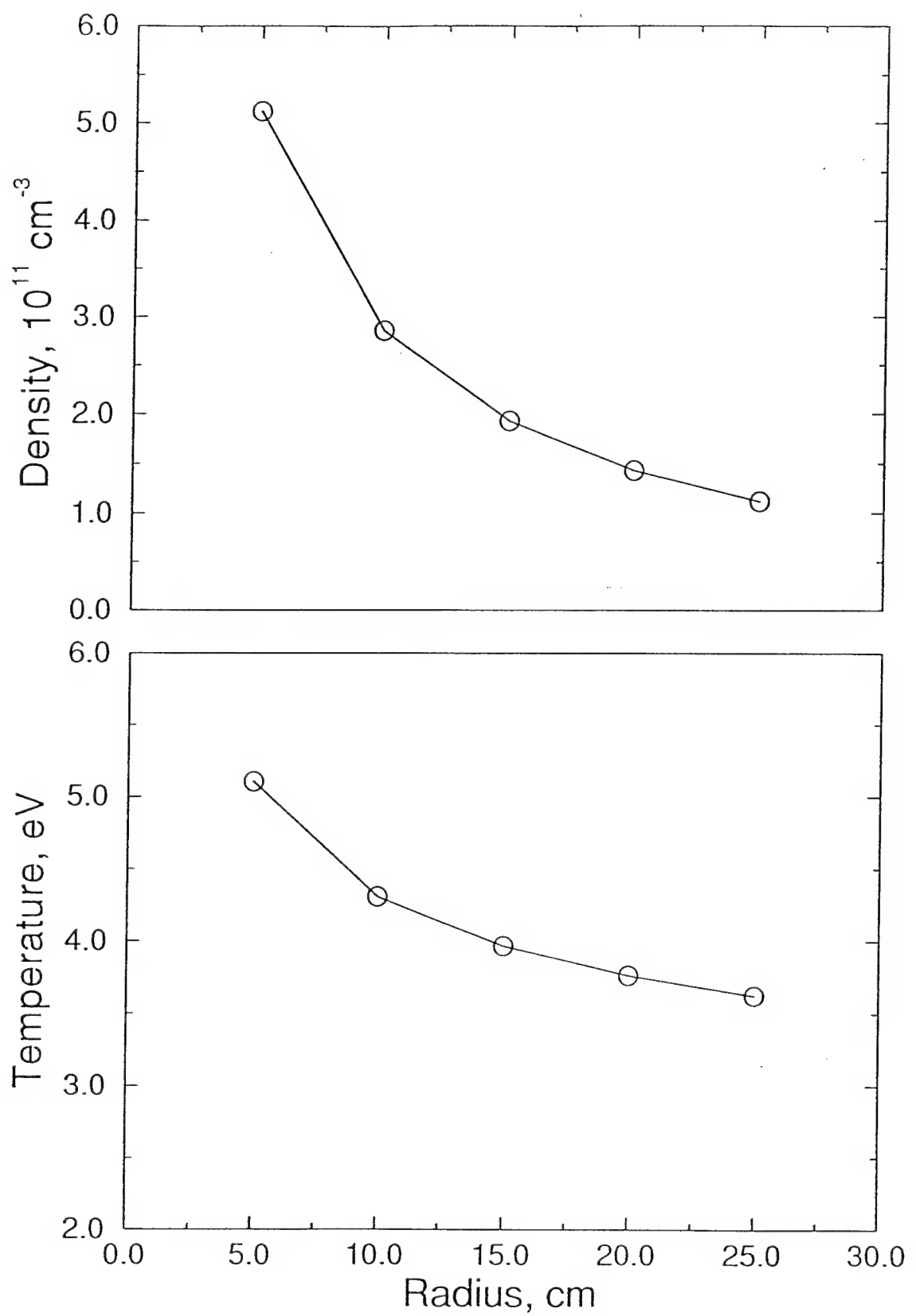


Fig. 5.4 Effect of source geometry on plasma characteristics. Source chamber length = 25 cm, pressure = 1 mTorr, absorbed power = 570 Watts and flow rate = 15 sccm.

## 6. ECR Chlorine Discharge Physics: 0-d Results

In this section, we present spatially-averaged characteristics of a chlorine discharge in an ECR reactor and illustrate the model with a parametric study of input power, pressure, flow rate and reactor dimensions. Currently there is very little experimental data on ECR or ICP chlorine discharges and available data is limited to on-axis measurements near the wafer in the process chamber[36]. Hence, we draw only a qualitative comparison with experimental observations wherever possible.

We use a collection of plasma reactions for a  $\text{Cl}_2/\text{Cl}$  mixture from ref. [37]. Bukowski [37] assumes a Maxwellian distribution in evaluating the rate constants with known cross-sections and presents them in the form,  $k = AT_e B \exp(C/kT_e)$  where  $T_e$  is electron temperature. The reactions and rate constants are listed here in Table 6.1. We include mass balance equations for  $\text{Cl}_2$ ,  $\text{Cl}$ ,  $\text{Cl}_2^+$ ,  $\text{Cl}^+$  and  $\text{Cl}^-$ . A mass balance of various excited states is not included since we do not consider two-step ionization processes and assume that the excited states rapidly return to ground level. Nevertheless, excitation processes are included in the reaction set since they affect the electron mean energy. Positive ions are assumed to readily recombine at the surface with unity sticking coefficient and liberate the corresponding neutral atom or molecule. The sticking coefficient for  $\text{Cl}^-$  is taken to be zero. The results are sensitive to the value of wall recombination coefficient for chlorine atom ( $\text{Cl} + \text{wall} \rightarrow \frac{1}{2} \text{Cl}_2$ ); we use  $v = 8.2 \times 10^{-3}$  from ref. [27]. Electron momentum transfer frequency in chlorine is computed from  $\mu n_g = 6.42 \times 10^{23} \text{ (m.v.s)}^{-1}$  where  $\mu$  is electron mobility and  $n_g$  is gas number density. Ion-neutral collision cross-section is taken to be  $1.0 \times 10^{-14} \text{ cm}^2$ .

The results presented here are for an ECR source chamber of radius,  $r = 10 \text{ cm}$  and length,  $L = 50 \text{ cm}$ . To evaluate the gas temperature in an ECR chlorine discharge using a gas energy balance, we assume an average ion temperature  $T_+$  of 0.25 eV based on the measurements in ref. [34]. Since  $\text{Cl}_2$  dissociation is nearly complete at low pressures and the resulting mole fraction of  $\text{Cl}_2$  is small, the heat gain by the gas from molecular vibrational excitation may be neglected. The gas temperature predicted here ranges from 430°K to 550°K at pressures of 0.133 - 0.67 Pa (1-5 mTorr) for an absorbed microwave power of 800 W. Since the measured ion temperature varies

**Table 6.1: Plasma Reactions**

		<u>A</u>	<u>B</u>	<u>C</u>
(1)	$\text{Cl}_2 + e > \text{Cl}_2^+ + 2e$	2.130(-8)	0.771	11.70
(2)	$\text{Cl}_2 + e > 2\text{Cl} + e$	3.990(-8)	0.115	4.43
(3)	$\text{Cl}_2 + e > \text{Cl} + \text{Cl}^-$	1.80(-10)	-	-
(4)	$\text{Cl}_2 + e > \text{Cl}^+ + \text{Cl}^- + e$	1.490(-9)	-0.272	13.20
(5)	$\text{Cl}_2 + e > \text{Cl}^+ + \text{Cl} + 2e$	3.882(-9)	-	15.50
(6)	$\text{Cl}_2 + e > \text{Cl}_2^*(B^3\pi) + e$	1.230(-7)	-1.120	4.30
(7)	$\text{Cl}_2 + e > \text{Cl}_2^*(2^1\pi) + e$	4.750(-9)	0.861	9.00
(8)	$\text{Cl}_2 + e > \text{Cl}_2^*(2^1\Sigma) + e$	4.750(-9)	0.861	9.00
(9)	$\text{Cl} + e > \text{Cl}^+ + 2e$	2.960(-8)	0.554	13.10
(10)	$\text{Cl}^- + e > \text{Cl} + 2e$	2.960(-8)	0.554	3.61
(11)	$\text{Cl} + e > \text{Cl}^*(3d) + e$	1.990(-8)	-	10.06
(12)	$\text{Cl} + e > \text{Cl}^*(4s) + e$	1.270(-8)	-	10.97
(13)	$\text{Cl} + e > \text{Cl}^*(4p) + e$	4.790(-8)	-	10.29
(14)	$\text{Cl} + e > \text{Cl}^*(4d) + 3$	9.200(-9)	-	11.15
(15)	$\text{Cl} + e > \text{Cl}^*(5p) + e$	9.320(-9)	-	11.06
(16)	$\text{Cl} + e > \text{Cl}^*(5d) + e$	5.200(-9)	-	11.12
(17)	$\text{Cl}_2^+ + \text{Cl}^- > \text{Cl}_2 + \text{Cl}$	$5 \times 10^{-8}$	-	-
(18)	$\text{Cl}_2^+ + \text{Cl}^- > 2\text{Cl}$	$5 \times 10^{-8}$	-	-

\*Rate expression is of the form:  $A(kT_e)^B \exp(-C/kT_e)$  where  $kT_e$  is electron temperature in eV,  $A$  is in  $\text{cm}^3/\text{s}$ ;  $1.0(-10)$  denotes  $1.0 \times 10^{-10}$ .

with power and pressure [34] and currently we do not have a self-consistent relation or equation for ion temperature, a constant gas temperature  $T_g = 500^\circ\text{K}$  is assumed in the remainder of the work. It is well known that the gas density in the source decreases once the plasma is ignited[38]. For example, the initial gas density at 0.133 Pa (1 mTorr) and  $500^\circ\text{K}$  is  $1.93 \times 10^{13} \text{ cm}^{-3}$ . The gas density with the plasma-on decreases to  $2.67 \times 10^{12} \text{ cm}^{-3}$  according to relation (31), which is consistent with the observations in ref. [38]. It is also clear that the use of ideal gas law with gas temperature alone (i.e. ignoring the second term in relation (31)) to compute the density would yield incorrect results, particularly at low pressures when the electron partial pressure is significant and the ratio  $T_e/T_g$  is very high. The reduction in density is only about 7% at 1.33 Pa.

The effect of pressure on ECR chlorine discharge characteristics is shown in Figs. 6.1 and 6.2. The electron temperature decreases as the gas pressure is increased. This is similar to the observations by Ono, et al.[36] although their on-axis measurements are for the process chamber. This variation of electron temperature with pressure in an ECR chlorine discharge is similar to that found in rf capacitively-coupled, as well as ECR argon discharges. In electropositive discharges, ionization is balanced by ambipolar diffusion to the wall. The latter decreases as the pressure increases and therefore electron temperature must decrease to reduce the ionization rate constant. As will be seen later, the ECR chlorine discharge at low pressures and high power levels is highly electropositive and the attachment rates are significantly lower than ionization rates. Note that the electron temperature in Fig. 6.1 is the spatially-averaged quantity; values on the axis may be considerably higher. Though ionization rate constants decrease with decreasing electron temperature, electron density (Fig. 6.2a) increases with pressure due to the increase in neutral gas density. Such an increase in electron density at low pressures has been reported by Nakano, et al.[34] for ECR chlorine plasmas. Indeed, all ion densities increase with pressure. The electron density is nearly balanced by the  $\text{Cl}^+$  density. The degree of dissociation is high in the range of pressure, power and flow rates investigated here which rapidly increases with pressure at first and then decreases slowly (Fig. 6.2b). Consistently,  $\text{Cl}^+$  is the most abundant positive ion. As seen in Fig. 6.2b, electron is the most dominant negative charge carrier. Even at a pressure of 2 Pa, the ratio of  $[\text{e}]/[\text{Cl}]$  is about 34, indicating the electropositive nature of the discharge. The rates of reactions 3 and 4 in Table 6.1, which produce the negative ions, are rather low due to low  $\text{Cl}_2$  mole fractions.

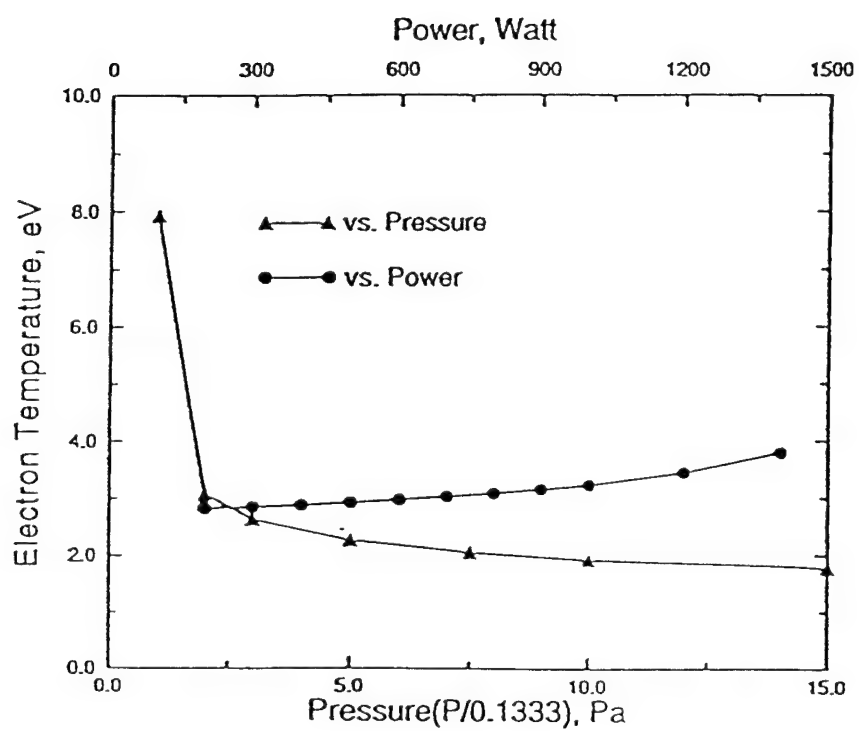


Fig. 6.1 Spatially-averaged electron temperature in an ECR source chamber (radius = 0.1 m, length = 0.5 m) at a  $\text{Cl}_2$  flow rate of 10 sccm. Variation with pressure is shown at 800 W power. The temperature vs power profile is for a pressure of 0.266 Pa.

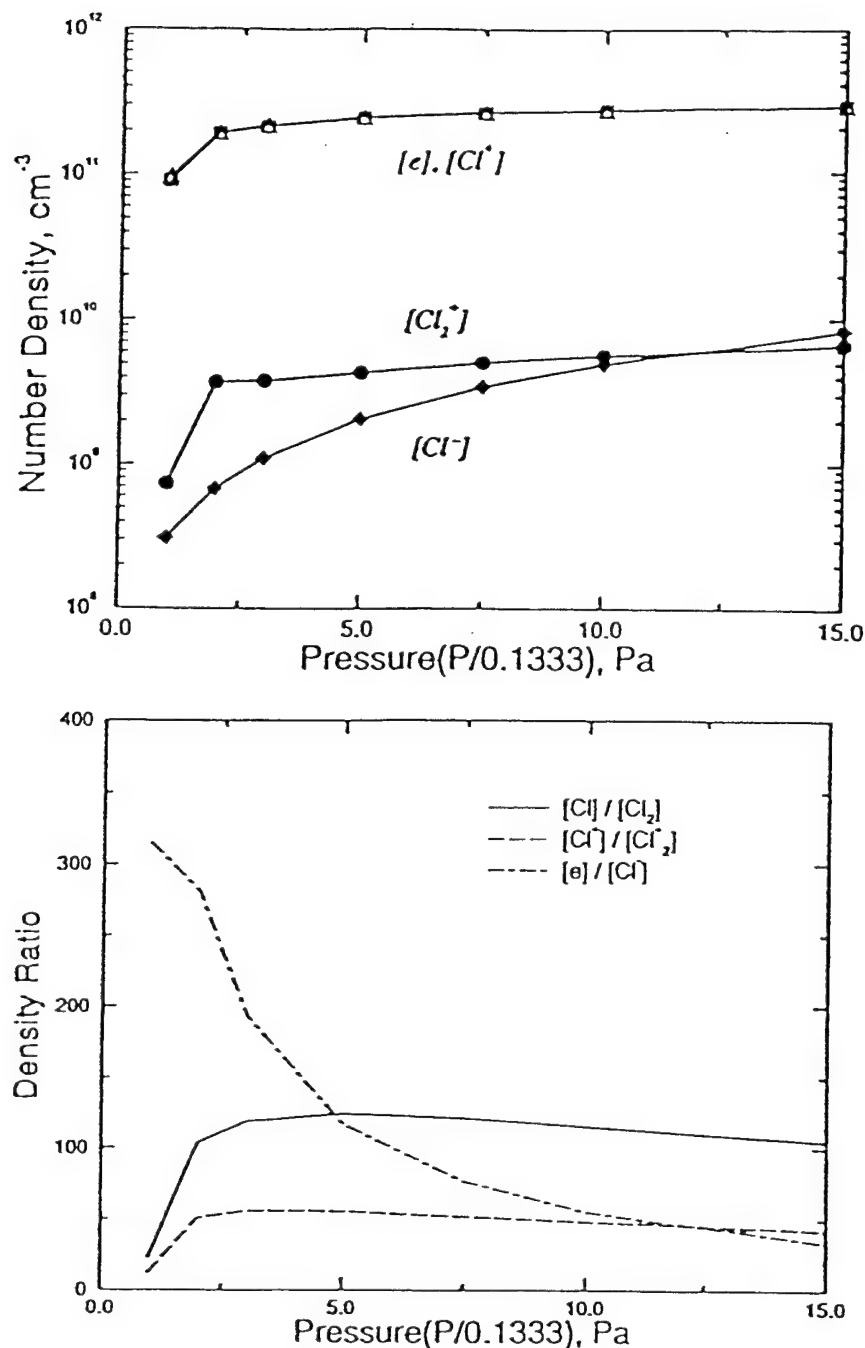


Fig. 6.2 Effect of pressure on ECR chlorine discharge characteristics:  
 $\text{Cl}_2$  flow rate = 10 sccm; absorbed microwave power = 800 W.  
 (a) density profiles and (b) degrees of dissociation  $[\text{Cl}] / [\text{Cl}_2]$ ,  
 ion ratio  $[\text{Cl}^+] / [\text{Cl}_2^+]$  and degree of electronegativity  $[\text{e}] / [\text{Cl}^-]$ .

The variation of plasma potential with pressure, according to Eq. (39), is from  $5.5kT_e$  ( $=40.5$  V) at  $0.133$  Pa (1 mTorr) to  $6.5kT_e$  ( $=11.5$  V) at  $2$  Pa (15 mTorr). Table 6.2 presents an account of how the applied power is spent as a function of pressure. Energy spent on electron inelastic collisions is a dominant mechanism which increases with pressure. Of the reactions shown in Table 6.1, energy loss due to Cl atom excitation processes is more significant than others. The fraction of the total power spent on accelerating the ions is high at low pressures but declines progressively as pressure increases.

**Table 6.2**

Account of how the applied power is spent in an ECR chlorine discharge:  
 absorbed microwave power = 800W; Cl<sub>2</sub> flow rate = 10 sccm.  
 Fraction of total power is shown.

Process	Pressure, Pa			
	0.133	0.267	0.667	1.333
Inelastic collision	0.3544	0.7153	0.8299	0.8791
Electron elastic collision	0.0001	0.0009	0.0027	0.0055
Electron energy outflow	0.0007	0.0001	0.0000	0.0000
Ambipolar wall loss	0.1725	0.0738	0.0417	0.0278
Ion power deposition	0.4723	0.2100	0.1256	0.0876

Next we discuss the effect of absorbed microwave power on the plasma characteristics using case studies conducted at  $0.267$  Pa (2 mTorr) and a Cl<sub>2</sub> flow rate of 10 sccm. Due to increasing partial pressure of electrons and large  $T_e/T_g$  ratios, the gas density decreases linearly with an increase in power according to relation (31). The balance of ionization vs. ambipolar diffusion discussed earlier for electropositive discharges effectively requires  $\sqrt{T_e} \cdot \exp(E/kT_e)$  to be proportional to  $n_g L_c$ , where  $L_c$  is a characteristic length; this condition indeed can be obtained from Eq. (27) for positive ions when the flow terms are neglected. The reduction in  $n_g$  when power is increased results in some increase in electron temperature (Fig. 6.1). The effect of power on

**Table 6.3**

Account of how the applied power is spent in an ECR chlorine discharge:  
 pressure = 0.267 Pa;  $\text{Cl}_2$  flow rate = 10 sccm.  
 Fraction of total power is shown.

Process	Power, kW			
	0.200	0.500	1.000	1.400
Inelastic collision	0.7555	0.7379	0.6956	0.6283
Electron elastic collision	0.0011	0.0010	0.0008	0.0005
Electron energy outflow	0.0007	0.0001	0.0001	0.0001
Ambipolar wall loss	0.0630	0.0675	0.0792	0.0979
Ion power deposition	0.1803	0.1935	0.2244	0.2733

plasma density is shown in Fig. 6.3a and various density ratios are plotted in Fig. 6.3b as a function of power. Electron density increases with power and is nearly balanced by  $\text{Cl}^+$  density; the difference between the two cannot be seen within the scale of Fig. 6.3a. The reduction in  $\text{Cl}^-$  density is due to continuously decreasing mole fraction of  $\text{Cl}_2$  with an increase in power. The degree of dissociation, ratio of molecular ion to atomic ion density, and  $[\text{e}]/[\text{Cl}^-]$  increase with power as shown in Fig. 6.3b. The plasma potential shows little variation around  $5.7 \text{ kT}_e$  in the range of 200-1400 W. The applied power distribution pattern also shows only small variations with power (Table 6.3).

The effect of flow rate is displayed in Figs. 6.4a and b. Unlike pressure and microwave power, the feed gas flow rate has negligible effect on electron density and temperature. However, the dissociation of molecular chlorine decreases significantly with a reduction in residence time. As a result  $\text{Cl}_2^+$  and  $\text{Cl}^-$  ions are relatively more abundant at high flow rates.

The reactor dimensions play a critical role in determining the plasma characteristics [39]. In general, it is believed that high plasma densities can be generated in relatively small source

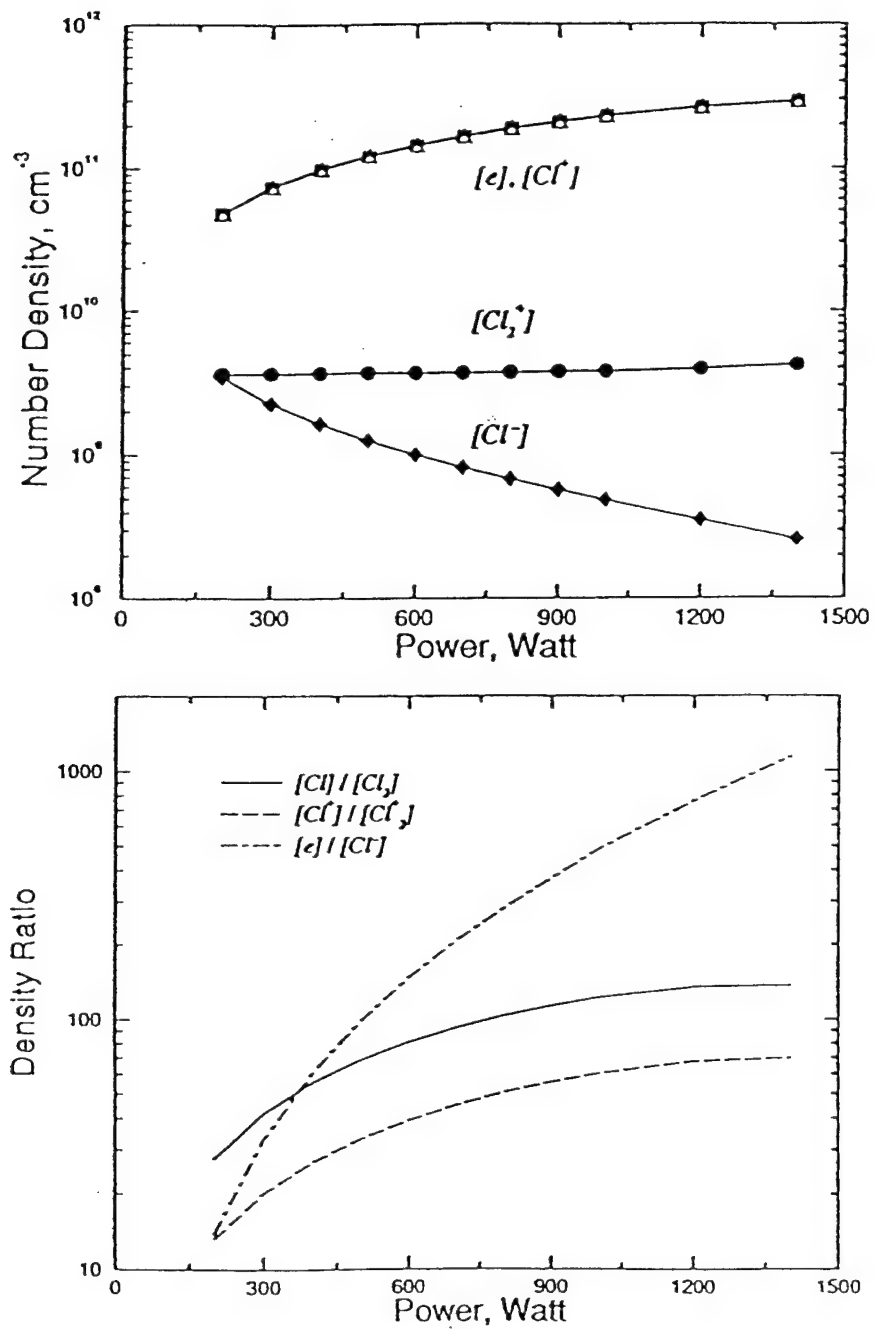


Fig. 6.3 Effect of absorbed microwave power on ECR chlorine discharge characteristics:  $Cl_2$  flow rate = 10 sccm; pressure = 0.267 Pa.  
 (a) density profiles and (b) degree of dissociation  $[Cl]/[Cl_2]$ , ion ratio  $[Cl^+]/[Cl_2^+]$ , and degree of electronegativity,  $[e]/[Cl^-]$ .

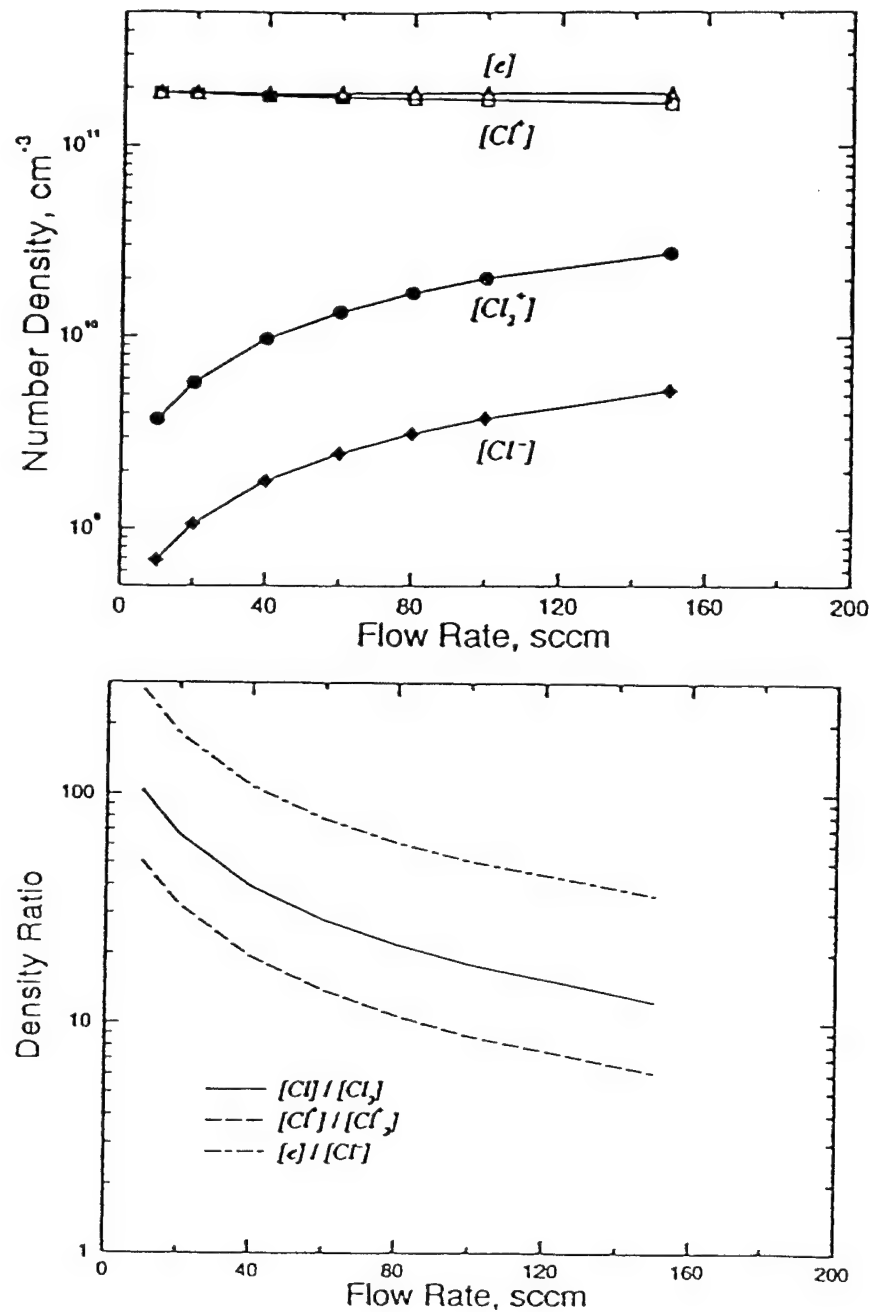


Fig. 6.4 Effect of  $\text{Cl}_2$  flow rate: Pressure = 0.267 Pa, absorbed power = 800 W, radius = 0.1 m and length = 0.5 m. (a) density profiles and (b) degree of dissociation  $[\text{Cl}] / [\text{Cl}_2]$ , ion ratio  $[\text{Cl}^+] / [\text{Cl}_2^+]$  and degree of electronegativity  $[e] / [\text{Cl}_2^-]$ .

chambers. Variation of plasma parameters as a function of source radius from the present model is shown in Fig. 6.5, which is qualitatively similar to the data for ECR nitrogen discharges from Popov[39]. The electron density exhibits a peak at some radius. However, a more relevant quantity electron density per absorbed power density ( $[e]/\text{Power}/\pi r^2$ ) suggested by Popov[39] as a measure of source efficiency, continues to grow with radius and shows no sign of saturation even at 20 cm. The electron temperature and plasma potential (which is approximately  $5.7 \text{ kT}_e$ ) show a decrease with an increase in source radius. The qualitative behavior of electron density and temperature is similar to that in Fig. 6.5 when the source length is varied, keeping the radius constant at 10 cm.

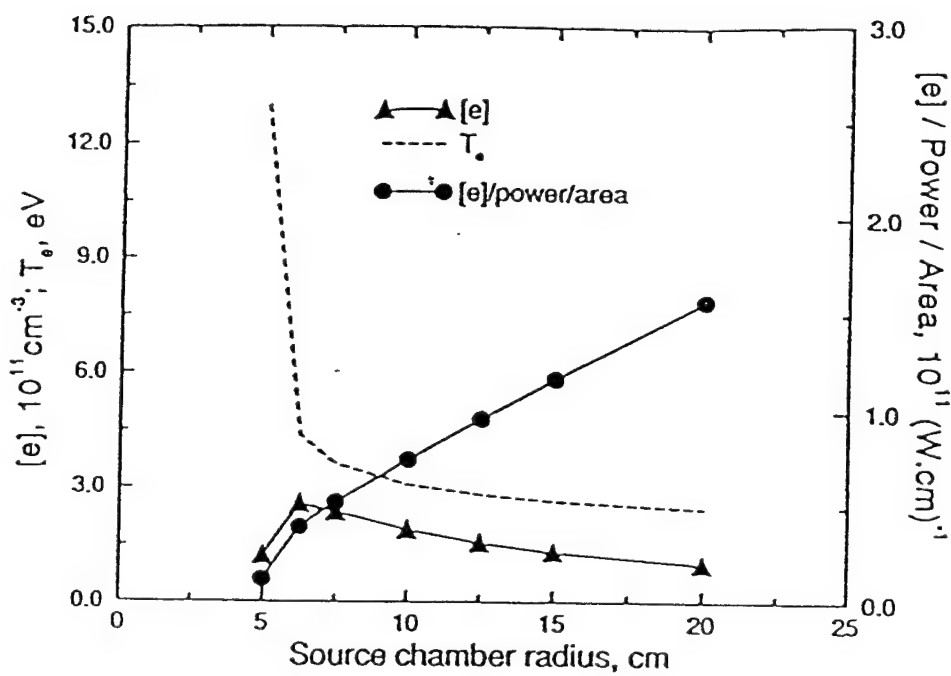


Fig. 6.5 Effect of source chamber radius on electron density  $n_e$ , electron temperature  $T_e$ , and electron density per power density,  $n_e/(\text{power}/\pi r^2)$ : Power = 800 W, pressure = 0.267 Pa,  $\text{Cl}_2$  flow rate = 80 sccm and source length = 0.5 m.

## 7. ECR Argon Discharge Physics: 1-d Results

In this section, we present results from the radially-averaged one-dimensional model for an ECR reactor. We consider a cylindrical source chamber of 14 cm diameter and 40 cm length, and a cylindrical process chamber of 60 cm diameter and 40 cm length. This system is the same as that simulated by Porteous, et al.[15] in a discharge physics study; it is also similar to that used for ECR diagnostics by Gorbatkin, et al.[40], except that the downstream chamber diameter in ref. [40] is 25.4 cm. We assume that the change in diameter from the source to the process chamber occurs gradually over a 10 cm length starting from  $z = 40$  cm. As mentioned earlier, we do not currently solve for microwave power absorption self-consistently; instead, we use a magnetic field profile reported in ECR argon experiments and the corresponding power profile suggested by Porteous, et al[15]. In the axial direction this power profile has a sharp peak at the ECR resonance zone ( $z = 16$  cm where Gorbatkin, et al.[40] made probe measurements), and the total power distributed over the resonance zone is 500 W[15]. We report results at various pressures and flow rates of argon for an applied power of 500 W and compare against measurements from ref. [40].

The set of inelastic collision processes and other reactions for argon are the same as those described in Section 5. The ion temperature is assumed to be 0.5 and 0.25 eV in the source and process chambers respectively, based on the measurements of Nakano, et al.[34]. These values are used only to compute the gas heating term due to charge exchange collisions in the gas energy equation.

Gorbatkin, et al.[40] reported that with no microwave power and in the absence of plasma, the pressure downstream (measured at  $Z = 60$  cm or  $Z/L = 0.75$ ) is about 75-90% of that measured near the resonance zone ( $Z = 16$  cm or  $Z/L = 0.2$ ). Figure 7.1 shows a comparison of model results and pressure measurements in the absence of plasma. We point out that Gorbatkin et al. allowed the downstream butterfly valve to remain in the open position for these measurements and adjusted the argon flow rate to obtain the desired pressure. For this reason, the results in Fig. 7.1 are shown as a function of flow rate. We have observed negligible pressure drop between  $Z = 60$  cm and  $Z = 80$  cm in all our simulations, with or without plasma. Therefore, we used the measured downstream pressure as our boundary condition at  $Z/L = 1.0$ . The agreement between predicted and measured pressure upstream is excellent, as seen in Fig. 7.1. At 5 sccm, the downstream

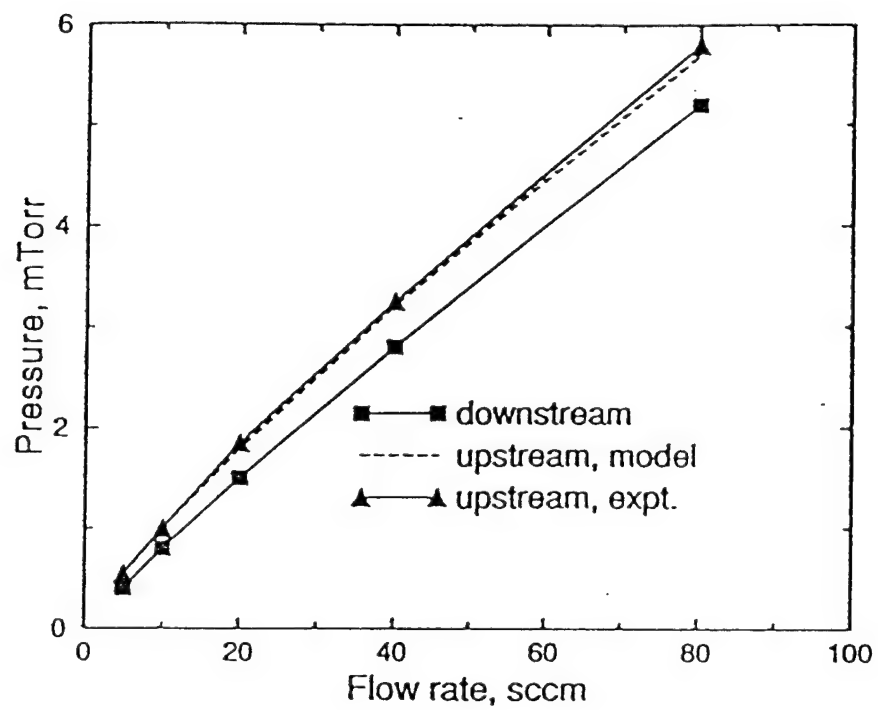


Fig. 7.1 Comparison of predicted and measured (from Ref. 40) pressures in the source chamber (upstream) with no microwave power and in the absence of plasma. The measured downstream pressure was used as an exit boundary condition in the model.

pressure is about 75% of the pressure near the resonance zone and increases to 90% at 80 sccm. A large expansion in cross-sectional area is normally accompanied by a decrease in velocity and increase in pressure in subsonic flows. We notice a decrease in mass-averaged velocity beyond  $Z/L = 0.5$  in all simulations. But the observed pressure profile is mainly influenced by the viscous losses in the source region ( $Z/L < 0.5$ ) and there is a significant pressure drop from the inlet to the edge of the source chamber. Indeed, there is a pressure minimum between the inlet and downstream probe location though the minimum pressure is closer to the downstream value. In contrast, the neutral pressure at the resonance region is smaller than at the downstream location with the application of microwave power and plasma formation, as will be seen below.

In the remainder of this section, we discuss the effects of pressure and flow rate on the axial profiles of various plasma parameters. Simulations were performed at various pressures (in the range of 1 - 8 mTorr) and flow rates (5 - 80 sccm) for an applied microwave power of 500 W. Figure 7.2 shows axial profiles of plasma density, electron temperature, electron and neutral pressures, neutral temperature, neutral density, and ionization rate and compares results at 2 and 8 mTorr for an argon flow rate of 20 sccm. The abscissa in all figures corresponds to normalized distance  $Z/L$ , where  $L$  is the total reactor length of 80 cm.  $Z/L = 0.5$  corresponds to the end of source chamber. The electron density peaks at or near the resonance region, as shown in Fig. 7.2a and as seen in experiments [41]. The exception to this occurs at low pressures and low flow rates, as will be discussed later. Note that by virtue of the quasi-neutral plasma assumption, Fig. 7.2a also denotes ion density. The axial plasma density profile is qualitatively similar to that measured by Carl, et al.[41], and Iizuko and Sato[42]. We note that the plasma density in the source can be higher than that in the process chamber by an order of magnitude. While an increase in pressure results in an increase in plasma density in the source, a decrease is seen in the process chamber. This is due to decreased electron temperature (Fig. 7.2b) and thus decreased ionization rate (Fig. 7.2f) downstream when pressure is increased. The electron temperature also peaks at or near the resonance zone. Though power is deposited over a narrow ECR zone, the large electron thermal conductivity transports electron energy efficiently downstream. Indeed, at pressures below 2 mTorr, the persistently high electron temperature downstream causes significant ionization in the process chamber. The electron temperature decreases with an increase in pressure and this inverse relation is a well-known scaling law obtained from 0-d models, as discussed in previous sections.

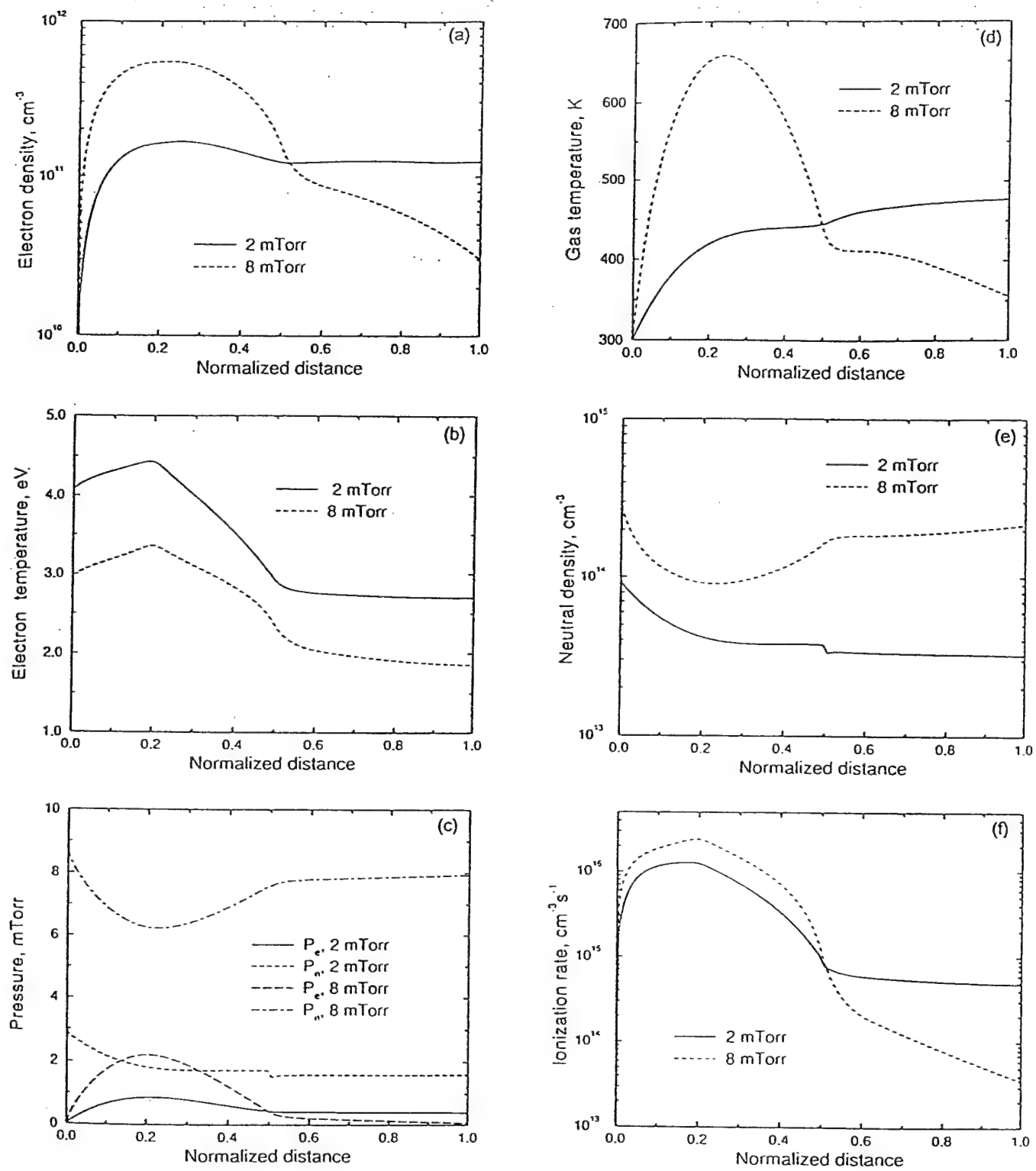


Fig. 7.2 Axial profiles of various parameters at 500 W and 20 sccm argon flow: (a) plasma density, (b) electron temperature, (c) neutral ( $P_n$ ) and electron ( $P_e$ ) pressures, (d) neutral temperature, (e) neutral density, and (f) ionization rate. The normalized distance,  $Z/L=0.5$  corresponds to the end of source chamber.

The axial electron temperature profile shown in Fig. 7.2b is qualitatively similar to that by Weng and Kushner[14], who used a Monte Carlo procedure to compute the EEDF and energy characteristics. Two-dimensional discharge physics studies[15] show that the radial profiles of both electron density and temperature exhibit an on-axis peak which is expected due to wall recombination of electrons and ions. The results obtained in this work are radially-averaged and thus would be smaller than on-axis values.

Figure 7.2c shows profiles of electron and neutral pressures,  $P_e$  and  $P_n$  respectively, in the reactor. In the transport part of the modeling, since we assume  $T_{ion} = T$ , the neutral pressure here is given by  $nkT$ , where  $n$  is the sum of number densities of argon, metastables, and  $Ar^+$ . In general, the contribution of the middle term in the thermodynamic pressure relation (31) due to ions is small. The total pressure is not shown in Fig. 7.2c for the sake of clarity, but can be obtained by adding the curves for electron and neutral pressures. The total pressure at the inlet is higher than that imposed at the exit as boundary condition. The fractional increase is higher at low pressures. This behavior is consistent with that in Fig. 7.1 in the absence of plasma. With plasma formation, the neutral pressure in the ECR region drops significantly, relative to the inlet. This is essentially due to intense local ionization, as evidenced by an increase in electron partial pressure in the same region. For example,  $P_e/P_n$  at the ECR zone is approximately 30 - 40% for both 2 and 8 mTorr cases shown in Fig. 7.2c. Note that the electron partial pressure profile tracks electron density and the distortion in its shape is due to electron temperature. Then it is not surprising that most of the neutral pressure drop that occurred in the source is recovered in the process chamber. The results in Fig. 7.3c are qualitatively and quantitatively in agreement with observations by Gorbatkin, et al.[40], who measured neutral pressure at  $Z/L = 0.2$  and  $0.75$ . The neutral temperature profile is shown in Fig. 7.2d. The gas heating is mainly due to ion-neutral collisions with a minor contribution from electron-neutral elastic collision, as discussed in the previous sections, using a 0-d model. The axial variation in temperature then follows the plasma density. The heat transfer from the gas to the wall may not be effective at low pressures, since inside heat transfer coefficient  $h_i$  is proportional to gas density. This may be the reason for the slight increase in temperature with distance inside the process chamber at 2 mTorr. No temperature measurements are available in ref. [40] for comparison. However, we point out that the volume-averaged temperature in the source computed from a 0-d model (Section 5) for the present conditions compares well with the results in

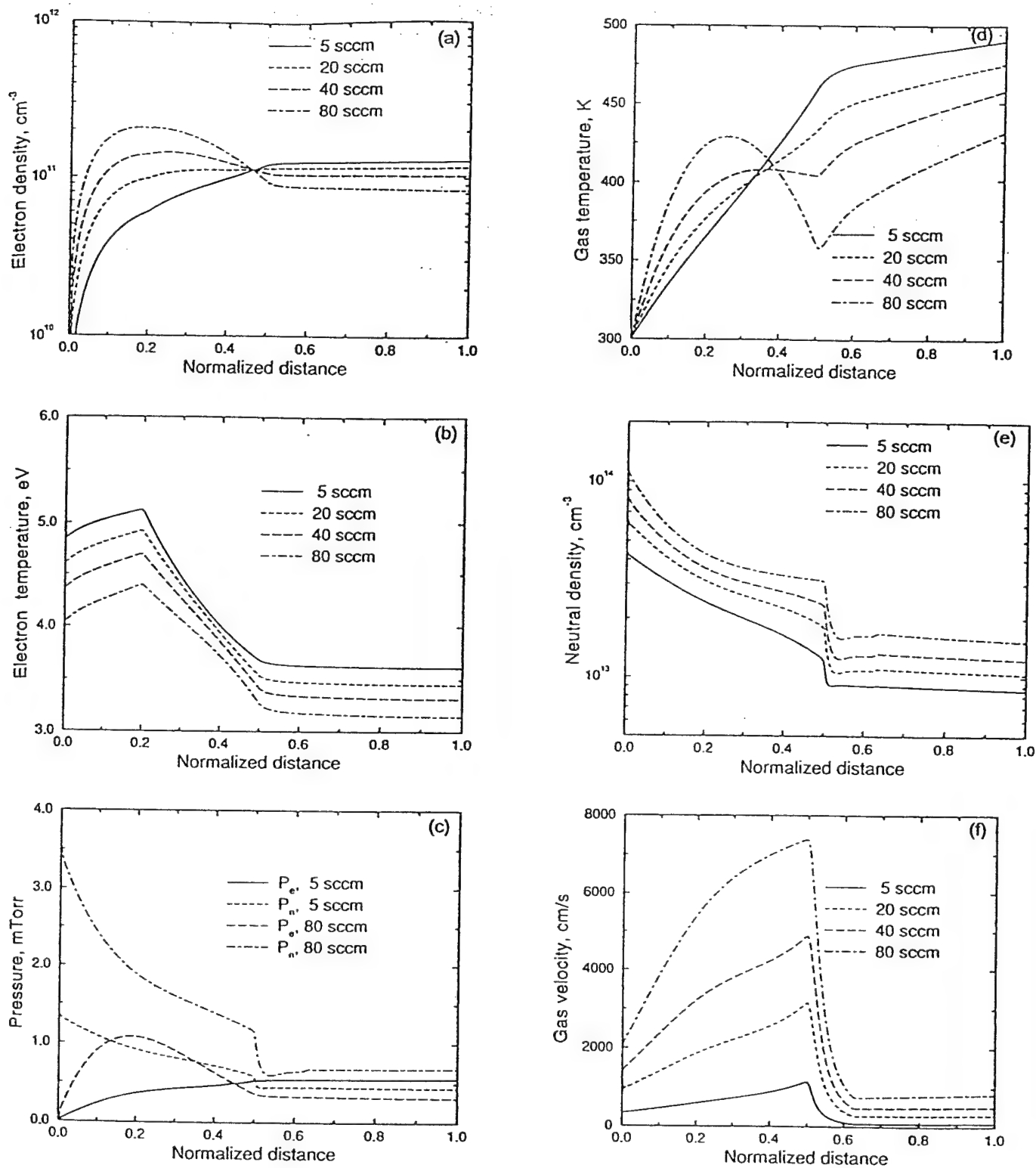


Fig. 7.3 The effect of argon flow rate on the axial profiles of various parameters: (a) plasma density, (b) electron temperature, (c) neutral ( $P_n$ ) and electron ( $P_e$ ) pressures, (d) neutral temperature, (e) neutral density, and (f) mass-averaged velocity. Reactor conditions: Power=500 W and  $p=1$  mTorr. The normalized distance,  $Z/L=0.5$  corresponds to the end of source chamber.

Fig. 7.2d. Note that the 0-d model uses the same physical features as in the 1-d equations and using the 0-d model, we have previously shown in Section 5 gas temperatures in agreement with the measurements by Hopwood and Asmussen[33]. The neutral density profile shown in Fig. 7.2e is consistent with the variation in neutral pressure and temperature in the reactor. Rossnagel, et al.[43] observed a similar reduction in neutral density in the ECR region relative to the sample region and attributed such behavior to gas heating.

Next, we discuss the effect of flow rate on the variation of plasma parameters. Figure 7.3 shows axial profiles of plasma density, electron temperature, neutral and electron pressures, gas temperature, neutral density, and mass-averaged velocity for four different argon flow rates at 1 mTorr and 500 W. The electron density profile at high flow rates looks similar to those in Fig. 7.2a. However, at 1 mTorr and low flow rates (for example, 5 sccm), the peak in plasma density does not occur at the ECR zone. Instead, the density continues to increase into the process chamber, where the electron temperature is high (Fig. 7.3b). Though the electron temperature is higher at lower flow rates, the decrease in neutral density with flow rate (Fig. 7.3c) in the source region causes a corresponding decrease in ionization. This explains the decrease in electron density with decreased flow rate in the source, which is consistent with the observations by Rossnagel, et al[43]. Figure 7.3c shows the neutral and electron pressure profiles as a function of flow rate. The neutral pressure increases everywhere as flow rate is increased. Notice that the total pressure at the inlet (which is all neutral) at 80 sccm is about 3.5 mTorr, while the total pressure at the downstream valve is 1 mTorr. Also, at 1 mTorr, the electron pressure is a substantial fraction of the total pressure in the ECR region, as well as in the process chamber. The gas temperature profile for various flow rates in Fig. 7.3d follows the corresponding plasma density variations in the reactor. The gas temperature in the process chamber decreases when the mass flow rate is increased. The increase in gas density in the ECR region with flow rate at 1 mTorr is similar to the measurements by Rossnagel, et al.[43]. Figure 7.3f shows profiles of mass-averaged velocity in the reactor. The increase in velocity in the source region is concomitant with a drop in pressure. The velocities in the process chamber are smaller due to the enlarged cross-sectional area.

Finally, in Fig. 7.4 we compare the predicted electron temperature and density at various pressures with the measurements of Gorbatkin et al.[40]. The experimental probe measurements were made at the ECR location ( $Z/L = 0.2$ ) and one downstream location ( $Z/L = 0.75$ ). The

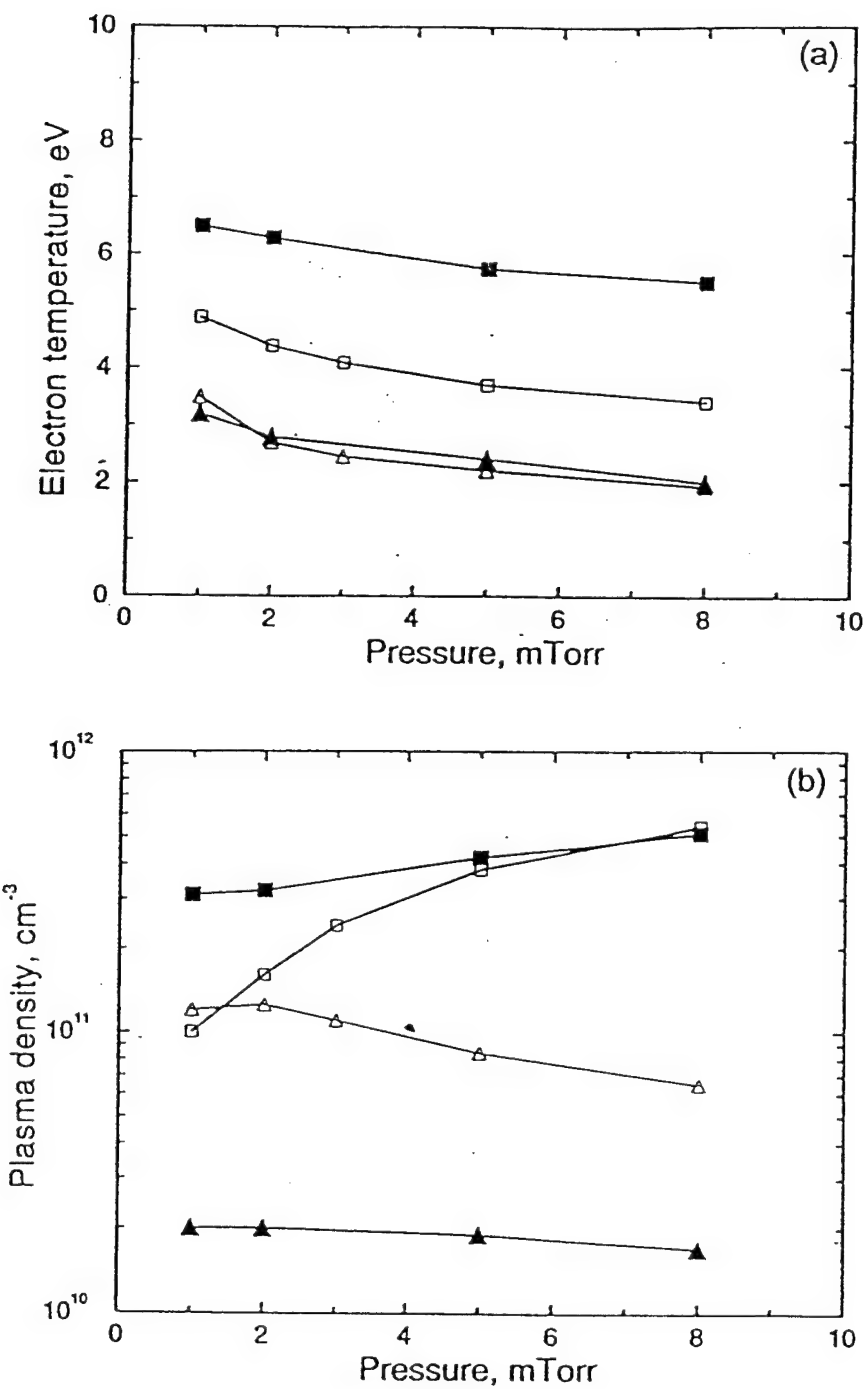


Fig. 7.4 (a) Electron temperature and (b) electron density as a function of pressure at 500 W at two locations:  $Z/L=0.2$  and 0.75. Full squares: source measurement from Ref. 40. Open square: source simulation. Full triangle: downstream measurement. Open triangle: downstream simulation.

agreement between theory and experiment in the case of electron temperature downstream is good. The agreement for the upstream temperature is actually better than it appears in Fig. 7.4a, if we recall that the model predicts radially-averaged temperature which would be somewhat smaller than the on-axis measurement. Two-dimensional discharge physics simulations[15] also show some radial variations in  $T_e$  in the source chamber, with an on-axis peak and relatively flat radial profiles in the process chamber. The comparison between model and experimental results for electron density in Fig. 7.4b does not appear as good as in Fig. 7.4a for the temperature. However, Gorbatkin, et al. discussed various causes of error in their electron density measurements, which are only accurate to a factor of 2-4[40]. Also, the size of the downstream chamber in the present analysis is different from that in ref. [40]. Considering the above, the model predictions seem reasonable and the trends appear to be correct.

## 8. Pulsed ECR Discharges

High density discharges using inductively coupled plasma (ICP) and electron cyclotron resonance (ECR) sources are used in etching and deposition applications which demand highly anisotropic features, critical dimension control, and processing uniformity over large areas. For a given reactor system and choice of feed gas mixture, the degree of success in meeting the goals on selectivity and processing rates depends on controlling the gas phase and surface chemistries. It is always desirable, but in practice extremely difficult, to promote favorable reaction pathways while suppressing others within the duration of the gas residence time. In chemical reaction engineering literature, one can find examples of time modulating the feed gas mixture rate or composition to "preselect" reaction channels for a given residence time. In conventional thermal chemistry, it is difficult to modulate the heat input to control reaction rate constants due to the high thermal inertia of the reactor systems. In contrast, it is relatively easy in plasma processing systems to modulate the microwave or rf power and affect reaction rates through the modulation of electron density and energy. Recently there have been several reports on successful selective etching of polysilicon [44-46] and control of fluorocarbon chemistry [47] through pulse time modulation of the microwave power in ECR discharges. Samukawa [44,45] achieved highly-selective, notch-free etching of polycrystalline silicon by pulsing an ECR chlorine plasma (10-100  $\mu$ s).

An understanding of mechanisms and the effect of process parameters is critical in process and equipment design, and process control. Hence, modeling of the plasma ECR reactors is undertaken here. The volume- or spatially-averaged model presented earlier is used for this purpose. A notable difference between this work and that in previous Sections 5 and 6 is that the time modulation requires time-periodic solution to the ordinary differential equations. A high-density chlorine discharge is modeled and the reaction set presented in Section 6 is used here. However, a Cl atom wall recombination coefficient of 0.1 is assumed in this section. A high-density  $\text{CF}_4$  discharge is also studied. Mass balance equations for 12 species, namely,  $\text{CF}_4$ ,  $\text{CF}_3$ ,  $\text{CF}_2$ ,  $\text{CF}$ ,  $\text{F}$ ,  $\text{F}_2$ ,  $\text{C}$ ,  $\text{C}^+$ ,  $\text{CF}_3^+$ ,  $\text{CF}_2^+$ ,  $\text{CF}^+$ , and  $\text{F}^+$  are written. A set of 19 reactions, including electron impact dissociation, ionization, and dissociative ionization is used. The wall recombination coefficient for ions is assumed to be 1.0; this process liberates the corresponding radicals. The coefficient of recombination for various radicals are 0.001, 0.001, 0.14, and 0.001 for  $\text{CF}_3$ ,  $\text{CF}_2$ ,

CF, and F, respectively. The governing ODEs were solved using a code called REAC. The solution procedure started with an initial guess for all species mass fractions and electron temperature. Each pulse was divided by 200-400 time steps and the equations at every time step were solved using an implicit procedure. Time marching was done until a time periodic solution was obtained, i.e., the relative change over one cycle was less than  $10^{-7}$ .

The results presented here are for a source chamber diameter,  $d = 30$  cm and length,  $L = 25$  cm. These dimensions are similar to those used by Samukawa [44-46]. Other parameters are as follows: pressure = 3 mTorr, flow rate = 30 sccm. A simple square wave modulation of the input power is considered. The pulse period (on + off time) is varied between 1 and 100  $\mu$ s. The duty ratio is defined as the ratio of power-on time to the total period. The time-averaged power is maintained at 300 W. For example, 25% duty ratio would have 1200 W during the on-part of the period and 0 during the remainder of the pulse period.

Results for a pulsed chlorine discharge are discussed first for the set of parameters given above and a base case of 100  $\mu$ s period and 25% duty ratio. Figure 8.1 shows densities and rates of key electron impact reactions during one period. The electron and positive ion densities increase during the on-part of the pulse, reach a maximum just when the power is turned off, and continue to decline during the remainder of the period. To understand this behavior, it is instructive to look at the behavior of electron temperature (See Fig. 8.2, 100  $\mu$ s and duty = 0.25). The time scale for power absorption by the electrons is very short and the electron temperature reaches its peak value nearly instantaneously. Once the power is turned off, the electron temperature drops below 1.0 eV within a few  $\mu$ s and decays slowly thereafter. At  $T_e$  below 1.0 eV, all electron impact reactions exhibit negligible rates, as seen in Fig. 8.1. During the on-part of the pulse, the production of ions and electrons far exceeds their loss to the wall by ambipolar diffusion and by volume recombination. Indeed, examination of the power spent on various processes during the first 25  $\mu$ s reveals that nearly 85% of the input power is accounted for by the inelastic collisions and the remainder is due to the energy loss of particles to the walls. Under these circumstances, the positive ions and electrons continue to pile up until the power is turned off. During the off-part of the cycle, production of ions and electrons ceases and particles are slowly lost to the wall, due to volume recombination. The densities are not negligible, though  $T_e$  is insignificant. If volume

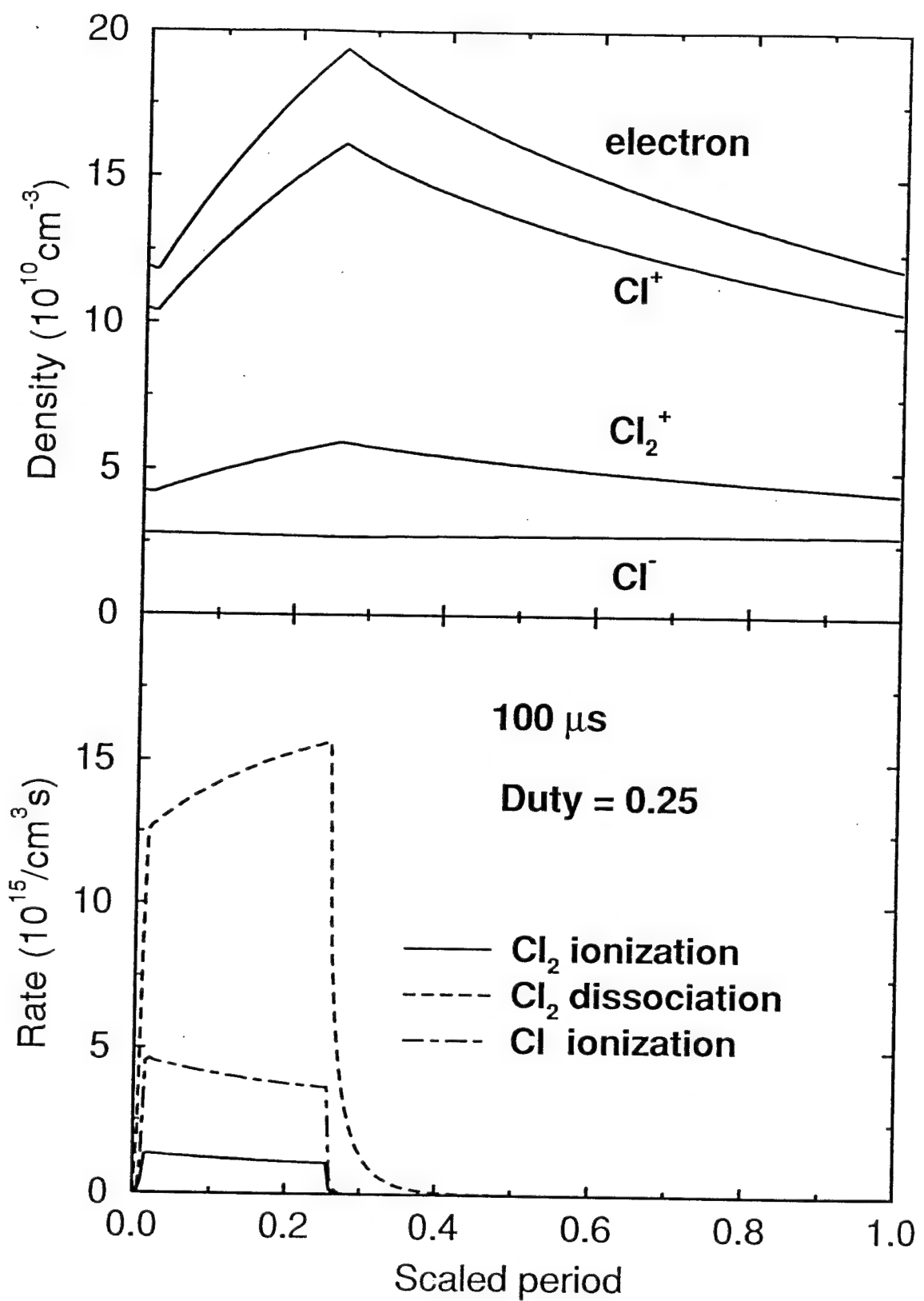


Fig. 8.1 Density of various species (top) and reaction rates (bottom) in a pulsed chlorine discharge. Duty ratio = 0.25; pulse period = 100  $\mu\text{s}$ ;  $p = 3 \text{ mTorr}$ ; flow = 30 sccm; and time-averaged power = 300 W.

recombination is small, then a mass balance for a positive ion during the pulse interval (off-period) reduces to:

$$V \frac{dn_+}{dt} = -A_{\text{eff}} n_+ u_B \quad (42)$$

Here,  $u_B$  is Bohm velocity,  $V$  is reactor volume, and  $A_{\text{eff}}$  is effective area for ion wall recombination written as  $(h_L 2\pi r^2 + h_R 2\pi r L)$  in Section 3. Recall that  $h_L$  and  $h_R$  are correction factors for the variation of the ion density at the sheath edge from its value in the bulk. Since electron temperature is nearly constant when there is no power,  $u_B$  may be taken to be time independent. Solution of Eq. (42) then is:

$$n_+ = n_{+0} e^{-t/t_d} \quad (43)$$

where  $n_{+0}$  is the density at the moment when the power is turned off.  $t_d$  is a decay time constant given by  $V/A_{\text{eff}} u_B$ . For a given reactor configuration, the pulse period and duty ratio can be chosen to obtain any value for  $n_+/n_{+0}$  between very small and near unity.

The negative ion shows no modulation in Fig. 8.1, though there is a slight increase in density not seen in the scale of the figure during the pulse interval. Negative ions are produced by dissociative attachment and, to a lesser extent, by dissociative ionization. They are lost by volume recombination. An approximate  $[\text{Cl}^-]$  balance for illustration here is given by

$$k_{\text{da}}[\text{Cl}_2][\text{e}] = k_{\text{rl}}[\text{Cl}^+][\text{Cl}^-] + k_{\text{r2}}[\text{Cl}_2^+][\text{Cl}^-] + k_{\text{re}}[\text{e}][\text{Cl}^-] \quad (44)$$

Rearranging,

$$[\text{Cl}^-] = \frac{k_{\text{da}}[\text{Cl}_2]}{k_{\text{rl}}[\text{Cl}^+]/[\text{e}] + k_{\text{r2}}[\text{Cl}_2^+]/[\text{e}] + k_{\text{re}}} \quad (45)$$

Here, the dissociative attachment coefficient ( $k_{da}$ ) is weakly dependent on  $T_e$ . Ion-ion recombination coefficients are constant. The modulation of ratios  $[Cl^+] / [e]$  and  $[Cl_2^+] / [e]$  during the period is not strong, though individually positive ions and electrons are modulated. Only electron - $Cl^-$  recombination shows some modulation due to  $T_e$ , but not strong enough in the present case to result in the time variation of  $Cl^-$ . The ratio of  $[e] / [Cl^-]$  is about 7 and the discharge is highly electronegative. The dissociation of chlorine is only moderate ( $Cl/Cl_2 = 5$ ). These are typical when the Cl atom wall recombination is high in ECR discharges, as seen by Ono, et al.[36]. When the recombination coefficient is 0.01 or lower, the fractional dissociation is close to unity and the discharge is electropositive, characterized by a high  $[e] / [Cl^-]$ , as seen in Section 6.

Next, the effect of duty ratio for a pulse period of 100  $\mu s$  is illustrated in Fig. 8.2. Note that the time-averaged power is maintained at 300 W. The instantaneous power during the on-period is higher as the duty ratio decreases. The peak electron temperature in a transient process then is higher at lower duty ratios. As duty ratio increases, the electron temperature slowly approaches the value corresponding to the continuous wave (cw) operation. The electron temperature drops to insignificant values a few  $\mu s$  after the power is off at all duty ratios. The peak in plasma density increases as the duty cycle decreases, which is due to the increase in  $T_e$  and electron impact creation of charged particles. Since a large portion of the peak plasma density is maintained for this reactor configuration according to the relation (43), the time-averaged plasma density itself is higher at lower duty cycles. The negative ion density (not shown here) increases only marginally with a decrease in duty ratio due to the near temperature-independence of the negative ion creation and destruction reactions (Eq. 45). While the increase in plasma density compared to cw operation is important for high processing rates, the ability to enhance selectivity is the key advantage of using pulsed discharges, as shown by Samukawa [44,45]. The potential difference ( $V_p - V_f$ ) driving the ions is found to be of the order 5.7  $kT_e$  for the cases investigated here. Since  $SiO_2$  etching rate is determined by the ion energy, it does not proceed effectively during the pulse interval. This enabled Samukawa [44,45] to obtain higher selectivities over  $SiO_2$  for both doped and undoped polysilicon etching than possible with cw operation.

Figure 8.3 illustrates the effect of pulse period for a fixed duty ratio of 0.25. In all cases, the electron temperature reaches its peak at  $t = 2 \mu s$ . Given the same power and rise time, the peak  $T_e$  is the same regardless of the pulse period. However, the transient  $T_e$  behavior at zero power

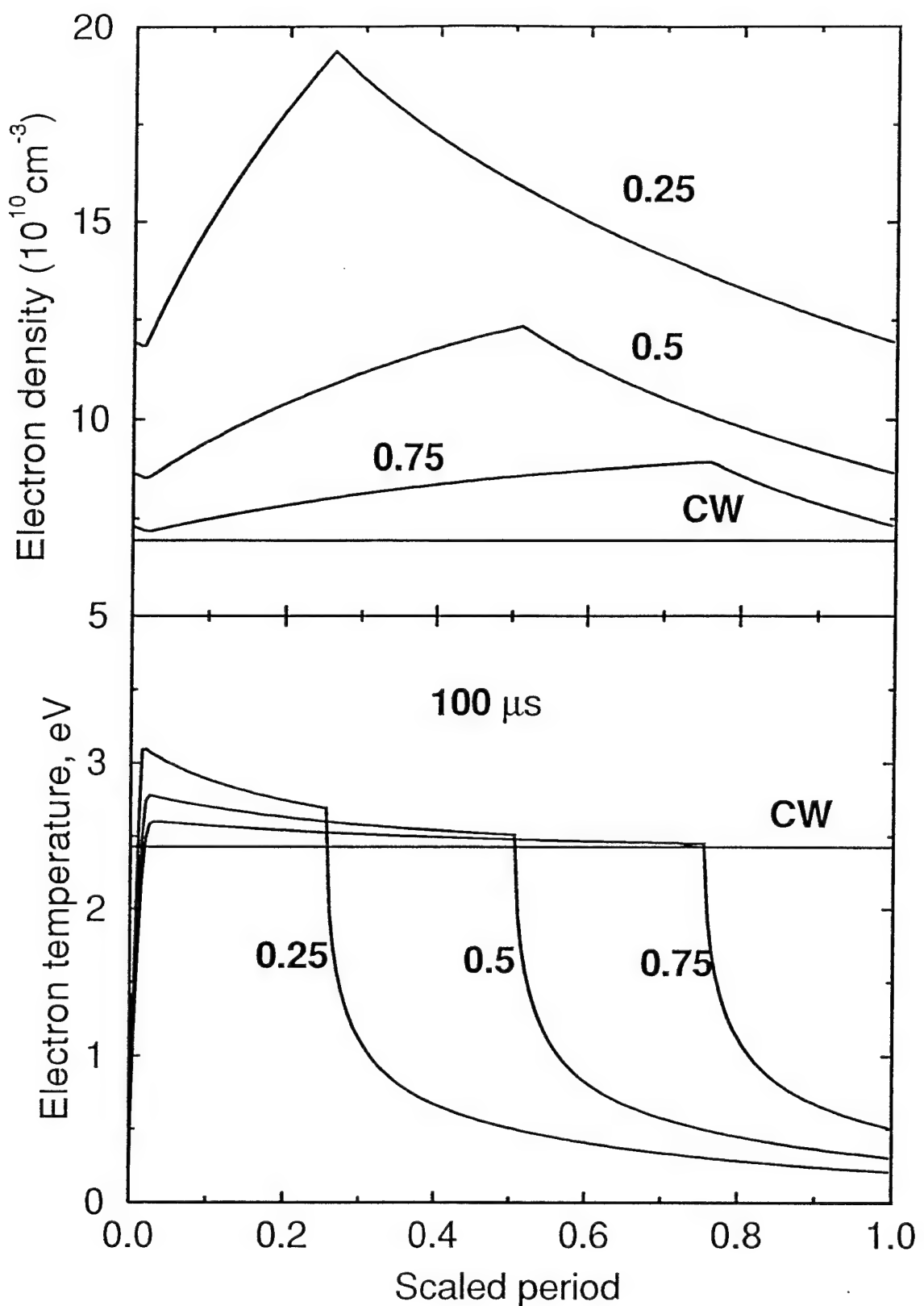


Fig. 8.2 Effect of duty ratio on electron density and temperature in a pulsed chlorine discharge. Time-averaged power is maintained at 300 W. Pulse period = 100  $\mu\text{s}$ .

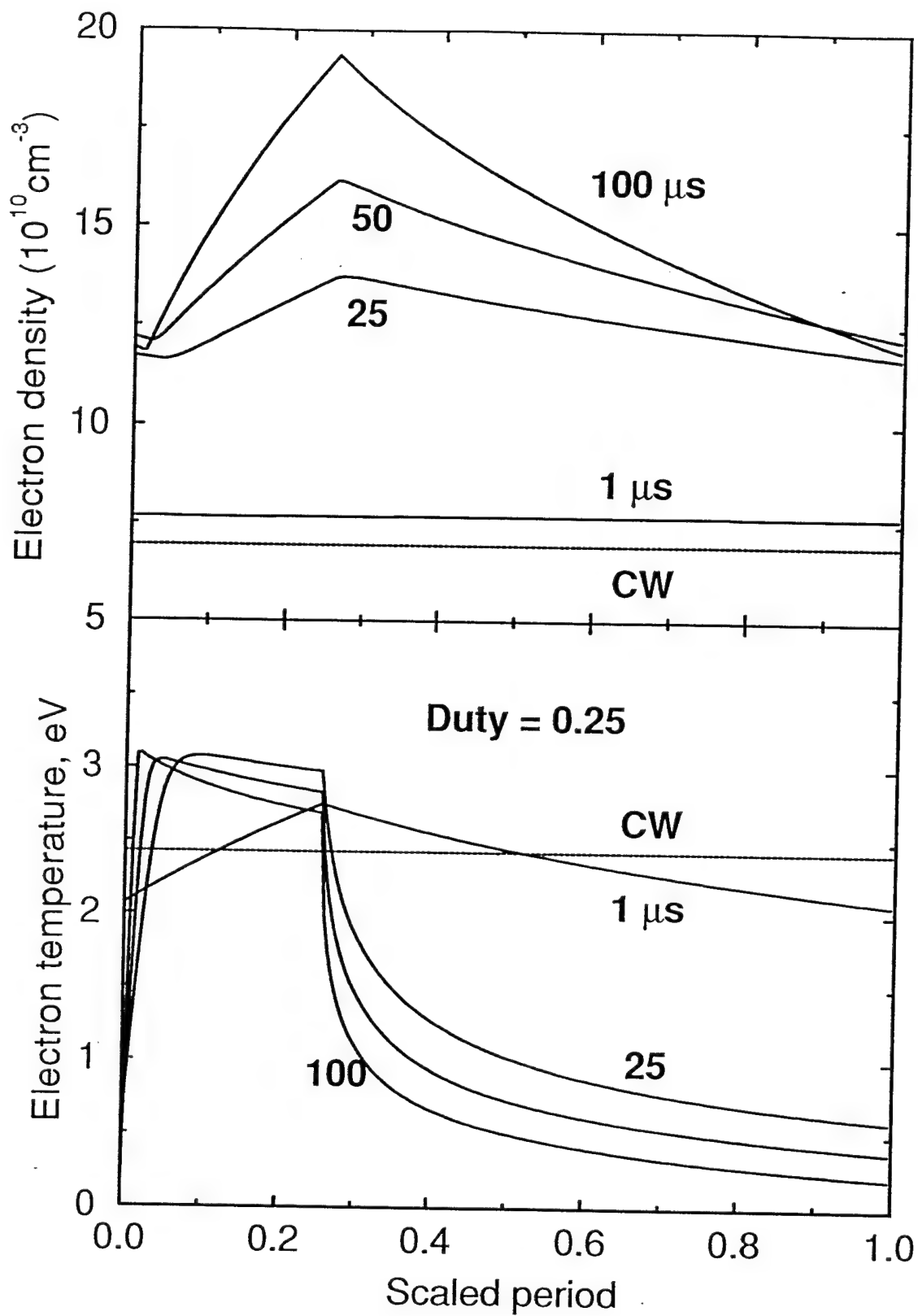


Fig. 8.3 Effect of pulse period on electron density and temperature in a pulsed chlorine discharge. Duty ratio = 0.25. Time-averaged power = 300 W.

depends on the period according to relation (43). At small periods ( $<1 \mu\text{s}$ ), the electron temperature asymptotically approaches to its cw value. The plasma density is higher with higher pulse period. Note that for intermediate values of pulse period, plasma production exceeds wall losses until the end of pulse width is reached. So, when the duty ratio is fixed and the period is varied, the above imbalance proceeds for longer pulse widths (duty ratio  $\times$  period) and results in increased plasma density.

In addition to the duty ratio and period, the flow rate was also varied and found to have negligible effect on the pulsed plasma characteristics. That is, the effect of flow rate on the pulsed discharge and cw discharge is the same. This is due to the fact that the residence time is of the order of ms. Both in cw and pulsed operation, the plasma density is not affected by the flow rate, which is consistent with the measurements by Tsujimoto, et al. [48]. However, as reported in Section 6, the degree of dissociation and hence the ratio of  $[\text{Cl}^+]/[\text{Cl}_2^+]$  are significantly affected by the residence time. Though Cl appears in most of the electron impact reactions considered in this study, an approximate Cl atom balance for illustration may be written considering only  $\text{Cl}_2$  dissociation:

$$-Q[\text{Cl}] + 2V\overline{k_d n_e}[\text{Cl}_2] - A k_w [\text{Cl}] = 0 \quad (46)$$

Here  $Q$  is the flow rate,  $k_w$  is the Cl atom wall recombination coefficient,  $k_d n_e$  is the rate constant for electron impact dissociation and the overbar denotes time-averaged value in the case of pulsed discharge. Rearranging Eq. (46) yields,

$$[\text{Cl}]/[\text{Cl}_2] = \frac{2V\overline{k_d n_e}}{Ak_w + Q} \quad (47)$$

At small values of  $k_w$ , the degree of dissociation is significantly affected, as  $Q$  is varied.

In Fig. 8.4, the pulsed plasma characteristics of a  $\text{CF}_4$  discharge are shown for a duty ratio of 0.25 and a period of  $300 \mu\text{s}$ . All other parameters are the same as in the chlorine case study. The electron temperature (not shown here) behaves in a manner similar to the chlorine case. It

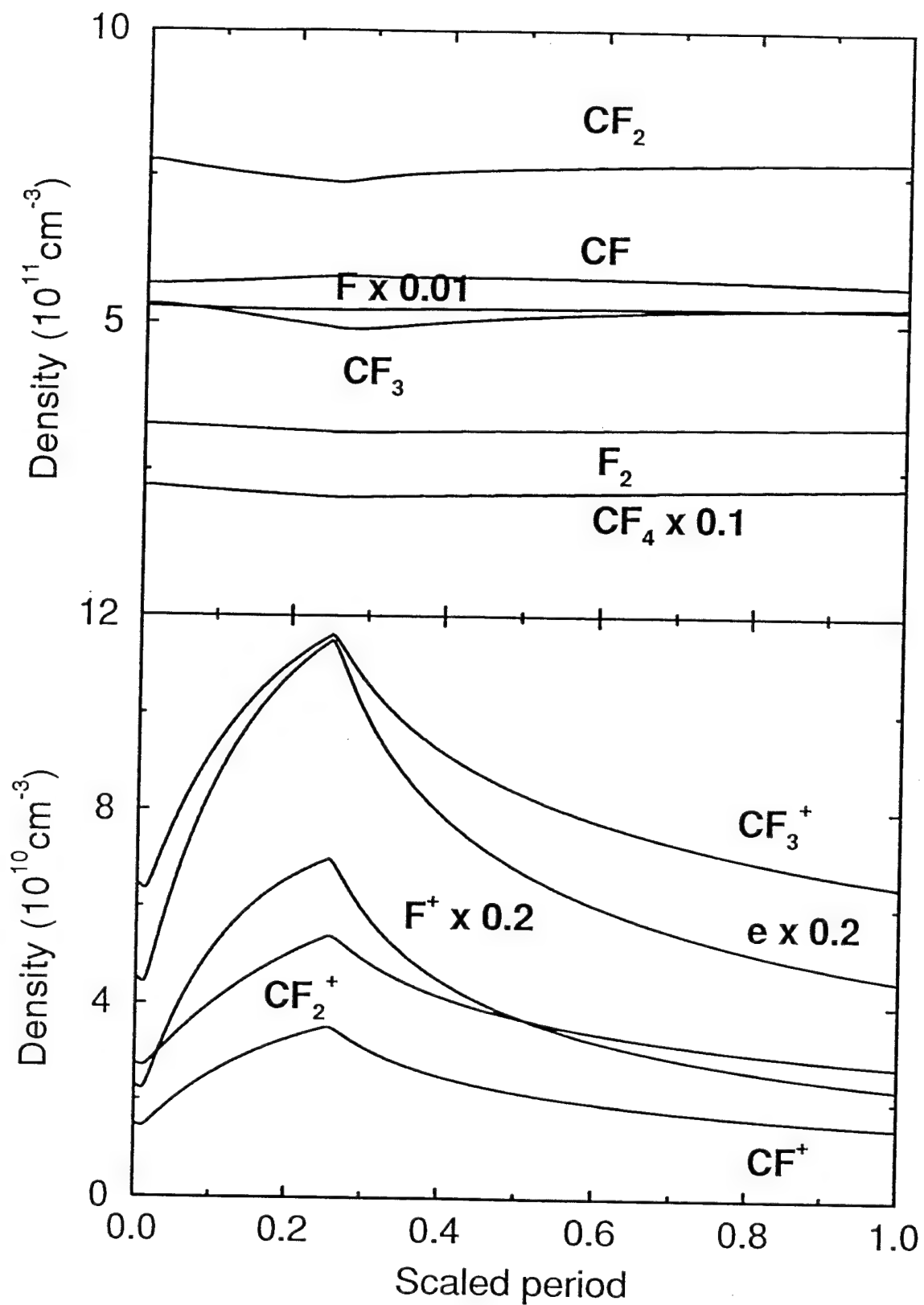


Fig. 8.4 Densities of radicals and ions in a pulse-modulated  $\text{CF}_4$  discharge. Period = 300  $\mu\text{s}$ ; duty ratio = 0.25; pressure = 3 mTorr; flow = 30 sccm; and time-averaged power = 300 W.

rises rapidly to a peak value of 4.1 eV and then decreases rapidly when the power is turned off at  $t = 75 \mu\text{s}$ . The corresponding  $T_e$  for cw operation is 2.9 eV. The plasma density is enhanced significantly, compared to the corresponding cw operation. However, the enhancement in radical densities is only marginal for a wide range of pulse widths and duty ratios.  $\text{SiO}_2$  etching is done with fluorocarbon gases, wherein a polymer is deposited on the underlying silicon and allows selective etching.  $\text{CF}_2$  radical is thought to be a key precursor for polymer deposition. Hence it is desirable to increase the ratio of  $[\text{CF}_2] / [\text{F}]$  in ECR discharges. Unfortunately, in a  $\text{CF}_4$  discharge, most of the reactions with low threshold energy that produce  $\text{CF}_2$  also produce F atoms. A case in point is the electron impact dissociation of  $\text{CF}_3$ , yielding  $\text{CF}_2$  and F, whose reaction rate is modulated well, with respect to other reactions, due to its low threshold of 3 eV. Dissociation of  $\text{CF}_2$  and CF, both of which produce F atoms, also has similar small threshold energies (4.5 and 2.5 eV, respectively). Hence, only a marginal increase in  $[\text{CF}_2] / [\text{F}]$  ratio is obtained in a pulsed discharge. In contrast,  $\text{CHF}_3$  appears to have potential for modulation of the rates of  $\text{CF}_2$  production,  $\text{CF}_2$  dissociation, and F production to obtain more selectivity than possible in a cw discharge [46].

## 9. 2-d Gas Flow Modeling

In general, plasma reactor modeling efforts in the literature often have neglected gas flow and heating related issues. Often, these issues have been regarded as secondary to striking and sustaining a plasma and subsequent processing. In contrast, the gas flow and heating issues are critical in ECR reactors. We have shown in previous chapters that the pressure in the reactor is not as nearly constant as in capacitively coupled rf reactors. Indeed, there is a tremendous pressure drop  $\Delta p$  from inlet to exit at pressures below 10 mTorr. Then the gas flow velocity is not constant in the flow direction. As was shown in the argon study, the gas velocity continues to increase in the source chamber and then decrease in the process chamber, since the latter usually has a larger cross section. Given all these considerations, it is important to examine the gas flow aspects of the ECR etching and deposition reactors.

We performed two-dimensional simulations using our 3-d code called MINT. Note that at low pressures typical of ECR operation, the gas does slip on the wall and there is a discontinuity in temperature between the wall (or substrate) and the adjacent gas molecule. These phenomena were included by modifying the traditional no-slip velocity and constant temperature boundary conditions in the following manner.

$$u_t = \pm \lambda \frac{\partial u_t}{\partial n} \quad (48)$$

$$T - T_w = \frac{2 - A}{A} \frac{2\gamma}{\gamma + 1} \frac{\lambda}{P_r} \frac{\partial T}{\partial n} \quad (49)$$

Here,  $n$  in the partial derivative represents the direction normal to the wall.  $u_t$  is tangential wall.  $T$  is the fluid temperature on the wall and  $T_w$  is wall temperature.  $\lambda$  is the gas mean free path.  $A$  is the accommodation coefficient.  $P_r$  is Prandtl number and  $\gamma$  is ratio of specific heats. Figure 9.1 shows flow streamlines on the left portion of the figure and pressure contours on the right. This reactor is the one used by Gorbatkin, et al. at ORNL [40]. The case corresponds to Gorbatkin's run of 5.2 mTorr (exit pressure at the throttle valve) and 80 sccm argon. The pressure at the inlet is predicted to be 6.16 mTorr, which is very close to the experimental result. The pressure drop is

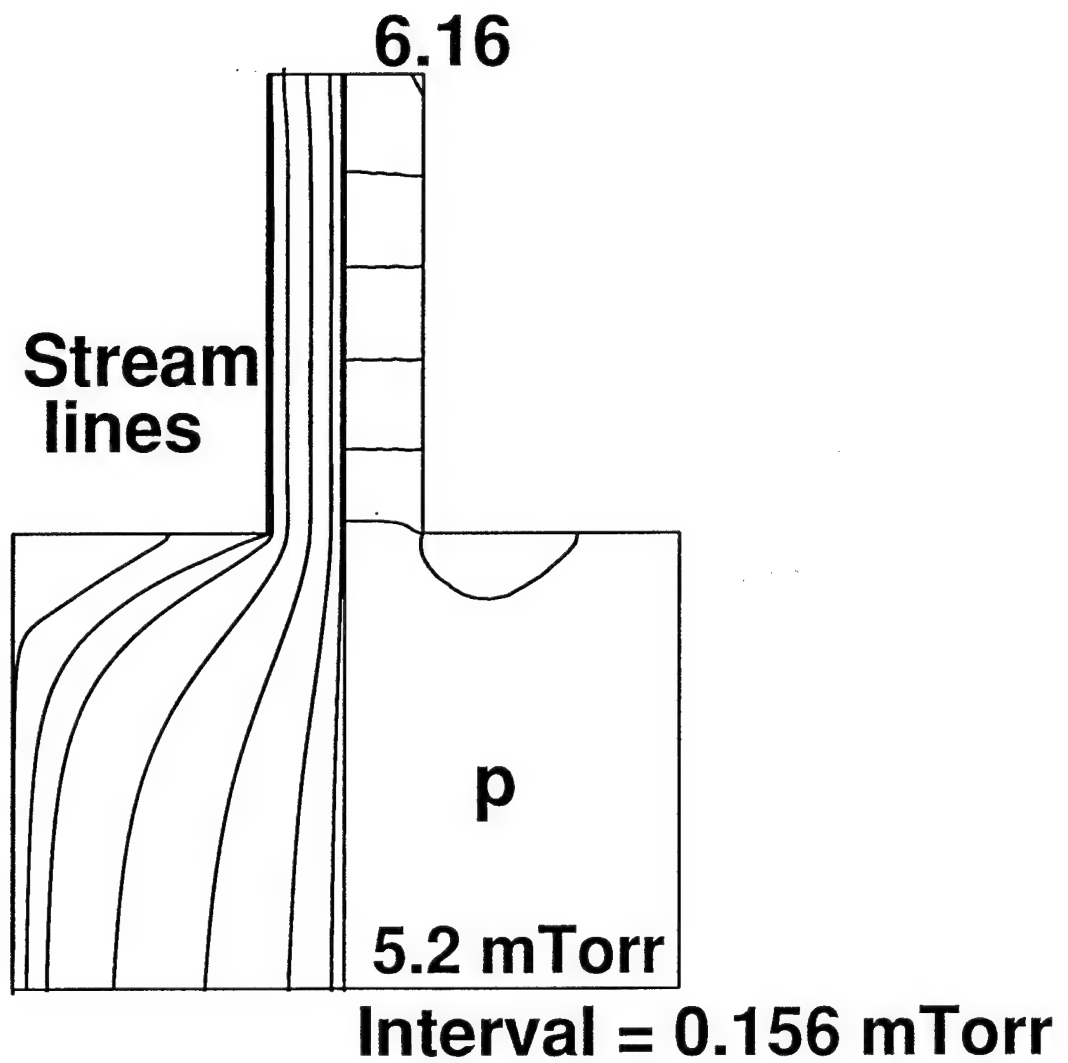
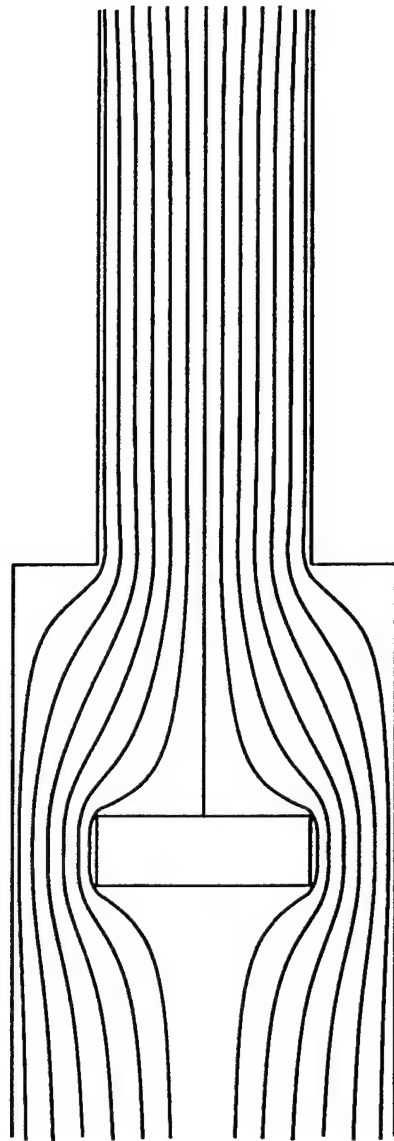


Fig. 9.1 Two-dimensional gas flow simulation of an ECR reactor from ref. [40]. Argon 80 sccm.  
Left: streamlines. Right: pressure contours.

significant (about 20%) and all of it happens in the source chamber, as seen in Fig. 9.1. The flow seems very smooth and is laminar.

Figure 9.2 shows chlorine flow (10 sccm) at 1 mTorr. Here, a substrate is placed in the downstream and the flow is shown to be squeezed around the substrate. There is, of course, a stagnation point on the up side of the substrate. So far, in both cases, we have a constant room temperature flow. It is important to point out that if Eq. (48) for slip velocity is not used, (a)  $\Delta p$  is overpredicted and (b) velocities are smaller for the same flow rate. That is, when the molecules on the wall have a non-zero tangential velocity, the entire flow moves faster and for a given mass flow, one only needs a lower  $\Delta p$  to push the mass through the reactors.

Next, a nitrogen case with a heated susceptor (540 K) is shown in Fig. 9.3. Here, Eq. (48) for slip velocity is used but Eq. (49) for temperature is not used to show its effect; in Fig. 9.4, the same case with Eq. (49) is shown with  $A = 0.5$ . The pressure drop is the same, 0.25 mTorr (or 25%) in a 1 mTorr case for 20 sccm nitrogen. The flow looks very similar. But, the temperature of the molecules near the substrate are 540 K in Fig. 9.3. When there is a temperature jump, the gas temperature adjacent to the substrate is only 365 K.



**1 mTorr, 10 sccm Chlorine**

Fig. 9.2 Flow streamlines in an ECR chlorine plasma.

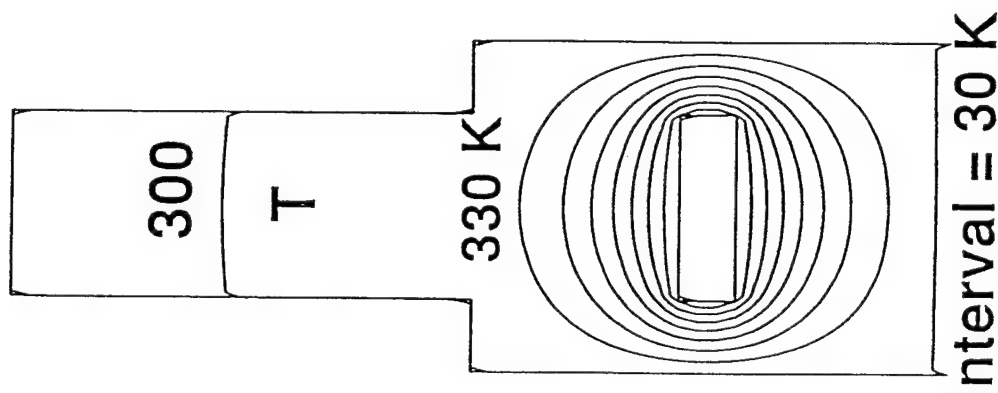
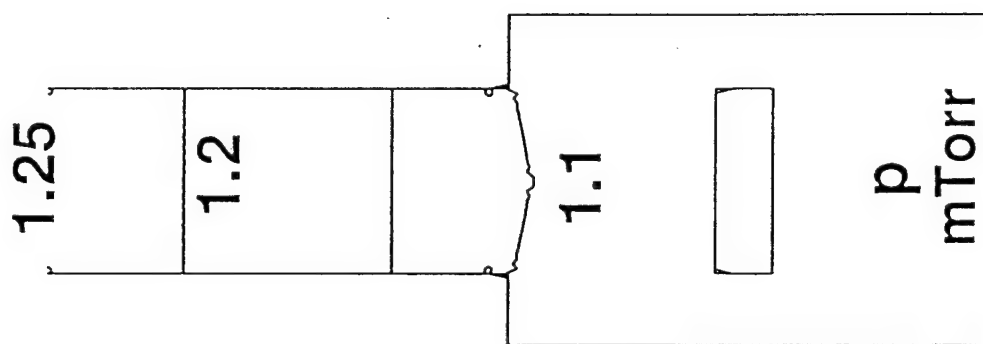
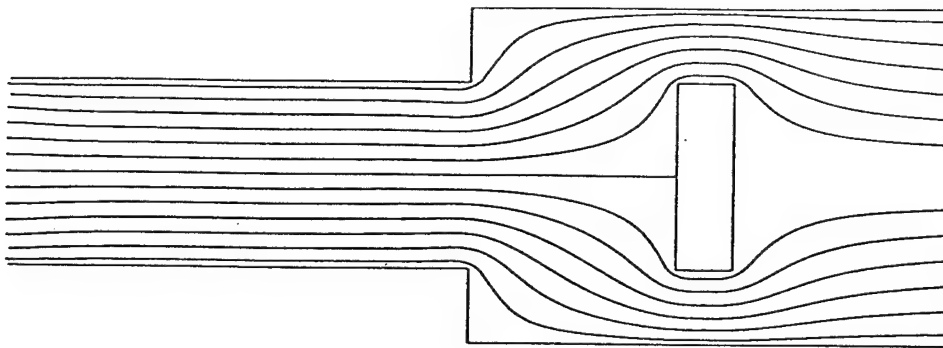
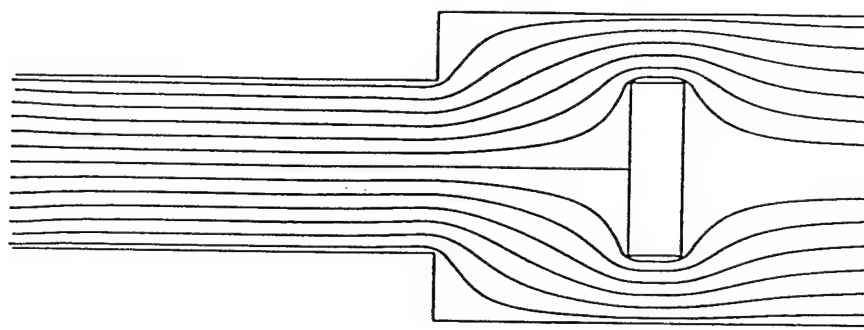
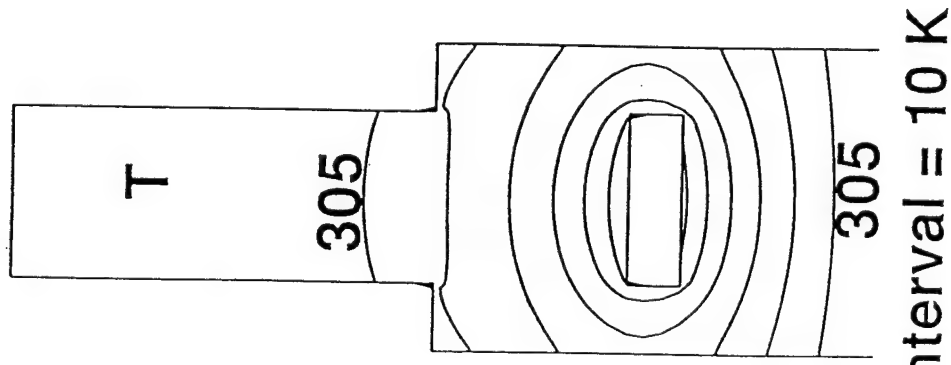
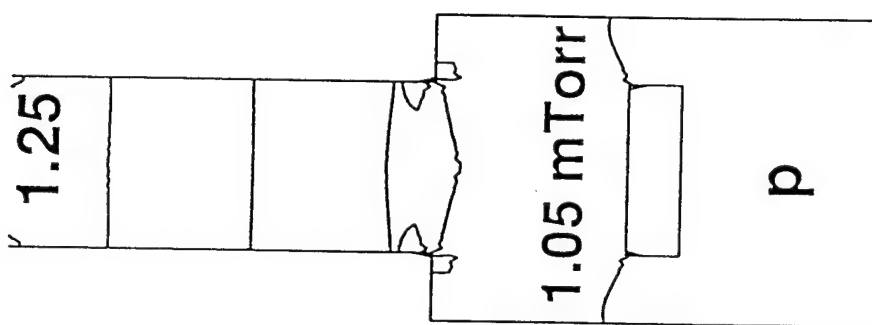


Fig. 9.3 Nitrogen in an ECR reactor. Left: temperature contours. Center: pressure contours. Right: streamlines. 1 mTorr exit pressure and 20 sccm. Eq. (49) is not used.



1 mTorr, nitrogen



Interval = 10 K

Fig. 9.4 Same as in Fig. 9.3 with temperature jump condition, Eq. (49).

## 10. Etching Studies

### A. $\text{CF}_4$ etching of silicon and $\text{SiO}_2$

This is an industrially important process, though recently  $\text{CHF}_3$  is increasingly being used. However, the chemistry for the latter is not as well known. The discharge physics and chemistry aspects without the presence of wafer must be studied prior to accounting for the details of surface reactions. The latter are not well known. Mass conservation equations for electrons and 12 species ( $\text{CF}_4$ ,  $\text{CF}_3$ ,  $\text{CF}_2$ ,  $\text{CF}$ ,  $\text{C}$ ,  $\text{F}$ ,  $\text{F}_2$ ,  $\text{CF}_3^+$ ,  $\text{CF}_2^+$ ,  $\text{CF}^+$ ,  $\text{C}^+$ , and  $\text{F}^+$ ) are written. With the addition of momentum and energy equations, the total number of coupled equations is 16. Table 10.1 presents the  $\text{CF}_4$  reaction set used in the simulations. The rate constants for the electron impact reactions were computed using a Maxwellian distribution and known cross sections. The cross sections for the electron impact dissociation of the radicals  $\text{CF}_x$  (reactions 14, 15, 16, and 17 in Table 10.1) are not well known. The dissociation energy in each case was calculated from the net heat of formation and the corresponding rate constant was assumed to be of the form  $k_o \exp(-E_{\text{dis}} / T_e)$  where  $k_o$  is the value fitted to reaction 12. There is no evidence for the formation of large amounts of  $\text{F}^-$  ions. The available kinetic data yields high densities of  $\text{F}^-$  and therefore reactions involving  $\text{F}^-$  are not included. This omission does not affect the general characteristics of the results presented here. Three body recombination reactions of  $\text{CF}_x$  radicals with  $\text{F}$  are included (reactions 20-23 in Table 10.1); however, their effect on the results is small in the pressure range considered here. The rate constants of various reactions in Table 10.1 are plotted in Fig. 10.1. The cross section for asymmetric charge exchange collisions ( $\text{CF}_x^+ + \text{CF}_y \rightarrow \text{CF}_x + \text{CF}_y^+$ ,  $x = 0-3$ ,  $y = 0-4$ ) is taken to be  $2.5 \times 10^{-15} \text{ cm}^2$ . The cross section for symmetric charge exchange collisions is  $5.0 \times 10^{-15} \text{ cm}^2$ . The information needed on electron elastic collisions can be approximated by  $N\mu = 5.4 \times 10^{21} (\text{cm.V.s})^{-1}$ .

All ions are assumed to readily recombine at the wall (unity sticking coefficient) and release the corresponding radical or atom. The sticking coefficient for  $\text{F} \rightarrow 0.5 \text{ F}_2$  is taken to be 0.001, though values in the literature range from  $4 \times 10^{-4}$  to  $4.8 \times 10^{-3}$ . The kinetics of adsorption of radicals and subsequent surface reactions, whether the wall is fluorinated or not, are not well

**Table 10.1  $\text{CF}_4$  Reaction Set**

	Reaction	Energy (eV)
1	$\text{e} + \text{CF}_4 \rightarrow \text{CF}_3^+ + \text{F} + 2\text{e}$	15.9
2	$\text{e} + \text{CF}_4 \rightarrow \text{CF}_2^+ + 2\text{F} + 2\text{e}$	22.0
3	$\text{e} + \text{CF}_4 \rightarrow \text{CF}^+ + 3\text{F} + 2\text{e}$	27.0
4	$\text{e} + \text{CF}_3 \rightarrow \text{CF}_3^+ + 2\text{e}$	8.5
5	$\text{e} + \text{CF}_3 \rightarrow \text{CF}_2^+ + \text{F} + 2\text{e}$	17.1
6	$\text{e} + \text{CF}_3 \rightarrow \text{CF}^+ + 2\text{F} + 2\text{e}$	21.4
7	$\text{e} + \text{CF}_2 \rightarrow \text{CF}_2^+ + 2\text{e}$	11.4
8	$\text{e} + \text{CF}_2 \rightarrow \text{CF}^+ + \text{F} + 2\text{e}$	14.6
9	$\text{e} + \text{CF} \rightarrow \text{CF}^+ + 2\text{e}$	9.1
10	$\text{e} + \text{C} \rightarrow \text{C}^+ + 2\text{e}$	8.0
11	$\text{e} + \text{CF}_4 \rightarrow \text{CF}_3 + \text{F} + \text{e}$	12.5
12	$\text{e} + \text{CF}_4 \rightarrow \text{CF}_2 + 2\text{F} + \text{e}$	15.0
13	$\text{e} + \text{CF}_4 \rightarrow \text{CF} + 3\text{F} + \text{e}$	20.0
14	$\text{e} + \text{CF}_3 \rightarrow \text{CF}_2^+ + \text{F} + \text{e}$	3.0
15	$\text{e} + \text{CF}_3 \rightarrow \text{CF} + 2\text{F} + \text{e}$	7.54
16	$\text{e} + \text{CF}_2 \rightarrow \text{CF} + \text{F} + \text{e}$	4.55
17	$\text{e} + \text{CF} \rightarrow \text{C} + \text{F} + \text{e}$	2.66
18	$\text{e} + \text{F}_2 \rightarrow \text{F} + \text{F} + \text{e}$	5.0
19	$\text{e} + \text{F} \rightarrow \text{F}^+ + 2\text{e}$	14.0
20	$\text{CF}_3 + \text{F} + \text{M} \rightarrow \text{CF}_4 + \text{M}$	—
21	$\text{CF}_2 + \text{F} + \text{M} \rightarrow \text{CF}_3 + \text{M}$	—
22	$\text{CF} + \text{F} + \text{M} \rightarrow \text{CF}_2 + \text{M}$	—
23	$\text{C} + \text{F} + \text{M} \rightarrow \text{CF} + \text{M}$	—

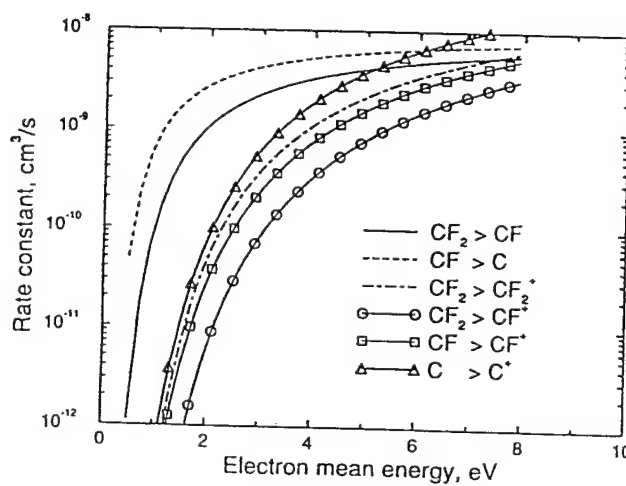
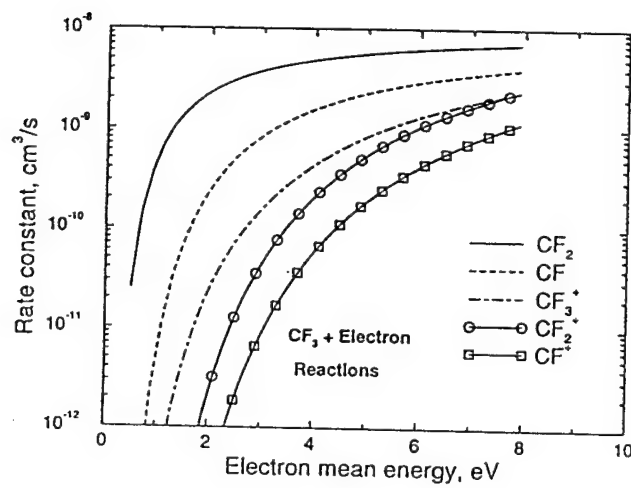
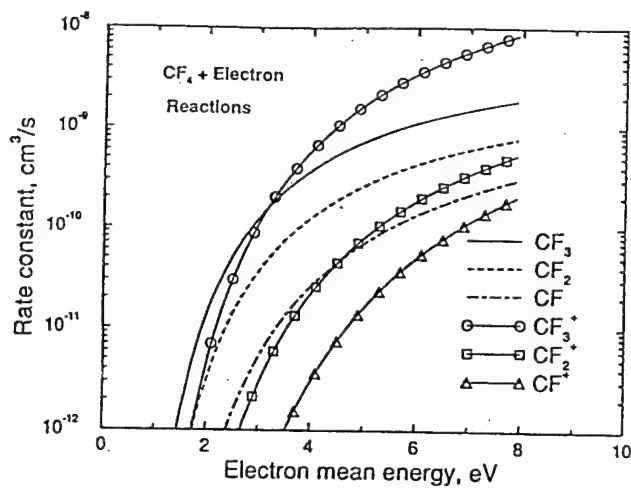


Fig. 10.1 Rate constants vs mean energy for reactions in Table 10.1

known. Sticking coefficient values for the radical from the literature were used and compared with the limiting case when the coefficients for all radicals are zero. The radical profiles, as expected, are somewhat different and there is a net loss of mass from the gas flow for the case of nonzero coefficients; the general plasma characteristics, particularly the electron properties, are not much affected.

An ECR reactor studied at the University of Wisconsin (Ashtiani, see Chapter 4) is considered here. The source chamber radius and length are 7.5 and 45 cm. The corresponding dimensions in the process chamber are 15 and 50 cm. All simulations reported here are for an absorbed microwave power of 500 W. The ECR resonance zone is located at  $z = 32$  cm. The shape of the power profile is similar to that used in the previous chapter for argon. Results are presented for a pressure range of 1-8 mTorr and two flow rates of 30 and 80 sccm. A limited comparison is made with available experimental data.

We begin with a discussion on the variation of pressure which has unique characteristics in low pressure, high density plasma reactors. Typically in high pressure plasma and non-plasma reactors operating in the 1-100 Torr range, the pressure drop  $\Delta p$  is small compared to  $p$ . In contrast, in ECR reactors operating below 10 mTorr, the  $\Delta p$  is large compared to the pressure itself. Figure 10.2 shows the variation of total pressure from inlet to the exit at two flow rates. Contribution of neutral and electron partial pressures to the total is also shown. Note that we fix the total pressure as boundary condition at the exit (which is 2 mTorr in Fig. 10.2) and “dial in” the desired mass flow at the inlet. This is typical of independent control of flow rate and pressure employed in reactor operation. Occasionally, experiments are done at low pressures with the throttle valve downstream fully open and the pressure is set by adjusting the mass flow rate; in this case, the two parameters are not independently controlled. In any case, the pressure drop required to push a given mass flow through the reactor would be unique, as will be seen. In Fig. 10.2, the contribution of electron partial pressure to the total is small near the inlet and exit, as expected; however, it consists of a significant fraction of the total pressure (20-25%) in the source chamber. The total pressure and neutral partial pressure decrease significantly from the inlet to the end of the source chamber. Indeed, when pressure at the exit is fixed at 2 mTorr, the pressure at the inlet is 4.74 mTorr for 30 sccm  $\text{CF}_4$  flow rate and 7.1 mTorr at 80 sccm. As expected, the required pressure drop increases with mass flow rate. In both cases, the total pressure decreases a little in

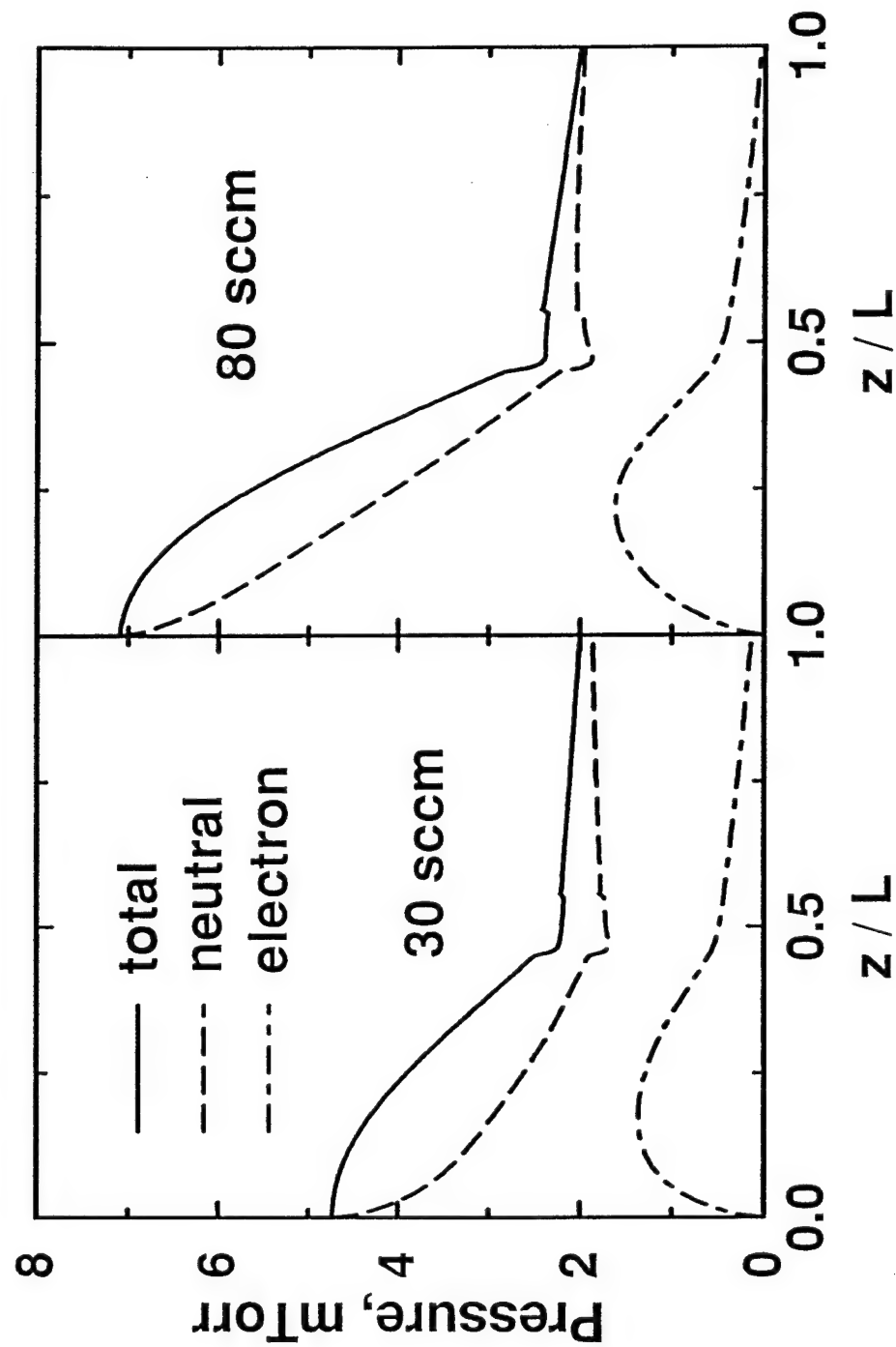


Fig. 10.2 Variation of pressure with normalized distance ( $z/L$ ) in an ECR reactor at  $\text{CF}_4$  flow rates of 30 sccm (left) and 80 sccm (right). The exit pressure is fixed at 2 mTorr. The ion partial pressures are included along with the neutrals since they are small.

the larger process chamber, whereas the neutral pressure after expansion into the process chamber increases slightly toward the exit.

**Table 10.2**

**Summary of Computed Pressures at the Inlet and at the Expansion to the Process Chamber.**  
**Exit pressure is fixed as boundary condition. ECR  $\text{CF}_4$  discharge at 500 W.**

Flow sccm	$p$ at exit mTorr	$p$ at expansion mTorr	$p$ at inlet mTorr
30	1	1.42	3.53
30	2	2.30	4.74
30	3	3.22	5.75
30	4	4.17	6.68
30	5	5.14	7.6
30	8	8.09	10.32
80	2	2.57	7.1
80	5	5.33	10.3

Table 10.2 provides a summary of computed pressures at the inlet and at the expansion to the process chamber for various values of exit pressure at the throttle valve location. The  $\Delta p$  required for a given mass flow depends dominantly on mass flow and little on the pressure itself. For example, the  $\Delta p$  for 30 sccm is nearly the same, about 2.7 mTorr, at all pressures, as seen in Table 10.2, while it is about 5.1 mTorr for 80 sccm. Note that in all cases the pressure drop in the process chamber is typically small and decreases with an increase in  $p$ . Table 10.2 also shows, consistent with Fig. 10.2, that most of the  $\Delta p$  is across the source chamber. This is just the normal viscous pressure drop along a pipe. To provide further evidence, we performed two-dimensional fluid dynamics simulations of only the gas flow in the absence of microwave power and any plasma, as described in Section 9. Figure 10.3(a) shows the streamlines and pressure contours at 2 mTorr exit pressure for a 30 sccm  $\text{CF}_4$  flow rate. The corresponding inlet pressure is only about 2.5

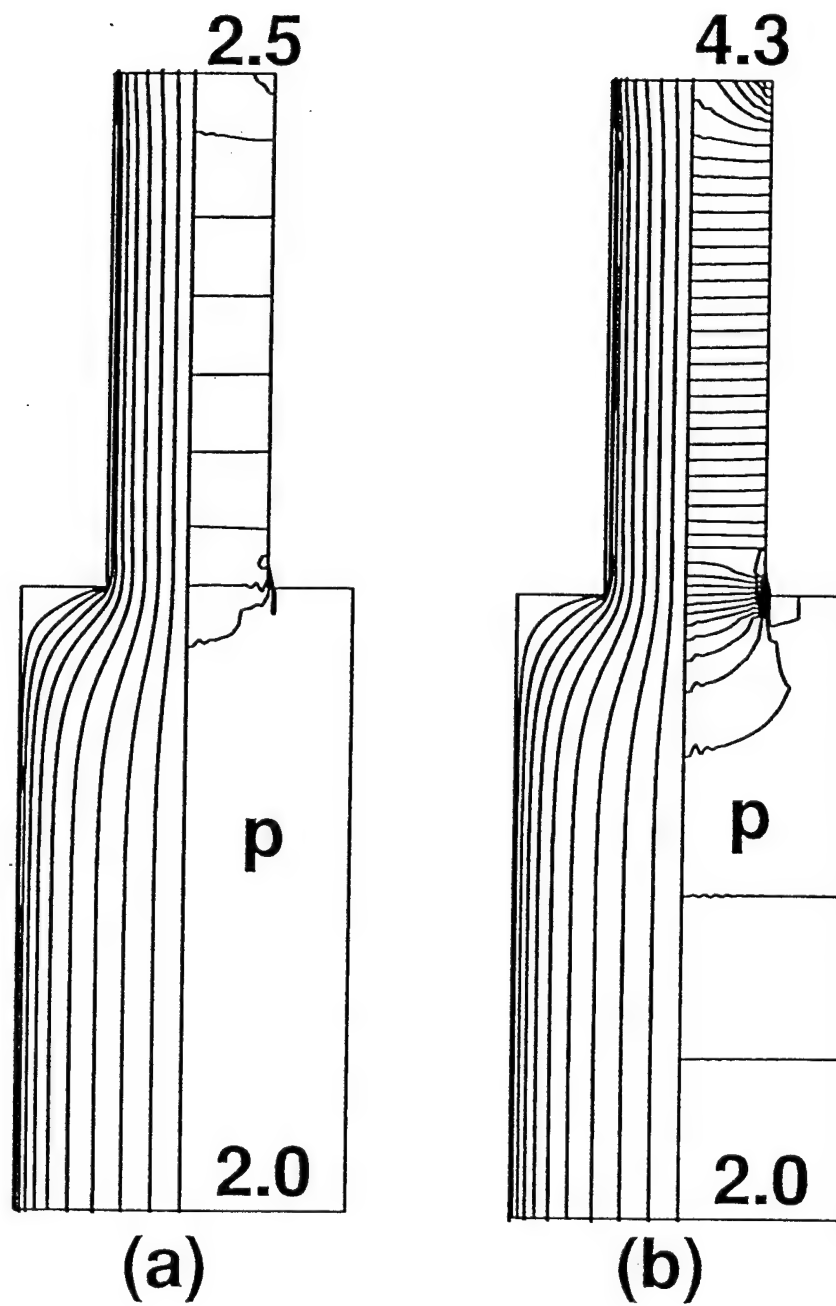


Fig. 10.3 Two-dimensional results of gas flow without the plasma at 2 mTorr (exit at the bottom). (a) 30 sccm CF<sub>4</sub> and (b) hypothetical case with the properties of F at the same mass flow rate of 30 sccm CF<sub>4</sub>. In each case, streamlines are shown on the left and pressure contours (interval = 0.05 mTorr) on the right. Slip velocity is included at the boundary.

mTorr, which is substantially smaller than that seen earlier. Note that in the ECR reactor,  $\text{CF}_4$  dissociates heavily and F is the major constituent (> 80%), in addition to significant amounts of carbon. The latter two are lighter components relative to  $\text{CF}_4$ . Therefore, a hypothetical case with the transport properties of F and same mass flow as 30 sccm  $\text{CF}_4$  was simulated (Fig. 10.3(b)). The inlet pressure in this case is 4.3 mTorr, which is close to that in Fig. 10.2 and Table 10.2; obviously there is some difference due to the electron partial pressure. Similar gas-flow-only simulations of each case in Table 10.2 provided the same conclusion. The observations on pressure presented thus far are similar to the predictions for an ECR argon discharge presented in an earlier chapter; recall that the latter compared well with the pressure measurements of Gorbatkin, et al. [40]. The strong variation of pressure has implications in processing as pressure determines the plasma characteristics and reaction rates. Also, the position of pressure measurement in reactors then becomes important.

Figure 10.4 shows profiles of electron density and temperature at 2 mTorr exit pressure for 500 W absorbed power and 30 sccm  $\text{CF}_4$  flow rate. The electron temperature peaks at the resonance zone. Though the power is deposited over a narrow region of approximately 1 cm, electron thermal conduction plays a significant role in diminishing the gradient. The electron temperature near the microwave window inlet region is about 2.6 eV. The temperature is also persistently high in the process chamber. The electron density peaks before the resonance zone where the neutral density and temperature are still large. Indeed, all the ionization rates (not shown here) also peak in the same vicinity. The electron density in the process chamber is relatively high. Ionization of  $\text{CF}_4$  and the radicals, after peaking in the source chamber, diminish in the process chamber due to their smaller densities; however, ionization of F continues since F atom concentration and electron temperature are significant in the process chamber (see Fig. 10.7) which may explain the large electron density there. Figure 10.4 also shows experimental data on electron density at 2 mTorr. The single data point in the source corresponds to microwave interferometry measurement of spatially-averaged electron density. The comparison of prediction and data here is good. The experimental data downstream represent probe data on or near the axis. In this case, the model predictions are higher. In general, given the uncertainties and assumption of constant density in the measurements and uncertainties in the kinetic data in the model, the agreement is reasonable.

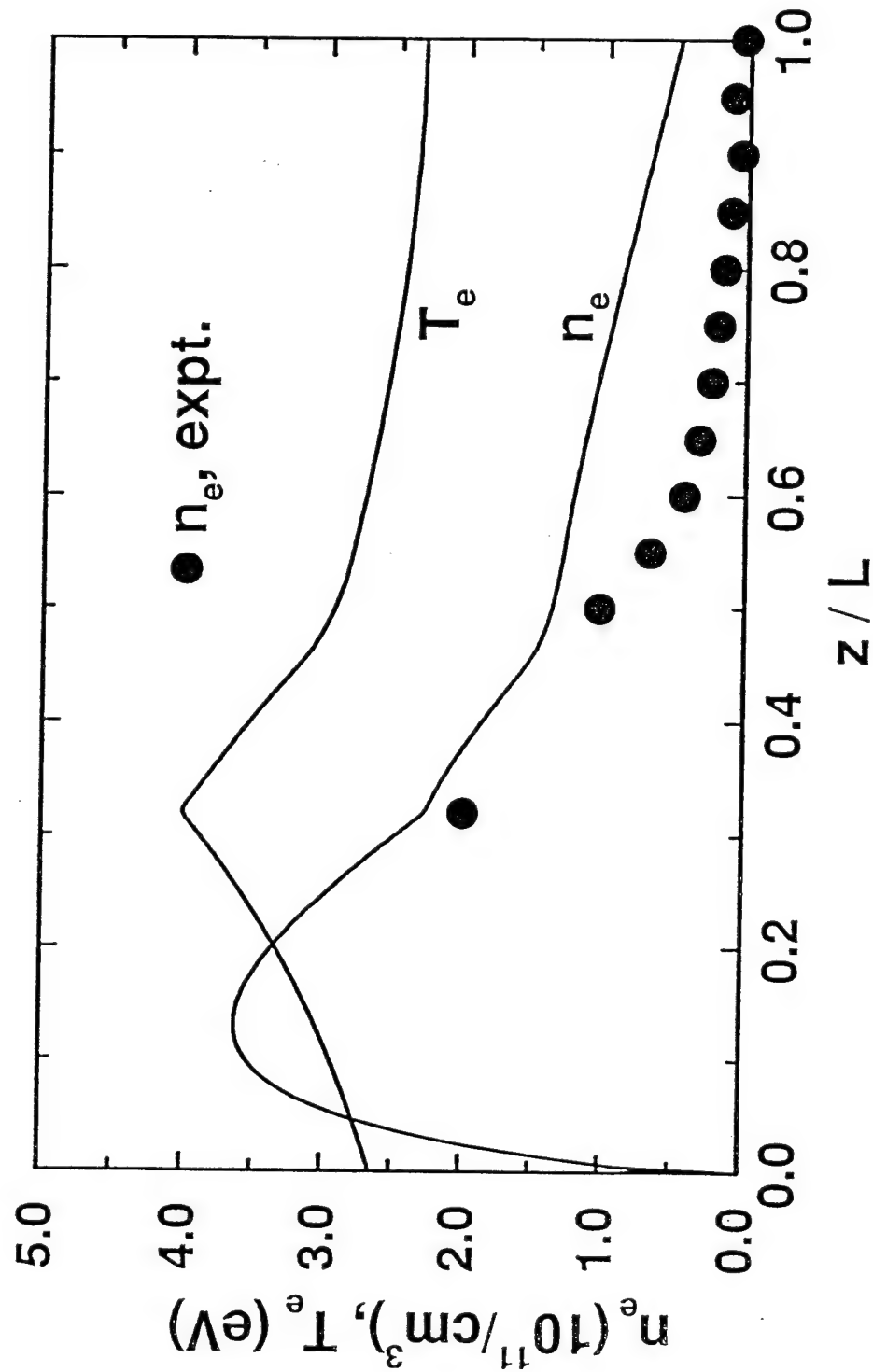


Fig. 10.4 Profiles of electron density ( $n_e$ ) and temperature ( $T_e$ ) in an ECR reactor at 500 W of absorbed microwave power, 2 mTorr exit pressure, and 30 sccm  $\text{CF}_4$  flow rate. Probe measurements of electron density (Ashtiani, Chapter 4) are also shown (filled circles).

Figure 10.5 illustrates the effect of pressure on plasma properties. Peak electron temperature at the ECR zone, peak electron density in the source, and values of electron density and temperature close to the exit in the process chamber are plotted. Electron temperature everywhere decreases with an increase in pressure, which is well known. The slope of  $T_e$  vs.  $p$  in the process chamber is somewhat steeper than in the source. This may be due to a decrease in electron thermal conductivity with an increase in pressure; the electron temperature gradients are found to be slightly higher as the pressure increases. The electron density in the source increases with the pressure since the neutral density increases. In contrast, the electron density in the process chamber exhibits a peak near 2 mTorr and decreases with a further increase in pressure. This is caused by the significant reduction in local ionization due to lower electron temperature. Plasma characteristics for 80 sccm  $CF_4$  flow rate are also shown in Fig. 10.5 for comparison. Typically, the electron temperature is lower by about 0.5 eV when the flow rate is increased from 30 to 80 sccm. Intuitively, one does not expect a significant change in electron properties when flow rate is varied, though the residence time alters the local composition of various neutrals. However, the change in flow rates in low pressure reactor operation is accompanied by upstream pressure changes, as discussed earlier. This in effect causes the differences in electron properties at the two flow rates plotted in Fig. 10.5.

The variation of neutral temperature and mass-averaged velocity of the gas mixture is shown in Fig. 10.6. The gas heating is mainly due to charge exchange collisions with the ions, with a minor contribution from elastic collisions and other reactions. Heat is lost to the ambient through the radial walls. The gas temperature peaks in the source region due to the high local ion densities. The gas temperature increases as reactor pressure is increased, since the ion density and number of charge exchange collisions increase. For example, the peak gas temperature in the source is about 600 K at 8 mTorr exit pressure. The mass-averaged velocity increases rapidly in the source chamber and decreases thereafter with a sudden expansion into the larger process chamber. Typical Mach numbers based on gas velocity and temperature in this study range from 0.01 to 0.2. Though the allowance for slip at the wall reduces the velocity gradient in the radial direction, the large  $\Delta p/p$  and the resulting continuous increase in velocity would not justify a simplified plug flow assumption as commonly done in high pressure diode reactors.

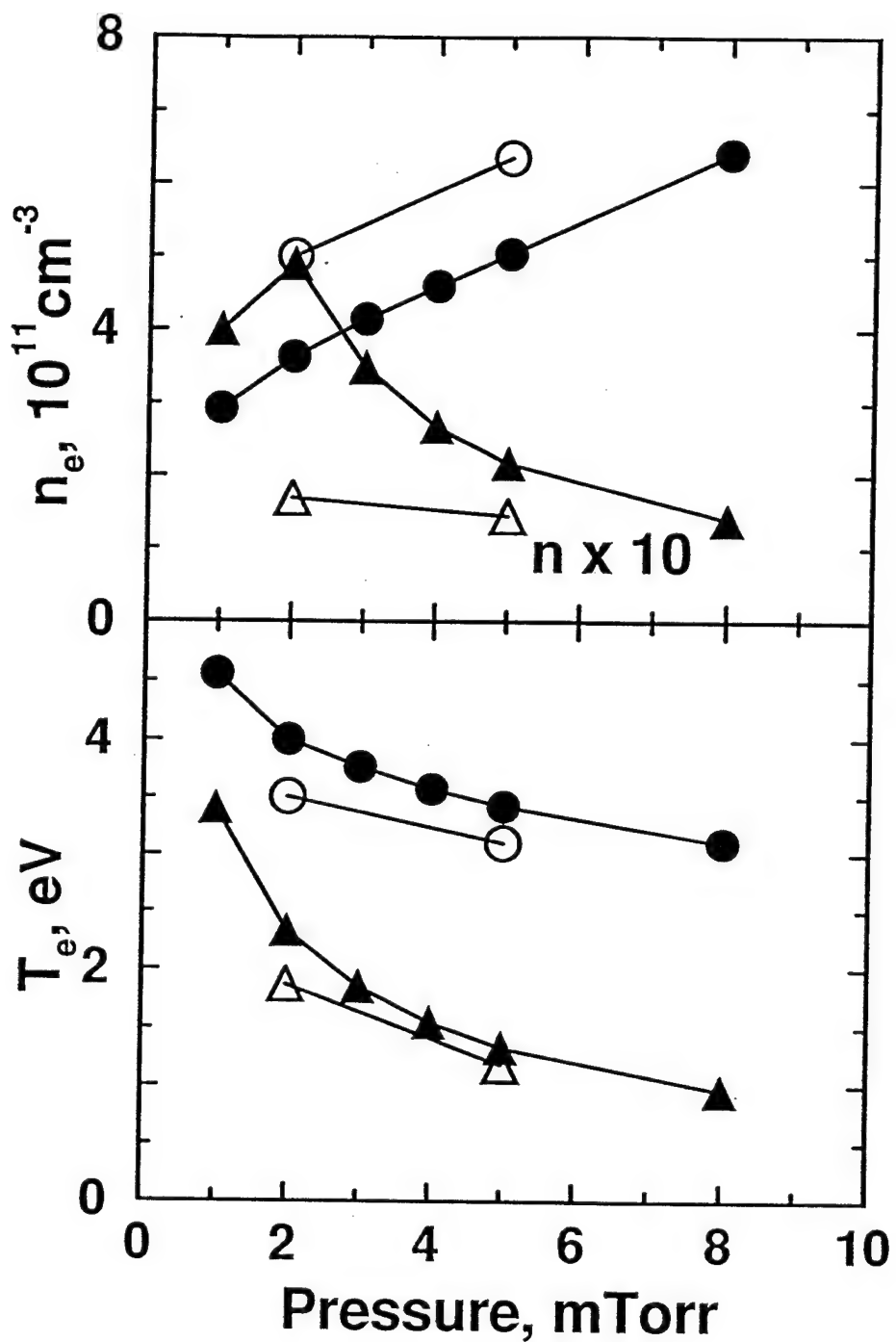


Fig. 10.5 Electron density ( $n_e$ ) and temperature ( $T_e$ ) as a function of pressure at 500 W power. Filled symbols: 30 sccm; open symbols: 80 sccm. Circles: peak values in the source chamber; triangles: downstream in the process chamber. Electron density in the process chamber is multiplied by 10 to fit the scale of the figure.

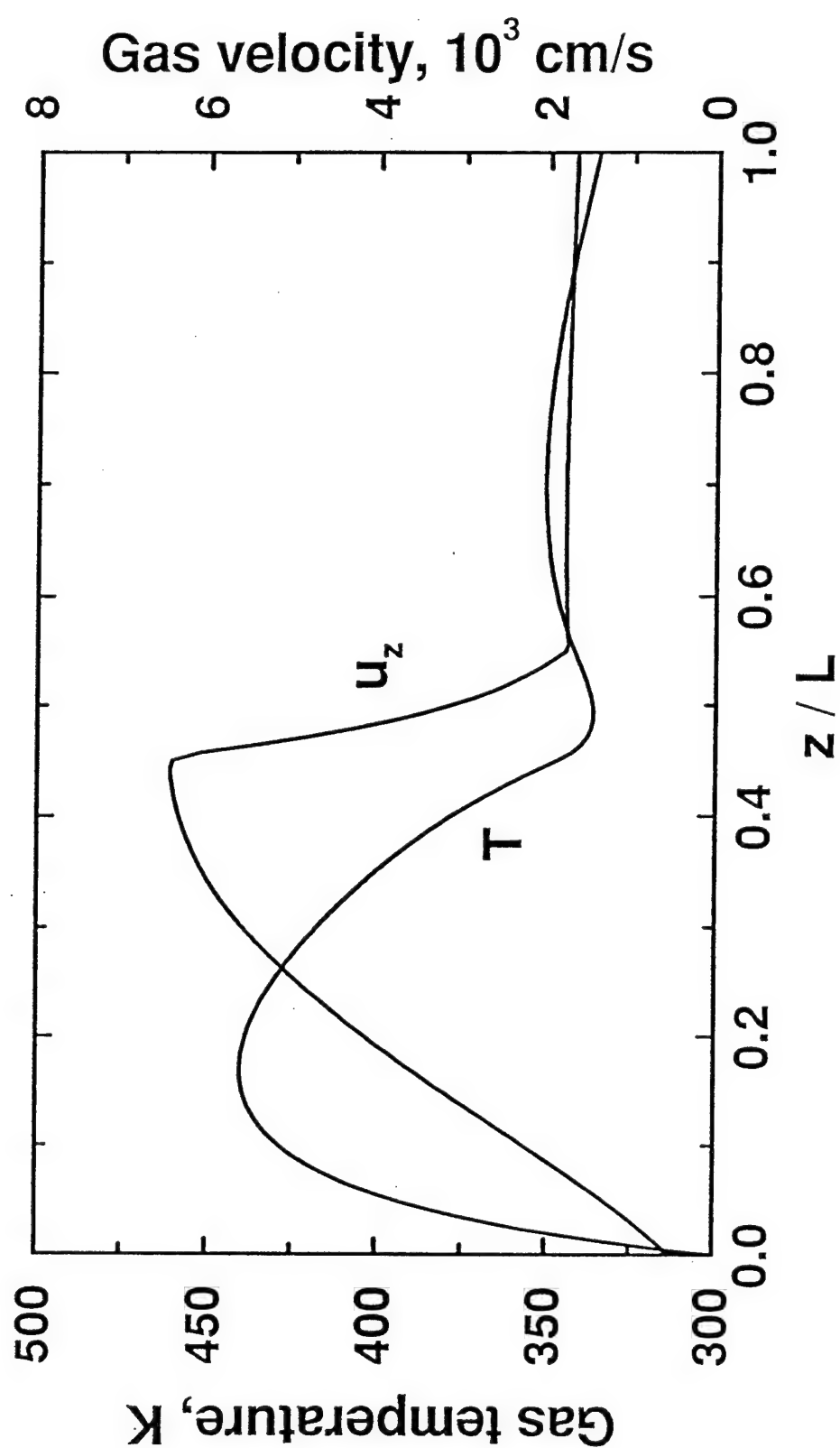


Fig. 10.6 Profiles of neutral temperature and mass-averaged mixture velocity in an ECR CF<sub>4</sub> discharge. Conditions: exit pressure = 2 mTorr, power = 500 W, and flow = 30 sccm.

Variation of neutral and ion densities along the length of the ECR reactor is presented in Fig. 10.7. The reactor conditions are 2 mTorr exit pressure and 30 sccm flow rate. The feed gas  $\text{CF}_4$  is essentially depleted due to intense dissociation. At 5 mTorr and 80 sccm, only 10% (by mass) of the  $\text{CF}_4$  is left. The radical densities peak in the source chamber, not too far from the inlet, since local  $\text{CF}_4$ , electron density, and temperature are sufficiently large. Since all radicals undergo further dissociation and ionization, the radical densities continue to decrease toward the exit. The F atom concentration is high throughout the reactor (not shown here). There is also a significant concentration of carbon atoms; for example,  $6 \times 10^{12} \text{ cm}^{-3}$  in the process chamber at 2 mTorr. The mixture molecular weight decreases close to 20 at the exit from 88 at the inlet. The prediction of  $\text{CF}_3^+$  is close to that reported by Ashtiani, et al. [49] ( $\approx 10^{10} \text{ cm}^{-3}$  in the process chamber). The effect of pressure on radical densities is illustrated in Fig. 10.8. The F atom concentration in the source increases with pressure. The predictions here are in the same range as the actinometric measurements by Jenq, et al.[50]. A direct comparison cannot be made since the flow rates were adjusted in ref. 22 to obtain the desired pressure.  $\text{CF}_2$  densities are larger than  $\text{CF}_3$  in the process chamber. The predictions of  $\text{CF}_2$  concentration are reasonable compared to IR absorption measurements[49] shown in Fig. 10.8, though the experimental trend cannot be confirmed with only three data points in a narrow range of 1.5 - 2.5 mTorr.

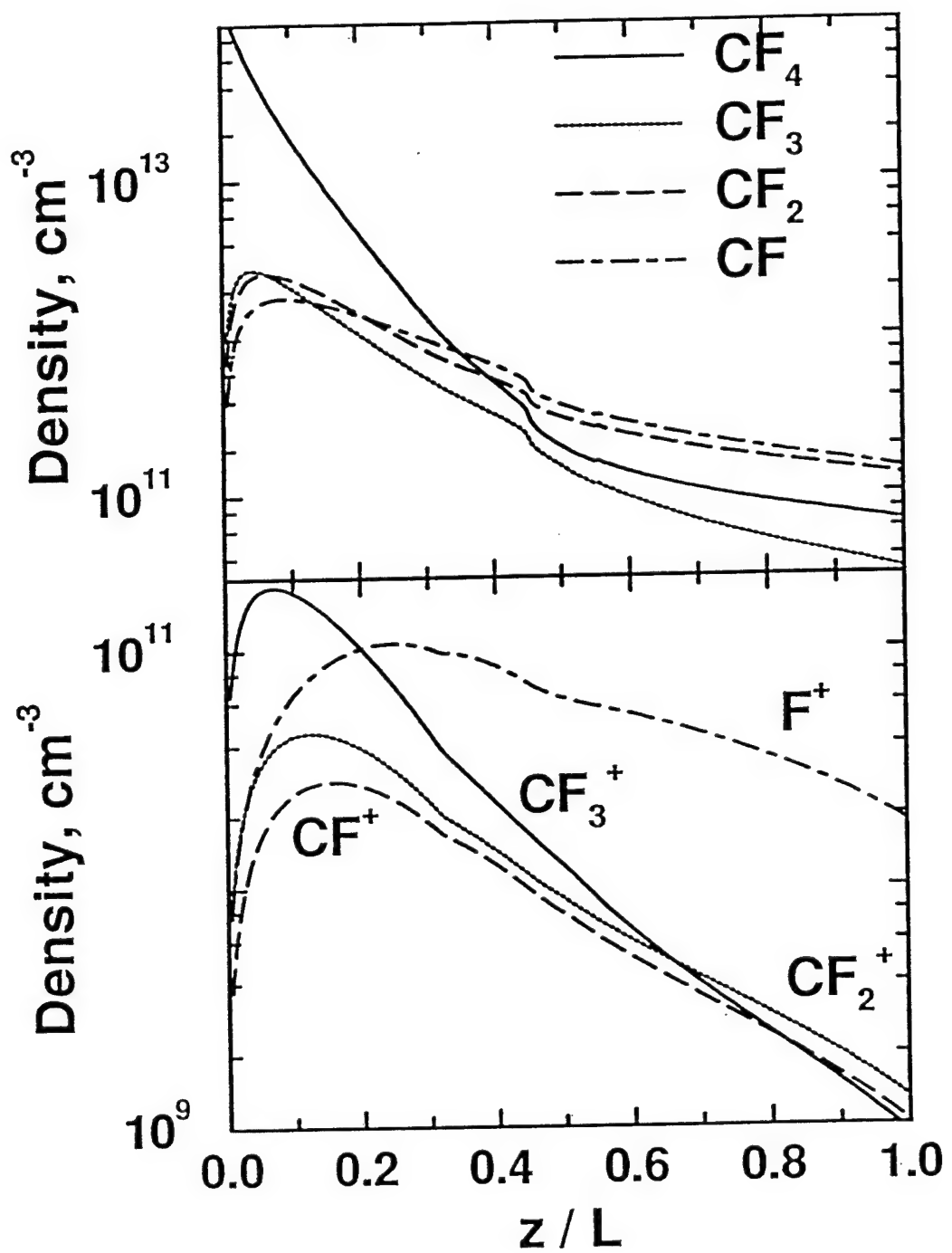


Fig. 10.7 Density profiles at 2 mTorr and 30 sccm  $\text{CF}_4$ .  
 $z/L$  is normalized distance.

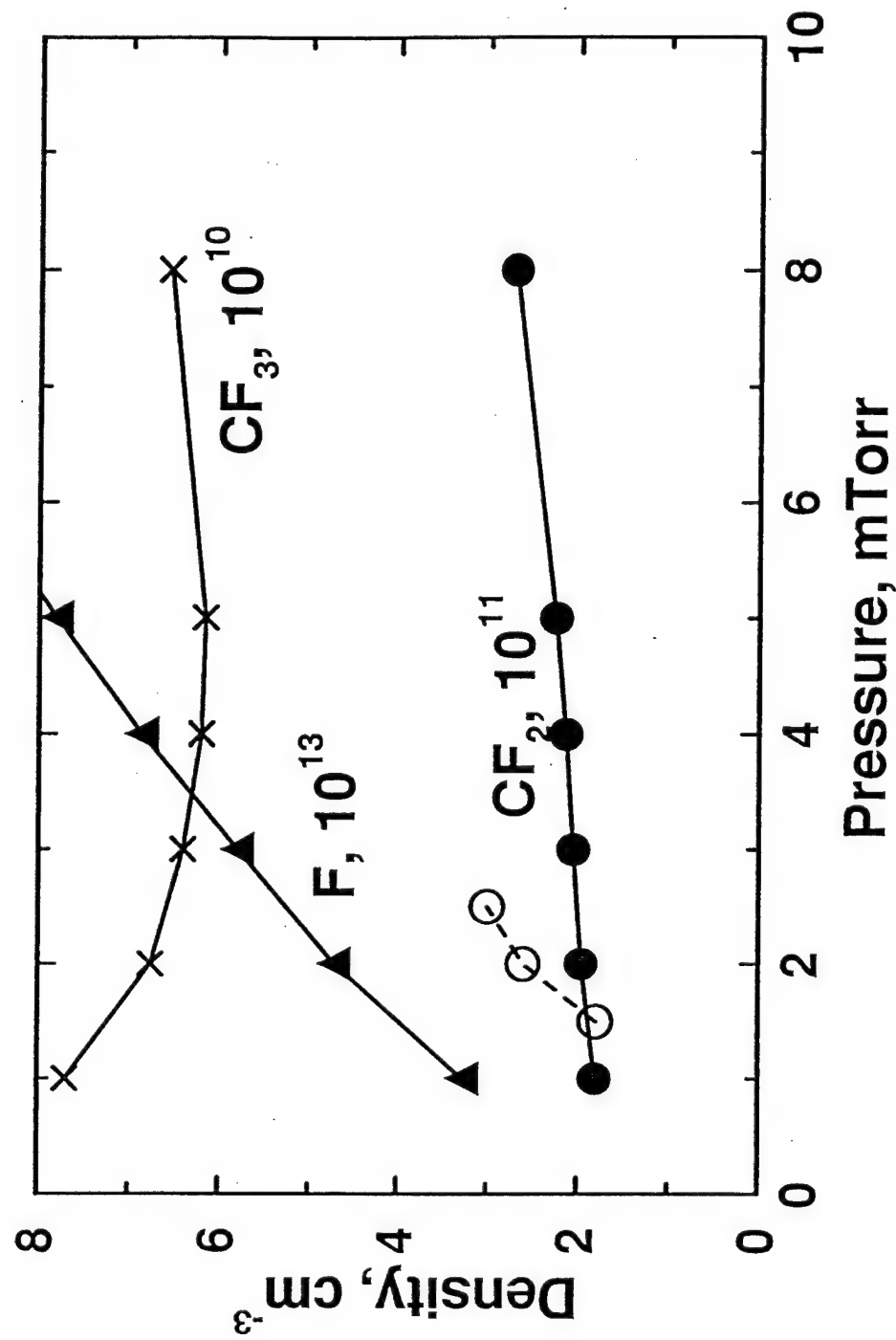


Fig. 10.8 Effect of pressure on radical concentrations.  $CF_4$  flow is 30 sccm. Open circles are  $CF_2$  concentrations from Ashtiani (Chapter 4), measured by IR absorption spectroscopy.

## 11. User-Friendly Code

A graphical user interface was developed for the 0-d code used in this study. This code runs on a personal computer. The input parameters consist of only those parameters for which there are knobs on the reactor panel, such as pressure, microwave power, and flow rates of various feed gases. The user needs to provide information on the reactor length scales, such as reactor height (or length) and radius; these are used to compute the flow volume and surface area of the source and process chambers. Other input parameters include number of wafers, wafer size, wall/wafer temperature, feed stream temperature, and orientation of reactor (vertical or horizontal to include gravitational effects on flow and to choose proper heat transfer correlations for heat rejection to the ambient). For a given feed gas system, the user needs to specify the species and a list of plasma phase and surface reactions. These can be input using alphanumeric characters in the reaction set window. A library of species along with their chemical symbols, molecular weight, and their force constants for transport property evaluation is provided with the interface. The code/interface also includes a built-in access to JANNAF and Sandia thermochemical databases. Also, each of the windows comes with an on-line help module which explains the input variables corresponding to that window. This code can be easily used with the aid of the interface to obtain the volume-averaged properties of a plasma or non-plasma process.

## 12. Summary and Conclusions

The ECR technology used in plasma processing is by far the most complex of competing techniques, characterized by the interaction of plasma generation, electromagnetics, plasma/surface interaction, ion transport, fluid flow, heat transfer, neutrals transport and chemistry, and surface activities. A comprehensive multidimensional model with all of the effects included and coupled is beyond the scope of this project. Instead a modular approach of varying complexity levels has been used here to attack this problem. Zero-, one-, and two-dimensional models were developed. The lower order models allowed coupling of all effects, while higher order models naturally had to leave out one or two features and look at them only modularly. This approach allowed us to generate insight into the mechanisms of ECR operation, as well as an opportunity to explore the effects of process and reactor geometry variables on the state of the plasma, neutrals generation, and all aspects relevant to etching and deposition. The models were used to study argon, chlorine,  $\text{CF}_4$  discharges with applications to silicon and GaAs processing. Pulsed discharges in which the input power is modulated has been modeled since pulsing has been shown to result in notch-free etching of narrow features. We also explored the reactor scaling issues with the aid of gas flow modeling.

The lowest order model or 0-d code was equipped with a GUI for running on PCs. A Phase III effort would undertake a similar exercise for the 1- and 2-d codes. This would allow the transfer of all three codes to the industry. The 0- and 1-d codes also apply to ICP and other high density reactors and hence, are of interest to a wider community: equipment manufacturers, chip manufacturers, and universities.

Future work in this field involves efforts in several directions. On the reactor modeling front, all effects listed at the beginning of this section must be self-consistently included in the model. While including these physical features per se is not the problem, solving such a massively coupled problem in 3-d (even 2-d) is not an ordinary task. The time scales involved, electron vs. ions vs. neutrals, are orders of magnitude different. The fluid flow Mach number is low ( $10^{-3}$  -  $10^5$ ) but there is significant density variation due to variations in pressure and temperature across the reactor. The electron impact reactions may be stiff with respect to electron temperature, which is a solution variable. The recombination reactions are slower but important. With such diverse

features, the numerical aspects of the problem are extraordinarily complex; these would involve long term research and require expertise from multidisciplinary groups. Also, efficient grid generation techniques are a must to describe complex commercial geometries.

Even when all of the above goals are achieved in the next few years, availability of such models may be of little value if we do not have reaction kinetics data for many of the gases used in semiconductor processing. The current knowledge covers reasonably well only a brief list of gases: argon, helium, nitrogen, chlorine, oxygen,  $\text{CF}_4$ ,  $\text{SF}_6$ , and silane. Much work needs to be done for a variety of other gases such as  $\text{BCl}_3$ ,  $\text{SiCl}_4$ ,  $\text{CHF}_3$ ,  $\text{C}_x \text{H}_y\text{F}_z$ ,  $\text{NF}_3$ , to name a few. A more urgent area is the interaction of radicals and ions with the wafer surface. Availability of reaction kinetics data base is critical to realize the full potential of computational modeling.

## References

1. M. Meyyappan, et al., Process modeling of magnetron reactive ion etching (MIE) - Application to GaAs and AlGaAs, Phase II Final Report to U.S. Army ETDL on Contract DAAL01-88-C-0842, 1991.
2. G. McLane, Research on Magnetron Enhanced RIE, In Progress.
3. O.A. Popov, Ed., High Density Plasma Sources (Noyes Publications, 1995).
4. J. Asmussen, J. Vac. Sci. Tech. A, **7**, 883 (1989).
5. Y. Manabe and T. Mitsuyu, J. Appl. Phys., **66**, 2475 (1989).
6. S. Meikle and Y. Hatanaka, Appl. Phys. Lett., **57**, 762 (1990).
7. J. Flemish, Work at U.S. Army Research Laboratory, Ft. Monmouth, NJ.
8. T.V. Herak, et al., J. Appl. Phys., **65**, 2457 (1989).
9. D.A. Carl, et al., J. Appl. Phys., **70**, 3301 (1991).
10. G. Fortuno-Wiltshire, J. Vac. Sci. Tech. A, **9**, 2356 (1991).
11. M. Haverlag, et al., Appl. Phys. Lett., **61**, 2875 (1992).
12. S.J. Pearton, et al., Appl. Phys. Lett., **56**, 1424 (1990).
13. S.J. Pearton, Materials Sci. and Eng., **B10**, 187 (1991).
14. Y. Weng and M.J. Kushner, J. Appl. Phys. **72**, 33 (1992).
15. R.K. Porteous, H.M. Wu, and D.B. Graves, Plasma Sources Sci. Technol. **3**, 25 (1994).
16. M.D. Kilgore, H.M. Wu, D.B. Graves, J. Vac. Sci. Technol. B **12**, 494 (1994).
17. R.B. Bird, W.E. Stewart, and E.N. Lightfoot, Transport Phenomena (Wiley, New York, 1960).
18. M. Meyyappan, in Computational Modeling in Semiconductor Processing, Chapter 5, edited by M. Meyyappan (Artech House, Boston 1995)
19. J.D. Ramshaw, J. Non-Equilib. Thermodyn. **14**, 295 (1990).
20. J.D. Ramshaw, J. Non-Equilib. Thermodyn. **18**, 121 (1993).
21. J.D. Ramshaw and C.H. Chang, Plasma Chem. Plasma Process. **13**, 489 (1993).
22. G.L. Rogoff, J. Phys. D: Appl. Phys. **18**, 1533 (1985).
23. R.A. Stewart, P. Vitello, and D.B. Graves, E.F. Jaeger, and L.A. Berry, Plasma Sources Sci. Technol. **4**, 36 (1995).

24. Y. Yasaka, A. Fukuyama, A. Hatta, and R. Itatani, *J. Appl. Phys.* **72**, 2652 (1992).
25. W.R. Briley and H. McDonald, *J. Comp. Phys.*, **24**, 372 (1977).
26. C. Lee and M.A. Lieberman, *J. Vac. Sci. Technol. A* **13**, 368 (1995).
27. R. Wise, D.P. Lymeropoulous, and D.J. Economou, *Plasma Sources Sci. Technol* **4**, 317 (1995).
28. M. Meyyappan and T.R. Govindan, *IEEE Trans. Plasma Sci.* **23**, 623 (1995).
29. R.D. Present, *Kinetic Theory of Gases* (McGraw Hill, New York, 1958).
30. J.P. Holman, *Heat Transfer* (McGraw Hill, New York, 1976).
31. T.R. Govindan and F. de Jong, in *Computational Modeling in Semiconductor Processing*, Chapter 2 , edited by M. Meyyappan (Artech House, Boston, 1995).
32. JANNAF Thermochemical Tables, Dow Chemical Company, 1965.
33. J. Hopwood and J. Asmussen, *Appl. Phys. Lett.* **22**, 2473 (1991).
34. T. Nakano, N. Sadeghi, and R.A. Gottscho, *Appl. Phys. Lett.* **58**, 458 (1991).
35. M.D. Bowden, et al., *J. Appl. Phys.* **73**, 2732 (1993).
36. K. Ono, et al., *Jap. J. Appl. Phys.*, **33**, 4424 (1994); *Pure & Appl. Chem.* **66**, 1327 (1994).
37. J. Bukowski, Ph.D. Thesis, University of California, Berkeley, 1995.
38. O.A. Popov, S.Y. Shapoval, and M.D. Yoder, *J. Vac. Sci. Technol. A* **12**, 300 (1994).
39. O.A. Popov, in *Physics of Thin Films*, Edited by M. Francombe and J. Vossen, Vol. 17, Academic Press (1993).
40. S.M. Gorbatkin, L.A. Berry, and J.B. Roberto, *J. Vac. Sci. Technol. A* **8**, 2893 (1990).
41. D.A. Carl, M.C. Williamson, M.A. Lieberman, and A.J. Lichtenberg, *J. Vac. Sci. Technol. B* **9**, 339 (1991).
42. S. Iizuka and N. Sato, *J. Appl. Phys.* **70**, 4165 (1991).
43. S.M. Rossnagel, S.J. Whitehair, C.R. Guarnieri, and J.J. Cuomo, *J. Vac. Sci. Technol. A* **8**, 3113 (1990).
44. S. Samukawa, *Appl. Phys. Lett.* **64**, 3398 (1994).
45. S. Samukawa and K. Terada, *J. Vac. Sci. Technol. B* **12**, 3300 (1994).
46. S. Samukawa, *Jpn. J. Appl. Phys.* **32**, 6080 (1993).
47. K. Takahashi, M. Hori, and T. Goto, *Jpn. J. Appl. Phys.* **32**, L 1088 (1993).

48. K. Tsujimoto, T. Kumihashi, N. Kofuji, and S. Tachi, *J. Vac. Sci. Technol. A* **12**, 1209 (1994)
49. K. Ashtiani, J.L. Shohet, and R. Harvey, *J. Vac. Sci. Technol. A* **11**, 1136 (1993).
50. J.S. Jenq, J. Ding, J.W. Taylor, and N. Hershkowitz, *Plasma Sources Sci. Tech.* **3**, 154 (1994).

ARMY RESEARCH LABORATORY  
PHYSICAL SCIENCES DIRECTORATE  
MANDATORY DISTRIBUTION LIST

Oct 1996  
Page 1 of 2

Defense Technical Information Center\*  
ATTN: DTIC-OCC  
8725 John J. Kingman Rd, STE 0944  
Fort Belvoir, VA 22060-6218  
(\*Note: Two DTIC copies will be sent  
from STINFO office, Ft Monmouth, NJ)

Director  
US Army Material Systems Analysis Actv  
ATTN: DRXSY-MP  
(1) Aberdeen Proving Ground, MD 21005

Commander, AMC  
ATTN: AMCDE-SC  
5001 Eisenhower Ave.  
(1) Alexandria, VA 22333-0001

Director  
Army Research Laboratory  
ATTN: AMSRL-D (John W. Lyons)  
2800 Powder Mill Road  
(1) Adelphi, MD 20783-1197

Director  
Army Research Laboratory  
ATTN: AMSRL-DD (COL Thomas A. Dunn)  
2800 Powder Mill Road  
(1) Adelphi, MD 20783-1197

Director  
Army Research Laboratory  
2800 Powder Mill Road  
Adelphi, MD 20783-1197  
(1) AMSRL-OP-SD-TA (ARL Records Mgt)  
(1) AMSRL-OP-SD-TL (ARL Tech Library)  
(1) AMSRL-OP-SD-TP (ARL Tech Publ Br)

Directorate Executive  
Army Research Laboratory  
Physical Sciences Directorate  
Fort Monmouth, NJ 07703-5601  
(1) AMSRL-SE  
(1) AMSRL-SE-C (V. Rosati)  
(1) AMSRL-SE-C (M. Hayes)  
(1) AMSRL-OP-FM-RM  
(22) Originating Office

Advisory Group on Electron Devices  
ATTN: Documents  
Crystal Square 4  
1745 Jefferson Davis Highway, Suite 500  
(2) Arlington, VA 22202

Commander, CECOM  
R&D Technical Library  
Fort Monmouth, NJ 07703-5703  
(1) AMSEL-IM-BM-I-L-R (Tech Library)  
(3) AMSEL-IM-BM-I-L-R (STINFO Ofc)

ARMY RESEARCH LABORATORY  
PHYSICAL SCIENCES DIRECTORATE  
SUPPLEMENTAL DISTRIBUTION LIST  
(ELECTIVE)

Oct 1996  
Page 2 of 2

Deputy for Science & Technology  
Office, Asst Sec Army (R&D)  
(1) Washington, DC 20310

Cdr, Marine Corps Liaison Office  
ATTN: AMSEL-LN-MC  
(1) Fort Monmouth, NJ 07703-5033

HQDA (SARDA-TR)  
Dr. Richard Chait  
(1) Washington, DC 20310

Director  
Naval Research Laboratory  
ATTN: Code 2627  
(1) Washington, DC 20375-5000

USAF Rome Laboratory  
Technical Library, FL2810  
ATTN: Documents Library  
Corridor W, STE 262, RL/SUL  
26 Electronics Parkway, Bldg 106  
Griffiss Air Force Base  
(1) NY 13441-4514

Dir, ARL Battlefield  
Environment Directorate  
ATTN: AMSRL-BE  
White Sands Missile Range  
(1) NM 88002-5501

Dir, ARL Sensors, Signatures,  
Signal & Information Processing  
Directorate (S3I)  
ATTN: AMSRL-SS  
2800 Powder Mill Road  
(1) Adelphi, MD 20783-1197

Dir, CECOM Night Vision/  
Electronic Sensors Directorate  
ATTN: AMSEL-RD-NV-D  
(1) Fort Belvoir, VA 22060-5806

Dir, CECOM Intelligence and  
Electronic Warfare Directorate  
ATTN: AMSEL-RD-IEW-D  
Vint Hill Farms Station  
(1) Warrenton, VA 22186-5100